Stellar Radio Transients: From Brown Dwarfs to Pulsars And Beyond

Vikram Ravi

A thesis submitted for the degree of

Bachelor of Science with Honours in Astronomy & Astrophysics

at The Australian National University

Research School of Astronomy & Astrophysics

October 2009

Declaration

This thesis is an account of research undertaken between February 2009 and October 2009 at The Research School of Astronomy & Astrophysics, The Australian National University, Canberra, Australia.

Except where acknowledged in the customary manner, the material presented in this thesis is, to the best of my knowledge, original and has not been submitted in whole or in part towards a degree at any university.

Vikram Ravi

Acknowledgements

My honours year, and this thesis, has been among the most happily hectic experiences of my life. I will start with the formal/semi-formal thank you's and finish with some shout-outs.

First, a huge thank-you to my supervisors: Dayal Wickramasinghe for his guidance through (and away from) the sometimes crazy ideas involved in the thesis; Lilia Ferrario, for her constant interest and help with the basics of setting up an honours project; and finally George Hobbs. Thank you, George, for the drama, the (few) losses at ping-pong, the calls of incompetence, and the Ashes. But most of all, thank you (and now Sha) for always offering me a place at your house, for going along with the, sometimes silly, ideas I spout, and for being a good friend.

To the Astronomy & Astrophysics Honours coordinator Helmut Jerjen, thank you so much for making the Honours year as simple as possible, and for organising the RSAA travel funds (and also for the fun times in class). I would also like to thank Baerbel Koribalski for making me an informal ATNF student.

Next, I would like to acknowledge the Mathematical Sciences Institute at the ANU for offering me such conveniently located desk space, and great office mates who put up with my somewhat focused working habits.

Thank you to everyone who helped and collaborated with me on the project: Dr. David Champion (ATNF/MPIfR), Dr. Mike Keith (ATNF), Prof. Ray Norris (ATNF), Prof. Don Melrose (USyd), Dr. Dick Manchester (ATNF). Mr. Justin Bray (Adelaide), Dr. Simon Johnston (ATNF), Dr. Patrick Weltevrede (ATNF/JBO), Dr. Jamie Stevens (ATNF), Dr. Martin Cohen (UC Berkeley), Prof. Saul Adelman (Citadel), Prof. Joel Weisberg (Carleton), and Dr. Gyula Josza (ASTRON).

There's not enough room to say all I want about everyone individually, but, in any case, thanks, it's been a grand learning experience and a great time.

For the observing trips: thanks to Jamie Stevens, Robin Wark and Phil Edwards for putting up with my antics at Narrabri and for making the system work so well, and to my DAs Rajan Chhetri and Emil Lenc. Thank you David for the great drive, all the other fun at Sydney, and your constant presence on Skype. Also, thank you to Ettore Caretti and John Reynolds for the help with Parkes. Finally, Jonathan Khoo − thanks mate, it's been a blast...mate.

To my parents: thank you for everything

Now for the shoutouts: Burgmann in general, for the fun and support; Will, it's going to be amazing; Tom, for IB; Zemma, for astro and tea; Don, for being a mate; all my friends, for being there; and to the ANU and Berkeley, for the last four years.

Preface

The research that comprises this thesis has been an extraordinary experience, in that it involved a large collaboration of interested researchers from a variety of institutions, has led to more than 90 hours of telescope time and a publication being submitted to MNRAS, with a few more in preparation.

The body of work described here was the result of collaboratons with and advice from a number of scientists, from the Australian National University (ANU), the Australia Telescope National Facility (ATNF), the University of Sydney (USyd), the University of Adelaide (Adelaide) and the Max Planck Institut für Radioastronomie (MPIfR). Included in this collaboration were my supervisors Prof. Dayal Wickramasinghe (ANU), Dr. Lilia Ferrario (ANU) and Dr. George Hobbs (ATNF), as well as collaborators and advisors Dr. David Champion (ATNF/MPIfR), Dr. Mike Keith (ATNF), Prof. Ray Norris (ATNF), Prof. Don Melrose (USyd), Dr. Dick Manchester (ATNF) and Mr. Justin Bray (Adelaide). A number of other people made useful and significant contributions: they are listed in the acknowledgements.

The observational data that was used in this thesis partly resulted from observations undertaken in October and November 2008, with the Australia Telescope Compact Array, before the start of my honours year. However, I found it necessary to obtain more data, some of which is included in this thesis. I was first author on proposals to the Westerbork Synthesis Radio Telescope (R09B/010 - 36 hours) and the Australia Telescope Compact Array (C2114 - 24 hours), and used a large amount of unallocated time at the Parkes Radio Telescope ($\sim$ 20 hours) and some at the Australia Telescope Compact Array ($\sim$ 10 hours). The data that was not processed in time for this thesis will be looked at shortly after.

Finally, we, as a collaboration, have submitted a paper to the Monthly Notices of the Royal Astronomical Society (MNRAS) (Ravi et al. 2009, submitted), which consists of the work described in Chapter 3 of this thesis. Other papers, particularly on the work described in Chapter 5, are being written, and we anticipate that the data that has not yet been processed will lead to exciting results as well.

Abstract

A variety of magnetic stars, from brown dwarfs to Ap stars to white dwarfs, have recently been observed to produce transient radio emission, sometimes periodic. These pulses and flares are, in general, 100% circularly polarised, and occur on timescales ranging between a few minutes and an hour. In all cases, the emission is thought to be the result of a coherent mechanism and magnetospheric in origin, with the periodicities linked to the stellar rotation periods.

In this thesis, I present observational and modelling studies of a select sample of previously detected transient emitters from each of the aforementioned stellar classes − the magnetic Ap star CU Virginis, the brown dwarfs DENIS 1048−3956 and LHS 3003 and the white dwarfs RX J0317−853 and PG 1031+234 − and consider them as defining examples of populations of stellar radio transient sources. I use the modelling to constrain the properties of the magnetospheres of these stars using observational data obtained at the Australia Telescope Compact Array. Twin pulses are detected from CU Virginis every rotation period: here, these are shown to be caused by electron-cyclotron maser emission. The CU Virginis magnetosphere and non-thermal electron population are modelled by fitting the quiescent lightcurves. I find that the quiescent radio spectrum of the flaring brown dwarf DENIS 1048−3956 obeys a negative power law, the first such result for a brown dwarf. This implies a power law non-thermal electron distribution similar to that of CU Virginis. No emission is detected from the white dwarfs, and these null results are used to suggest that white dwarf winds must closely resemble pulsar winds in their anisotropic electron pitch angle distributions.

I also discuss unified characteristics of the emission models of CU Virginis and the brown dwarfs, with the aim of linking the modelling ideas to analogous pulsar phenomena. Finally, I discuss and analyse the populations of the transient emitters from both physical and emperical perspectives, in order to assess their detectability in upcoming radio surveys with next-generation telescopes. The study of the transient radio sky is poised to be among the most exciting and prolific areas in the future of radio astronomy.

Note on Units and Constants

SI units are used throughout this thesis. The only major exception is in the case of radio flux density, where the more commonly used Jansky (Jy; $1\,Jy = 10^{-26}\,W\,m^{-2}\,Hz^{-1}$) is applied. The magnetic field strength (or magnetic flux density) is always expressed in Teslas (T), rather than Gauss (G). For reference, $1\,T = 10^{4}\,G$. Also, parsecs (pc) are usually used as astronomical units of distance: $1\,pc = 3.08568 \times 10^{16}\,m$.
Symbols for fundamental constants are not defined in the text, but are listed here:
Fundamental unit of charge, or proton charge: q_e.
Electron mass: m_e.
Mass of a hydrogen atom: m_H.
Speed of light in vacuum: c.
Boltzmann's constant: k_B.
Universal gravitational constant: G.
Note that 'e' always represents the mathematical constant (Euler's number). Also, commonly used symbols are:
M: mass of a star.
R: radius of a star.
ν: frequency of electromagnetic radiation.

CONTENTS

Introduction and Motivation

1.1 Introduction

Time-domain observations of the radio sky have been instrumental in furthering our understanding of fundamental physics, astrophysical mechanisms and the population syntheses of a variety of galactic and extragalactic objects. Radio transients − including periodic pulses[1], random flaring epochs and isolated aperiodic bursts on timescales of microseconds to hours − are by their very nature probes of physics at the most compact of astronomical scales. I define a radio transient event as one where, for a measurably limited time, a point or area in the sky appears brighter than the persistent background. Time-domain radio surveys and targeted observations have recently unleashed a horde of transient sources. Whole unforeseen classes of objects, such as neutron star Rotating Radio Transients (RRATS) [McLaughlin et al. 2006], have been discovered. More excitingly, a large number of bursts, such as the galactic centre radio transients [Hyman et al. 2005], the Bower sub-millijansky transients [Bower et al. 2007] and the Lorimer burst [Lorimer et al. 2007], are of completely unknown origins. Furthermore, a selection of objects, from ultracool dwarf stars [Hallinan et al. 2007] to pre-main sequence T Tauri stars [Salter, Hogerheijde & Blake 2008] to magnetic Ap stars [Trigilio et al. 2000], exhibit radio pulses and flares. However, the parameter space of the dynamic radio sky has remained largely unexplored, because radio surveys, and indeed telescopes, are not usually optimised for transient detection. This field promises to be among the most compelling and prolific areas in the future of radio astronomy [Cordes, Lazio & McLaughlin 2004].

A significant fraction of the short-timescale radio transients associated with known sources are galactic in origin, and are identified with a variety of stellar objects. Stellar radio transients can again be separated into those caused by cataclysmic epochs that affect the stars themselves, such as supernovae or large surface flares, and those that originate well beyond the stellar photospheres. In the latter case, essentially all such transients involve stellar magnetic fields and accelerated charges radiating through gyromagnetic processes. The relative stability of such systems and the anisotropic beaming of gyromagnetic emission mechanisms entail that these transients often exhibit periodicities tied to the rotation periods of the stars. Examples of periodic magnetic star radio transients abound, from pulsars [Hewish et al. 1968], which are seen to emit a pulse each time a stable emission beam swings across the line of sight, to periodic pulses from ultracool dwarf stars [Hallinan et al. 2007].

We can then elucidate the scope of this thesis: rotating magnetic star radio

[1] In the context of this thesis, pulses always refer to periodic transient emission, as opposed to isolated flares. Pulses do *not* refer to stellar pulsations, but to pulsed radio emission.

transients. The aims herein are:

- to characterise three potential classes of radio transient, and derive observational constraints on the physical mechanisms involved and the population syntheses, and
- to present models of the emission from these radio transients with a view to unifying the physics involved.

1.1.1 A brief historical overview

The overarching goal of this thesis is to take a unified approach to rotating magnetic star radio transients, in a sense carving out a previously undefined area of astronomy. While a multitude of literature − theoretical and observational − exists that falls within our scope, I now attempt to place in context the various branches of astronomy that led to this thesis.

I trace the origins of this field to two areas of astrophysics: solar system radio astronomy and the study of explosive and variable phenomena in the radio sky. The solar system exhibits a rich set of examples of exotic non-thermal radio emission processes. These include the menagerie of radio bursts and storms from the Sun [Dulk 1985], the Auroral Kilometric Radiation (AKR) from non-thermal electrons of the solar wind trappped in the Earth's magnetic field [Kurth, Baumback & Gurnett 1975], and the Jovian Decametric Emission (known as DAM) from electrons accelerated by electric fields in the Jupiter-Io magnetic interaction [Warwick 1967]. Also, even from the early days of radio astronomy, the radio sky was known to be dynamic. The Interplanetary Scintillation Array, a high time resolution radio telescope built in 1967 to study the rapid intensity fluctuation of radio sources due to interactions with the solar wind plasma [Okoye & Hewish 1967], was in fact the telescope that made the serendipitous discovery of pulsars [Hewish et al. 1968].

The non-thermal radio emission mechanisms identified in the solar system have been applied to radio emission from stars. Gyrosynchrotron emission mechanisms from thermal and non-thermal power law electron distributions are invoked to explain the quiescent[2] emission from magnetically active stars [Güdel 2002]. These mechanisms were first identified in Microwave Impulsive bursts from the Sun [Kundu 1983]. Gyrosynchrotron emission involves mildly relativistic electrons (energies $> 10\,\mathrm{keV}$), with thermal (Maxwellian) or non-thermal (power law or other) energy distributions and generally isotropic pitch angle distributions. As these electrons gyrate around magnetic field lines, they radiate in broad spectra peaked between 10 and 100 harmonics of the fundamental cyclotron frequency [Dulk & Marsh 1982].

[2] The quiescent component of a source is considered to be any persistent, non-transient radio emission. Quiescent emission, or *quiescence*, can be variable, but is always persistent, in contrast to transient emission.

Transient emission from stars is nearly always interpreted in terms of coherent emission mechanisms. Coherent emission involves the amplification of the emission by the coherent phase behaviour of the emitting electrons. The 'free energy' required for this amplification is found in inverted electron energy distributions, with more electrons at higher energies, or in anisotropic pitch-angle distributions. As shall be seen, a key coherent mechanism is the Electron-Cyclotron Maser (ECM) [Twiss 1958], also first applied to AKR and DAM [Melrose 1976], and to Microwave Spike bursts from the Sun [Slottje 1978]. Coherent emission is identified by brightness temperatures generally in excess of 10^{12} K and, in the case of ECM emission, near complete polarisation of the emission [Dulk 1985].

The discovery of pulsars in 1968 heralded the beginning of the field of high time resolution extra-solar astronomy. Pulsars (pulsating radio stars) produce short duty-cycle, highly periodic, significantly polarised pulses of radio emission on periods ranging from milliseconds to a few seconds. The short duration of the emission implies brightness temperatures on the order of 10^{30} K [Manchester & Taylor 1977], a clear sign of coherent emission. Pulsars are modelled as highly magnetic neutron stars (with fields in excess of 10^4 T), rotating on the periods of the pulses, that create and accelerate electron-positron pairs by the extreme electric potentials caused by the rotating dipole field [Goldreich & Julian 1969]. Pulsars are the archetypal sources of stellar radio transient emission. The stability of the emission means that pulsars form extremely useful clocks. Studies of the timing of the pulses from pulsars form our best probes into the frontiers of gravitational physics [Kramer 2005]. The pulsar emission mechanism is not constrained, because of the lack of independent constraints on the magnetic field structures and magnetosphere compositions of pulsars. This is because of their small sizes; pulsar radii are on the order of ~ 10 km [Manchester & Taylor 1977].

In recent years, pulsars have been joined by a flood of transient sources and source populations. Radio astronomy has been revolutionised by the availability of faster and more efficient software and hardware; data mining and post-processing are among the powerful new tools now applied to search for transient sources in previously obtained radio data [Cordes, Lazio & McLaughlin 2004]. Searches for transient sources were also catalysed in part by the discovery of a variety of classes of multi-wavelength exploding or flaring objects, such as Gamma-Ray Bursts (GRBs) [Klebesadel, Strong & Olson 1973] (GRBs were in fact first detected by US military satellites deployed to monitor nuclear weapons testing). Other discoveries, such as the unexplained single flaring epoch known as the Galactic Centre Transient [Zhao et al. 1992], also motivated the field. Data mining of the Parkes Multibeam Pulsar Survey [Manchester et al. 2001] archives has resulted in a number of fascinating short-timescale transients, such as RRATS (long-period neutron stars) [McLaughlin et al. 2006], and the single-epoch Lorimer burst [Lorimer et al. 2007]. Searches through the data archives of the Very Large Array (VLA) have also revealed a number of transient events [Bower et al. 2007],

some unidentified and others matched to known events such as GRBs. The set of transient sources has also been expanded by blind radio surveys targeted at weak transient detection; these surveys have found sources such as the intermittent, periodic Galactic Centre radio transients [Hyman et al. 2005] and the unidentified single-epoch galactic transients found in the Nasu 1.4 GHz survey [Matsumura et al. 2007].

1.2 Summary of this thesis

This thesis aims to develop the physics of selected objects in different classes of magnetic rotating stars that are potentially prototypical examples of hitherto uncharacterised classes of radio transient. To date, studies of the transient radio sky have primarily focused on blind searches for new classes of transient events, followed by attempts to infer the types of sources from analyses of the radio emission and identifications with sources in other wavelength bands. This approach is well justified: the more transient sources that are found, the more likely it is that either an identification will be made or that statistical results will characterise the populations. However, for transient sources already identified with known classes of stars, I make a study of the physics of the transient emission with two aims:

- to form basic models for the transient emission from these sources in order to characterise potential classes of radio transient of which these sources are prototypes, and
- to gain some insight into the population of similar transients in terms of their detectability by upcoming radio surveys with next-generation telescopes, and to also understand the stability of the emission.

The incidence of transient emission across a variety of stars provides valuable insights into the evolution, atmospheres and magnetic fields of stellar populations. Transient emission, interpreted with coherent emission mechanisms, requires specific conditions for its production. Hence, the detection and analysis of transient emission from a star allows for tight constraints on the magnetosphere properties, including the populations of non-thermal electrons, the magnetic field geometry and strength, and the nature of the means by which the stellar atmosphere is created. The evolution of magnetic fields in stars, parallel to the evolution of the stars themselves, is not well understood, as it is difficult in many cases to accurately map the magnetic field strengths and geometries. Transient coherent radio emission, where the emission frequency is generally directly proportional to the magnetic field strength, is an immensely powerful probe into the magnetic field structures of a variety of stars at different evolutionary stages. The propagation and polarisation of transient radio emission through stellar magnetospheres, and the variations in these properties with the rotation of the stars, are also useful

probes. Finally, the stability of periodic stellar radio pulses, on periods tied to the rotation rates, allow for precise determinations of the rotational properties of such stars, including their spin-down behaviour.

Periodic radio pulses from rotating magnetic stars, as seen in the magnetic Ap star CU Virginis [Trigilio et al. 2000] and a few ultracool dwarfs [Hallinan et al. 2008], bear close similarities to pulsar emission. Both are thought to be caused by tightly beamed coherent emission mechanisms, with periodicities linked to the stellar rotation periods. In many non-pulsar periodic radio transients, the periodicity of the emission is also extremely stable, much like in pulsars themselves. Furthermore, the emission in both cases originates in and propagates through a magnetised plasma. However, unlike in pulsars, the magnetic fields, magnetospheric plasmas and electron acceleration mechanisms in rotating magnetic stars can be probed through means independent of the radio pulses themselves. Therefore, non-pulsar stellar radio transients offer a variety of physical probes into the pulsar emission mechanism, an outstanding problem of astronomy.

Finally, upcoming large-area radio continuum and transient surveys will greatly expand the stellar radio transient sample, both in source numbers and classes. Future radio telescopes such as the Square Kilometre Array (SKA) and the Low Frequency Array (LOFAR), as well as their predecessors like the Australian SKA Pathfinder (ASKAP) [Johnston et al. 2008], have among their primary science goals the study of the transient radio sky. It is therefore important to understand how many and what sort of transients could be observed. By characterising the pulses, the populations can be emperically constrained. This method requires an understanding of the pulse stabilities and duty-cycles, as well as estimates of the population fractions of pulse emitters. However, the second method is to constrain the population through other observable stellar parameters, such as the rotation rates or magnetic fields. These constraints could be statistical, based on trends of the radio emission with the rotation or magnetic field, or they could be theoretical, based on a cohesive model of the transient emission from magnetic rotators parametrised in terms of basic observables.

Therefore, there exist four motivations for this thesis:

- to further knowledge about stellar magnetosphere astrophysics, in terms of the magnetic field geometry and strength, the plasma environment, electron acceleration mechanisms, the means by which the magnetospheres are filled with plasma, and the evolutionary history of the magnetospheres,

- to characterise the rotational properties of periodic stellar pulse emitters by analysing the pulse arrival times,

- to link the pulse emission models of rotating magnetic stars, including the emission mechanisms, radiative propagation, sources of non-thermal electrons and beaming to the hitherto unsolved pulsar emission mechanism, and

- to understand how many such transients will be detectable in large-area radio continuum and transient surveys by upcoming radio telescopes.

The body of this thesis deals with three potential prototypical examples of stellar radio transient classes. First, in Chapter 3, I consider periodic radio pulses from the magnetic Ap star CU Virginis. I present and analyse new observational results, and use these, along with archival data, to characterise the emission. I also derive information about the beaming geometry of the emission, which constrains the emission mechanism, and provide emperical estimates of the detectability of similar sources in future surveys. In Chapter 4, I then describe and apply a magnetosphere model for CU Virginis, based on its quiescent emission, and apply the results to models for the pulses and the spin-down of the star. In the next two chapters, I describe searches for transient emission from selected brown dwarfs and white dwarfs previously observed to flare. While no transient emission is found, I measure the quiescent spectrum of the brown dwarf DENIS 1048−3956 and for the first time confirm this spectrum as a power law. I use this spectrum to analyse the emission mechanism and magnetosphere properties in Chapter 5. In Chapter 6, the non-detections of the observed white dwarfs are discussed and applied to constrain models for highly magnetic isolated white dwarf magnetospheres. I also analyse archival data to show that one of the observed white dwarfs, previously believed to have flared, did not actually do so. Finally, in Chapter 7, I discuss unified properties of the pulsed emission from the low-field transient population (LFTP), including brown dwarfs and CU Virginis-type transients. The conclusions reached and the multitudinous opportunities for future work are described in Chapter 8.

Observational Techniques

2.1 Introduction

I begin with a discussion of the observational techniques used in this thesis. All original observational work presented herein is based on data taken with radio telescopes, in particular the Australia Telescope Compact Array (ATCA) [Frater, Brooks & Whiteoak 1992]. The ATCA is a radio telescope located near Narrabri, in North-West NSW, and consists of six 22-metre dish antennas (see Figure 2.1) operating as an interferometer. Five dishes have variable separations and are placed on a rail track three kilometres long, and the sixth is kept at a fixed position three kilometres from one end of the track. Baseline lengths, the distances between pairs of antennas, range between 30 m and 6 km. The array runs East-West, with some Northern baselines between antennas possible when a short North-South section of track, connected to the main three kilometre stretch, is used.

This section outlines the basic theory of this telescope, describing how radio images of the sky and time series of radio fluxes are made with the ATCA. Radio telescopes such as the ATCA sample the radio end of the electromagnetic spectrum; the ATCA can observe at frequencies (wavelength bands) including 1.4 GHz (20 cm), 2.4 GHz (13 cm), 5.5 GHz (6 cm), 9 GHz (3 cm) and 21 GHz (1.2 cm). Data taken in all these bands are presented and analysed in this thesis. Telescopes operating in each component of the electromagnetic spectrum are sensitive to vastly different sets of astronomical phenomena as compared to the other components. Radio astronomy is no different. Besides the Sun, the brightest objects in the radio sky are not stars but supernova remnants, active galactic nuclei, large swathes of cool hydrogen gas within and beyond the Milky Way, the diffuse lobes of radio galaxies, and the short, bright periodic bursts of emission from pulsars [Kraus 1986]. Most continuum studies in radio astronomy deal with non-thermal emission − emission from populations of electrons with non-thermal energy distributions − because the blackbody spectra of most astronomical sources of thermal emission, such as stars and nebulae, peak at infrared or higher frequencies. Also, the blackbody emission power decreases with the temperature of the radiating object.

Here, I outline how the radiation from a source at radio wavelengths is described, and measured using interferometric techniques such as those used at the ATCA. I discuss the concepts of brightness, luminosity, flux density and brightness temperature in §2, and in §3 I show how an interferometer recovers the brightness distribution of a source. Finally, I outline how radio images are made using interferometric data in §4. While this discussion has mainly been adapted for this thesis, sources include Kraus (1986) and the MIRIAD user man-

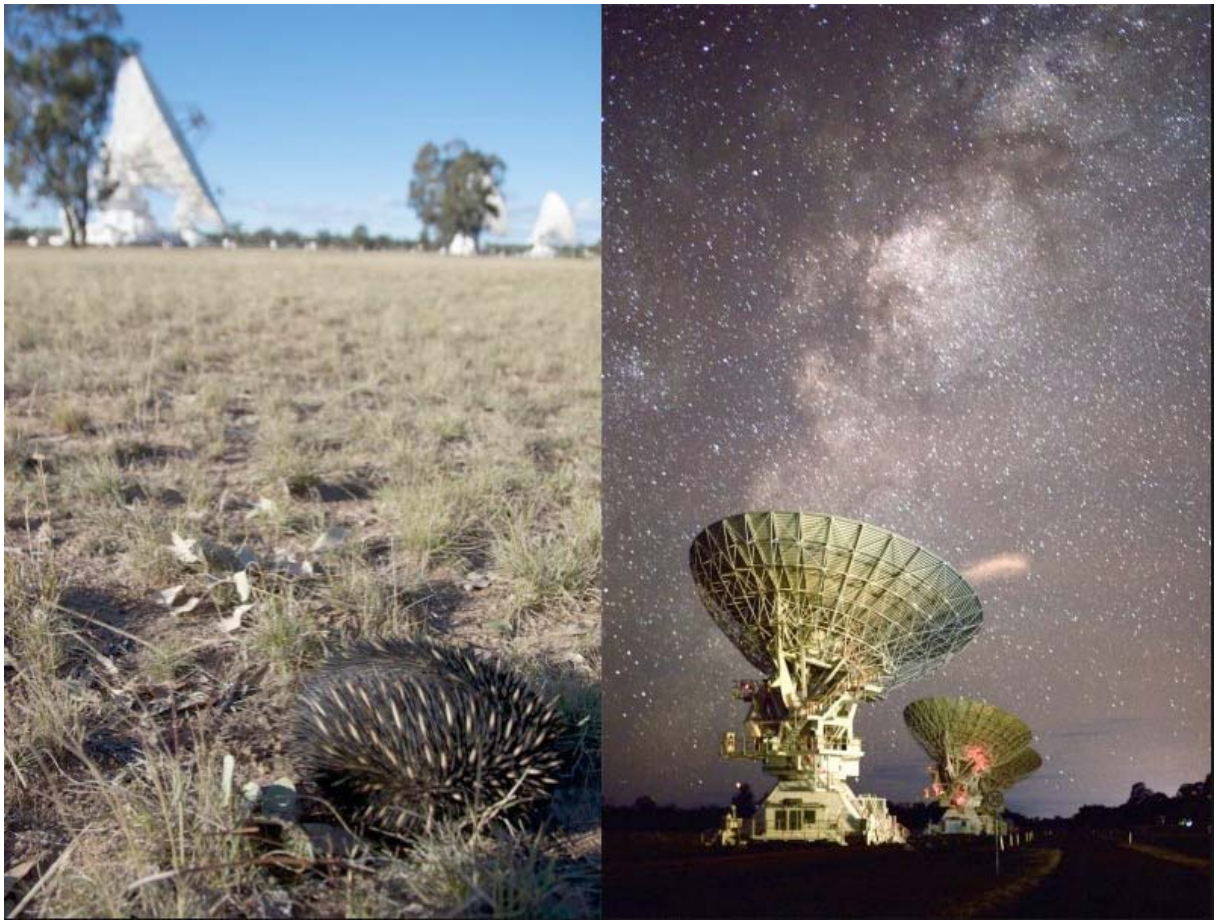

Fig. 2.1: *Left:* Three dishes of the Australia Telescope Compact Array (ATCA) with a visiting astronomer in the foreground. *Right:* Three dishes of the ATCA on the East-West track, with a few stars. (Images courtesy of Emil Lenc)

ual (http://www.atnf.csiro.au/computing/software/miriad).

2.2 Measures of radio emission

I define the brightness distribution $B(\theta, \phi)$ of a radio source on the celestial sphere as the electromagnetic energy radiated per unit time dt from a unit surface dA perpendicular to the line of sight, over a unit solid angle $d\Omega$, per unit frequency $d\nu$, at a position (θ, ϕ) on the sky. Therefore, brightness has units $W\,m^{-2}\,Hz^{-1}\,sr^{-1}$. This term is also known as the specific intensity, or the surface brightness.

From this, I derive the flux density, or as I shall hereafter refer to it, the *flux*. The flux is simply defined as the power per unit frequency per unit area of the radiation field over all viewing solid angles. This implies that the flux $S(\nu)$ is given by an integral over the solid angle Ω subtended by the source at the point of observation:

$$S(\nu) = \int_{\Omega} B(\theta, \phi) d\theta d\phi \tag{2.1}$$

The solid angle Ω can be estimated as the projected area A of the source divided by the square of the distance D to the source: $\Omega = A/D^2$, when $\sqrt{A} \ll D$. Flux has units of $W\,m^{-2}\,Hz^{-1}$, though it is usually expressed in terms of Janskys (Jy), where $1\,Jy = 10^{-26}\,W\,m^{-2}\,Hz^{-1}$. Janskys are more convenient for use in radio astronomy than the conventional SI units, and we shall use this unit throughout the thesis. However, all expressions involving a flux term will, unless otherwise mentioned, have the flux expressed in conventional SI units. Flux is possibly the most important measure in radio astronomy, because it is what a telescope observes: the flux of a source is what a telescope pointed at it will detect.

Next, I integrate the flux from a source over the entire surface area of its sphere of emission to derive its monochromatic luminosity L_ν: the power radiated by the source per unit frequency. If the flux of a source, assumed to be a symmetric emitter, is measured from a distance D, its monochromatic luminosity is given by

$$L_\nu = 4\pi D^2 S(\nu) \tag{2.2}$$

Monochromatic luminosity has units of $W\,Hz^{-1}$. If we also assume that the spectrum of a particular type of radiation from a source extends over a finite band between frequencies ν_1 and ν_2, the total luminosity in Watts is given by

$$L = \int_{\nu_1}^{\nu_2} S(\nu) d\nu \tag{2.3}$$

The total power emitted by a source across the electromagnetic spectrum is known as its bolometric luminosity.

Another useful measure of the emission from a source is the brightness temperature. The brightness temmperature T_b is simply the effective blackbody temperature necessary to emit radiation of flux $S(\nu)$ at a given frequency ν. At radio

frequencies, the blackbody spectrum is approximated as the Rayleigh-Jeans law:

$$S(\nu)\Omega = \frac{\nu^2 k_B T_b}{c^2}$$

Therefore, the brightness temperature is given by

$$T_b = \frac{c^2 S(\nu)\Omega}{\nu^2 k_B} \tag{2.4}$$

Finally, I define the radiation temperature T_r of a given flux $S(\nu)$ by setting $\Omega = 4\pi$ to get

$$T_r = \frac{4\pi c^2 S(\nu)}{\nu^2 k_B} \tag{2.5}$$

2.3 Radio interferometry

I show here how, by combining the signals received by multiple small separated radio antennas, the source brightness distribution $B(\theta, \phi)$ can be recovered with twice the Rayleigh resolution[1] of a continuous antenna covering the spacings between the small antennas. This technique is known as *interferometry*, and similar techniques are widely applied in experimental physics, most famously as the Michelson interferometer. I begin by considering a simple two-element interferometer where the signals from two antennas are added. I then describe the technique of aperture synthesis [Ryle & Hewish 1960], where multiple antenna elements are placed at different separations to synthesise numerous two-element baselines, which in turn approximately synthesise the two-dimensional resolution of a large antenna covering the area of the small antennas by making use of the Earth's rotation. The ATCA is an aperture synthesis interferometer.

2.3.1 A two element interferometer

Consider Figure 2.2, where parallel radiation from a point source at an effectively infinite distance is detected by the two antenna elements with voltages V_1 and V_2 respectively. The antennas are separated by a distance a, and are observing at a wavelength λ. I treat the situation as one dimensional, in that the source position with respect to the baseline normal is given only by the angle ϕ. The relative phase delay ψ between the received wavefronts at the different antennas is

$$\psi = \frac{2\pi a}{\lambda} \sin\phi \tag{2.6}$$

If we assume a common normalised antenna response $E_0(\phi)$ as a function of sky position ϕ for the two antennas, the *beam patterns* or normalised voltages for a

[1] The Rayleigh resolution of a telescope is defined as the minimum resolvable angular separation of two point sources.

unit source for the two antennas will be

$$\begin{aligned} V_1 &= E_0(\phi)e^{-i\psi/2} \\ V_2 &= E_0(\phi)e^{i\psi/2} \end{aligned}$$

These beam patterns are added to find the beam pattern of the interferometer:

$$V_1 + V_2 = E_0(\phi)\cos(\frac{\psi}{2})$$

Then, the relative power pattern $P(\phi)$ of the interferometer, given by the square of the combined beam pattern, is

$$P(\phi) = |E_0(\phi)|^2 \cos^2(\frac{\psi}{2}) = |E_0(\phi)|^2 \frac{(1+\cos(\psi))}{2} \tag{2.7}$$

The first factor recovers the beam pattern of each element, and the second factor is a set of fringes. The first null of the power pattern is at the first null of the fringe set, which occurs at $\psi = \pi$. The fringe spacing α_f in radians is given by

$$\alpha_f = \frac{\lambda}{a} \tag{2.8}$$

This is the minimum angular separation of two point sources resolvable by this interferometer, or the Rayleigh resolution of the interferometer. The Rayleigh resolution of a single antenna with diameter a is in fact twice this value, ie. $2\lambda/a$ [Kraus 1986].

The relative power pattern is convolved with a source brightness distribution $B(\phi)$ centred at ϕ_0, with extent θ, to derive the actual power pattern $S(\phi)$ of the interferometer as

$$S(\phi) = \int_{-\theta/2}^{\theta/2} B(\phi)P(\phi_0-\phi)d\phi = \frac{1}{2}[S_0 + \int_{-\theta/2}^{\theta/2} |E_0(\phi)|^2 B(\phi)\cos(\frac{2\pi a}{\lambda}\sin(\phi_0-\phi))d\phi] \tag{2.9}$$

where S_0 is the total source flux. If both antennas are tracking the source with the peaks of their beam patterns, we can let $|E_0(\phi)|^2 = 1$. Furthermore, if we assume that the source extent is small ($\phi_0 - \phi \ll \pi$), then $\sin(\phi_0 - \phi) \sim \phi_0 - \phi$ and the expression for $S(\phi)$ is written as

$$2S(\phi) = S_0(1 + V(\phi_0)) \tag{2.10}$$

where

$$V(\phi_0) = V_0 \cos(\frac{2\pi a}{\lambda}(\phi_0 - \Delta\phi)) \tag{2.11}$$

In this formulation,

$$V_0 \cos(\frac{2\pi a}{\lambda}\Delta\phi) = \frac{1}{S_0}\int_{-\theta/2}^{\theta/2} B(\phi)\cos(\frac{2\pi a}{\lambda}\phi)d\phi \tag{2.12}$$

$$V_0 \sin(\frac{2\pi a}{\lambda}\Delta\phi) = \frac{1}{S_0}\int_{-\theta/2}^{\theta/2} B(\phi)\sin(\frac{2\pi a}{\lambda}\phi)d\phi \tag{2.13}$$

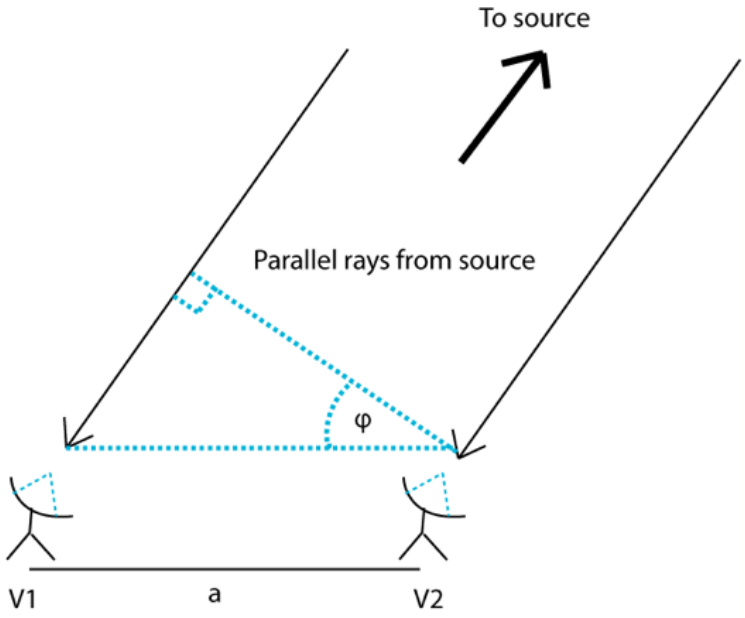

Fig. 2.2: Illustration of a two element interferometer.

Therefore, extending the limits of integration to infinity in the small-source assumption,

$$V_0 e^{\frac{2\pi i a}{\lambda}\Delta\phi} = \frac{1}{S_0}\int_{-\infty}^{+\infty} B(\phi) e^{\frac{2\pi i a}{\lambda}\phi} d\phi \tag{2.14}$$

This quantity is known as the *complex visibility*, and V_0 simply as the *visibility*, or the fringe amplitude. For fringes ranging between V_{min} and V_{max}, the visibility amplitude is given by

$$V_0 = \frac{V_{max} - V_{min}}{V_{max} + V_{min}} \tag{2.15}$$

The complex visibility is part of the $V(\phi_0)$ term in Equation 2.10 for the actual power pattern of a source at position ϕ_0. It is therefore what an interferometer observes, in addition to the base source power S_0.

An inverse Fourier transform can be applied to the complex visibility in terms of the wavelength spacing of the two elements $a_\lambda = a/\lambda$ to recover the brightness of the source at ϕ_0. This is given by

$$B(\phi_0) = S_0 \int_{-\infty}^{+\infty} V_0 e^{-2\pi i a_\lambda(\phi_0 - \Delta\phi)} da_\lambda \tag{2.16}$$

Therefore, by sampling the visibility V_0 at different wavelength spacings a_ϕ, a two element interferometer can recover the brightness distribution of a one-dimensional source $B(\phi_0)$ on varying angular scales $\alpha_f = 1/a_\lambda$. The value of α_f is the size of the *synthesised beam* of an interferometer. Any object smaller than this angular size will, under the inverse Fourier transform, appear as an approximately Gaussian flux distribution peaked at the position of the object with a full width of α_f.

Therefore, when an interferometer, or any telescope for that matter, measures the flux at a point in the sky, it is measured in units of flux per synthesised beam.

2.3.2 Aperture synthesis interferometry

I now develop the treatment of the previous section for a two-dimensional source brightness distribution $B(x, y)$, where I define a Cartesian coordinate system (x,y,z) with the z-axis perpendicular to the plane of the sky. The x-y plane is tangential to the celestial sphere at the point of interest (x, y). I now consider our previous two-element interferometer in a new coordinate system aligned with the x-y-z system, but with axes measured in terms of the wavelength spacings between the antennas along each axis u, v and w corresponding to the x, y and z directions. The complex visibility measured by this interferometer is

$$V(u, v, w)e^{2\pi iw} = \int_{-1}^{1}\int_{-1}^{1} \frac{B(x, y)}{\sqrt{1 - x^2 - y^2}} e^{2\pi i(ux+vy+\sqrt{1-x^2-y^2}w)} dxdy \qquad (2.17)$$

[Kraus 1986] where x and y are unit vectors denoting the source position in the sky, and $z = \sqrt{1 - x^2 - y^2}$. For small x and y (ie. for a small source), $z \sim 1$ and

$$V(u, v, w) = \int_{-1}^{1}\int_{-1}^{1} \frac{B(x, y)}{\sqrt{1 - x^2 - y^2}} e^{2\pi i(ux+vy)} dxdy \qquad (2.18)$$

The visibililty in this case is independent of w. The inverse Fourier transform of this visibility function yields the brightness distribution $B(x, y)$:

$$B(x, y) = \int_{-\infty}^{+\infty} V(u, v)e^{-2\pi i(ux+vy)} dudv \qquad (2.19)$$

An aperture synthesis observation aims to measure the visibility $V(u, v)$ at as many points as possible on the *u-v plane*. This is accomplished by allowing the Earth's rotation to change the orientation of an antenna array with respect to the source. The aperture of a large telescope spanning all individual array elements is synthesised by sampling different points of the u-v plane as the Earth rotates, enabling a better measurement of the brightness distribution of the source at different angular scales at different orientations in the x-y sky plane. In the case of a linear array, 12 hour observations are necessary to sample all orientations, or parallactic angles.

2.3.3 The real world: imaging, interference and data analysis

Given that, in general, actual radio interferometers such as the ATCA do not completely sample the u-v plane, special techniques are necessary to produce radio images that synthesise full u-v coverage. For the ATCA, these techniques are

combined in the software package MIRIAD[2]. First, combining data taken at different observing frequencies close to the frequency of interest within the observing bandwidth allows different points in the u-v plane to be sampled. This is accomplished by, in effect, changing the wavelength separations of the antennas without changing their physical separations. This technique is known as multi-frequency synthesis. Care is needed while using this technique to compensate for the spectral properties of the source and the calibration of the bandpass. Even so, when performing an inverse Fourier transform on the measured visibilities, artefacts due to incomplete u-v coverage will be present. However, a key advantage is that the actual u-v coverage is known, given the known antenna positions. The resulting *point-spread function*, or "dirty" beam of the array, can be calculated. This is the actual appearance of a point source taking the incomplete u-v coverage into account. This dirty beam can be deconvolved from the radio image to produce a "clean" image. An algorithm, known as CLEAN [Högbom 1974], is used to iteratively find the brightest image point within a region and subtract a scaled dirty beam from that point. The points are stored and the synthesised Gaussian beam corresponding to complete u-v coverage is added at these points, restoring the image.

The uncertainty of a flux measurement at a point in a radio image is known as the *sensitivity* of the detection, written as σ. The sensitivity σ of any detection in a radio image is essentiallly the standard deviation of the noise in the image. This is measured by finding regions of the image without any visible sources and calculating the standard deviation of the spread of pixel values. A source is usually considered visible if it is detected to greater than 6σ; therefore, the sensitivity is usually measured in areas where no regions greater than 6σ exist.

The field of view of an interferometric array, such as the ATCA, is defined by the *primary beam* common to the individual dishes of the array. The primary beam is simply the beam pattern of a single dish, and spans a much greater angular size than the synthesised array beam. Much like the synthesised beam, the central lobe of the primary beam also has a Gaussian response. The total primary beam pattern is simply an Airy function.

Calibration of radio interferometric data is necessary to correct and quantify the measurements. Flux and bandpass calibrations using sources with known fluxes and spectra are necessary to set the receiver flux scale and to calibrate the receiver gain in different parts of the observing band. Polarisation calibration using a source with known polarisation properties is also necessary when measuring the polarisation of a target source. We note that polarisation calibration is a complex process that is beyond the scope of this thesis to describe in full. While these calibrations can be done once per observation, using what is known as a *primary calibrator*, the gains of the individual baselines, and the phase errors in the visibil-

[2] http://www.atnf.csiro.au/computing/software/miriad

ity measurements in different baselines caused by atmospheric refraction (seeing) effects, must be corrected on shorter timescales. These necessitate a stable *secondary calibrator* that is observed at intervals during the target (program source) observations. It is especially important that the secondary calibrator be a point source, such that the visibility phases in all baselines must be zero. This allows for phase errors to be accurately measured.

Despite the use of a secondary calibrator, phase errors, particularly in image regions not near the centre of the primary beam, are usually found. The technique used to mitigate this is known as *self-calibration*. Self-calibration relies on the measurement of a quantity known as the closure phase. Consider three baselines between antennas A, B and C − AB, BC and AC − and let the visibility phases measured with these baselines be ϕ_{AB}, ϕ_{BC} and ϕ_{AC}. Assuming that one has accounted for the phase errors due to the time-variable orientation of the array with respect to the source, we still have phase errors due to seeing effects at B and C of δ_B and δ_C relative to antenna A. Then, the phases measured at the three baselines become:

$$\begin{aligned} AB &: \phi_{AB} + \delta_B \\ BC &: \phi_{BC} + (\delta_C - \delta_B) \\ AC &: \phi_{AC} + \delta_C \end{aligned}$$

Adding the AB and BC phases, and taking away the AC phase from the sum, the phase errors cancel and we are left with the closure phase: $\phi_{AB} + \phi_{BC} - \phi_{AC}$. This term, when measured between multiple trios of baselines, can be used to fit out the phase errors in an image.

Radio frequency interference (RFI) is among the major threats to radio astronomy today. A plethora of man-made radio signals, from sources as diverse as mobile phones, microwave ovens, satellites, faulty electrical contacts and car ignition systems, are to be found even in the most radio-quiet, remote locations. This interference is combated through a number of methods. First, a few bands of a few MHz each of the radio spectrum, such as around the neutral hydrogen atomic spin-flip line at 1420.4 MHz, are protected worldwide from man-made transmissions. However, these bands are not useful for modern continuum wideband observations, which utilise bandwidths of up to a few GHz. The second way is to locate telescopes in remote regions, so that the RFI environment is somewhat mitigated. However, inevitably, some RFI is always present and must be removed from the data. This is done by recognising a few key features of most RFI. First, RFI is usually seen only on short timescales, and is much brighter than the background sky emission. Secondly, RFI is commonly found in narrow bandwidths, so that, even if the source one is observing is expected to flare, the flaring emission can usually be isolated by its appearance across a wide bandwidth. Third, when observing with an interferometer, the phase of the complex visibility

measurements of an RFI spike will not be the same across all baselines, but will vary because of the comparitive nearness of the RFI source. Fourth, astronomical sources that actually emit broad-band transients with emission at all frequencies generated at the same time will exhibit dispersion, caused by the column density of interstellar medium electrons between the observer and the source. Dispersion causes lower frequency emission to be delayed with respect to higher frequency emission, and few sources of RFI match the characteristic dispersion behavious of celestial sources.

Characterising periodic transient radio emission from CU Virginis

Abstract

I analyse periodic radio pulses from the magnetic Ap (MCP) star CU Virginis. CU Virginis is the prototypical example of a pulsar-like class of radio transient. ATCA observations at 20 and 13 cm are presented showing, for the first time, twin 100% right-circularly polarised pulses in both bands. I find that the latest optical rotation ephemeris gives a 20% phase delay between our pulses and those detected 10 years previously. I successfully simulate the pulse phases assuming coherent electron-cyclotron maser emission in an idealised magnetosphere geometry. I also report unpolarised, unmodulated quiescent emission at 20 and 13 cm, both in the data presented here and in previous archival data sets. The flux of this emission is correlated with the pulse fluxes over three epochs. A population synthesis of CU Virginis-type radio transients reveals that upcoming 20 cm large-area radio surveys will detect at most 300 similar objects per year. Further, transient searches with next-generation radio telescopes that scan the entire sky every day will detect at most 730 CU Virginis-type transients per year.

3.1 Introduction

The magnetic Ap star CU Virginis (also known as HD124224, hereafter CU Vir) is the best studied (non-pulsar) stellar source of transient radio emission. CU Vir is also classified as a magnetic chemically peculiar (MCP) star; Ap stars refer to any A or B star with 'peculiar' surface abundances of rare earth metals or metalloids. CU Vir has a strong ~ 0.3 T magnetic field and large surface spots of silicon and helium [Khokhlova & Ryabchikova 1970]. The basic properties of CU Vir are presented in Table 3.1. The fast CU Vir rotation period of 0.52 days [Deutsch 1952] and the surface silicon spots further classify this star as an Alpha2 CVn, a set of stars which are characterised by strong, periodic spectroscopic variations (from SIMBAD[1]). CU Vir also possesses a strong, modulated line-of-sight magnetic field lightcurve [Borra & Landstreet 1980], which has led to it being modelled as an oblique magnetic rotator. This model consists of a frozen-in[2] dipole magnetic field offset from the rotation axis [Khokhlova & Ryabchikova 1970]. Furthermore, CU

[1] http://simbad.u-strasbg.fr/simbad/

[2] This is in contrast to dynamo fields, where the fields are aligned with the rotation axes and proportional to the rotation rates.

Property	Value
Position (J2000)	14:12:15.80, +02:24:34.0
Spectral type (1)	B9Si
V magnitude	5.01
Distance	80±6 pc
Rotation period	0.5207 days
Inclination (2)	43 ± 7 degrees
Obliquity (3)	74 ± 3 degrees
Polar magnetic field	3000 ± 200 G
Stellar radius	2.2 ± 0.2 solar radii
Magnetic field strength	3000 ± 600 G
Rotation velocity (4)	195 $\mathrm{km\,s^{-1}}$

Tab. 3.1: Stellar parameters of CU Vir from Trigilio et al. (2000). 1) Note that Ap stars include both A and B type peculiar stars. 2) The inclination of the rotation axis to the line of sight. 3) The angle between the rotation axis and the magnetic axis. 4) The rotation velocity quoted in this paper is the actual maximum tangential rotation velocity, as opposed to a $v \sin i$ velocity.

Vir is believed to have a radiatively driven stellar wind, where thermal radiation from the star drives plasma outwards through radiation and line-absorption pressure [Leto et al. 2006]. The star underwent a 'glitch' event in the year 1984 (MJD 45999.5) [Pyper et al. 1998] where the rotation period suddenly increased by 0.005%. No attempt at a measurement of a change in the spin-down of the star was made. This event is so far not conclusively explained [Stępień 1998], though models ranging from a violent emptying of the inner magnetosphere to an internal mass re-arrangement have been proposed [Trigilio et al. 2008].

Quiescent radio emission on the order of a few millijansky is observed in some MCP stars in spectra peaking at 6 cm [Drake et al. 1987]. The number of known MCP stars that are radio emitters is small. For instance, Leone, Trigilio & Umana (1994) detected six out of 60 MCP stars observed at 6 cm to sensitivities of $\sigma \sim 100\,\mu$Jy. The radio spectrum of CU Vir has recently been extended to millimetre wavelengths [Leone et al. 2004], and appeared to be flat [Leone, Umana & Trigilio 1996], with a variable degree of circular polarisation at 6 cm and 3 cm ranging up to 15% at 6 cm [Leone, Trigilio & Umana 1994]. This quiescent emission from MCP stars has been modelled by Trigilio et al. (2004) as gyrosynchrotron emission caused by non-thermal electrons accelerated towards the magnetic poles from the magnetosphere plasma. Acceleration is assumed to occur because of magnetic reconnection events in current sheets on the magnetic equator. This acceleration mechanism is well studied [Usov & Melrose 1992]. Leto et al. (2006) successfully applied the Trigilio et al. (2004) MCP quiescent radio emission model to CU Vir. Chapter 4 includes an in-depth discussion of the quiescent emission and the CU Vir magnetosphere.

Three observations of CU Vir at 20 cm over full rotation periods have each revealed a pair of short duty-cycle, 100% circularly polarised, high brightness temperature ($> 10^{12}$ K) pulses [Trigilio et al. 2000, Kellett et al. 2007, Trigilio et al. 2008]. The pulses are separated by roughly 40% in phase. Fluxes peak at ∼10 mJy. The pulse separations are stable over timescales of years, though variations in the shapes of the peaks and their rotation phase with respect to the optical ephemeris of Pyper et al. (1998) are apparent [Trigilio et al. 2008]. Trigilio et al. (2008) also reported a ∼10 mJy, circularly-polarised pulse at 13 cm that appeared to peak 25 minutes before the pulse was observed at 20 cm. No evidence for pulses has been seen at higher frequencies [Trigilio et al. 2000], although a slight increase in the circular polarisation fraction at the corresponding rotation phases at 6 cm has been observed. The pulses have been interpreted as tightly beamed coherent emission from an electron-cyclotron maser (ECM) system [Trigilio et al. 2008]. The non-thermal electron flow feeding this mechanism is believed to be the same one that causes the quiescent emission [Leto et al. 2006].

Here, I aim to characterise CU Vir as the prototypical example of a class of radio transient. The incidence of transient radio emission across a variety of stars provides valuable insights into the evolution, atmospheres and magnetic fields of stars. Non-pulsar stellar radio transients offer a variety of physical probes into the pulsar emission mechanism. Upcoming large-area radio continuum and transient surveys will greatly expand the stellar radio transient sample, both in source numbers and classes.

The CU Vir pulses share numerous commonalities with pulsar emission, including their origin in a magnetised plasma, short duty-cycles and coherent emission mechanism. Understanding the pulsar emission mechanism has proved challenging because of the lack of observational constraints on the neutron star magnetosphere. However, in the case of CU Vir, the magnetic field, the plasma in the magnetosphere and properties of the electron acceleration mechanisms can all be probed using multiple independent techniques, enabling the emission physics to be highly constrained.

While CU Vir is so far unique among MCP stars in producing pulsed radio emission, no search for pulses from other MCP stars at 20 and 13 cm has been published to date. It is expected that a number of similar objects will appear in large-scale continuum and transient surveys by future radio synthesis arrays such as the Australian Square Kilometre Array Pathfinder (ASKAP) [Johnston et al. 2008]. It is therefore important to understand how many CU Vir-type transients could be observed.

The structure of this chapter is as follows. In §2 I outline the observing and analysis techniques used to detect transient emission from CU Vir with the ATCA. In §3 I describe and analyse the detection of pulsed and quiescent emission from CU Vir at 20 and 13 cm. In §4 an ECM emission model for the pulses is developed and discussed and finally in §5 I estimate how many sources similar to CU Vir

could be detected in upcoming radio surveys.

3.2 Observing and data analysis

CU Vir was observed with the ATCA on 2008 October 31 over a nine hour timespan. A dual-band receiver providing two 128 MHz bandwidths centred on 1.380 GHz (20 cm) and 2.638 GHz (13 cm) was used, with an on-source integration time of 7.75 hr. Data were recorded in 32 channels across each of the 128 MHz bandwidths, with integration times of 10 seconds per cycle. The entire array consisting of the six 22-metre dishes was used in the fully 6A configuration. This configuration offers a set of long baselines that are optimised to reduce source confusion from extended emission. Calibrations were obtained from the ATCA primary calibrator PKS 1934−638, and five minute observations of the secondary calibrator PKS 1416−067 at 20 minute intervals. The phase centre of these observations was placed 10" south of the position reported for CU Vir in Trigilio et al. (2008) in order to avoid the possibility of image artefacts at the ATCA pointing centre due to correlator offsets.

I carried out the data reduction using the MIRIAD software package. Narrowband and short-timescale RFI was removed from the visibilities, along with any short-timescale amplitude excursions in the secondary calibrator data. Flux, bandpass and polarisation calibrations were obtained from PKS 1934−638. Gain and phase calibrations were obtained from PKS 1416−067. CU Vir was subsequently imaged out to three primary beam FWHM[3], in order to allow effective subtraction of all sources in the field. The two strongest nearby sources, PKS 1409+031 and TXS 1410+027 were individually 'peeled' from the visibilities [Noordam 2004]: the phase centres were shifted to their positions, self-calibration techniques were applied using the MIRIAD task GPSCAL to optimise the calibrations towards each source, and the final source models constructed using the MIRIAD CLEAN task were subtracted from the visibilities. The phase centres were then shifted to the position of CU Vir, and CLEAN models of all other sources detected to greater than 6σ within one primary beam FWHM were subtracted from the visibilities. The four shortest baselines at 20 cm were also removed from the visibilities because confusion from extended emission was not well represented in the CLEAN models.

Initial lightcurves of CU Vir were then constructed by vector averaging the visibility Stokes V amplitudes over three minute intervals. The visibility amplitudes, measures of the fringe heights, are directly proportional to the source flux (see Chapter 2). These lightcurves allowed the identification of the pulse timespans. The field was subsequently imaged to one primary beam FWHM (34' and 20' at 20 and 13 cm respectively) using only off-pulse data. The off-pulse quiescent emission in both observing bands was modelled using CLEAN and subtracted from

[3] Full Width Half Maximum

	Epoch A	Epoch B	Epoch C
Date (UT)	29/05/99	29/08/99	31/10/08
Timespan (hrs)	9.3	9	9
ATCA config.	6A	6D (1)	6A
20 cm Q	Yes	Yes	Yes
13 cm Q	Yes	No	Yes
20 cm P	2	2	2
13 cm P	1	0	2

Tab. 3.2: Basic parameters and detections from the three datasets analysed. Q: quiescent detections. P: Number of pulses detected. 1) The 6D configuration is very similar to the 6A configuration, but with more configurations of shorter lengths.

the visibilities. 'Cleaned' images of the quiescence were constructed by convolving Gaussian beams with the CLEAN models using the MIRIAD task RESTOR. Finally, lightcurves consisting only of the pulses were constructed in all Stokes polarisations by vector-averaging the visibilities in bins of three minutes as before, and plotting the real components. The time averaging interval was chosen to form pulses with a signal-to-noise ratio of at least six.

Throughout this thesis I adopt the Institute of Electrical and Electronics Engineers (IEEE) convention on the sign of Stokes V (1969, Standard Definitions of Terms for Radio-Wave Propagation, IEEE Trans. AP-17, 270). Positive Stokes V corresponds to right-circular polarisation. A right-circularly polarised wave propagates with a wavevector rotating counter-clockwise when viewed along the line of sight.

This analysis procedure was repeated for archival observations obtained in 1999 with the ATCA [Trigilio et al. 2008]. A summary of the observations analysed and the pulse and quiescent detections is presented in Table 3.2. I note for future reference that I analysed observations of CU Vir from three epochs: Epoch A (29th May 1999), Epoch B (29th August 1999) and Epoch C (31st October 2008). Data from Epochs A and B were collected by Trigilio et al. (2008), and the Epoch C observations, described above, were conducted by my supervisors and collaborators.

3.3 Results

3.3.1 Properties of the radio pulses

I detected pulses at both observing frequencies for Epoch C, and re-detected the pulses reported for Epochs A and B by Trigilio et al. (2008). I confirm the ∼100% circular polarisation of the pulses. The pulses appear in positive Stokes V, implying right-circular polarisation. These most recent detections are striking in that, in

	20 cm	13 cm
Peak fluxes: Stokes I (mJy)	9.38±1.75, 11.47±1.75	11.59±1.37, 9.62±1.37
Pulse widths (minutes)	39	51, 48
Pulse separations (minutes)	303	261
Stokes V percentage	115±17, 101±14	104±11, 99±14
Linear pol. limit $\sqrt{Q^2+U^2}/I$ (%)	13, 10	9, 10

Tab. 3.3: Parameters of the pulses detected during Epoch C.

contrast with those during Epochs A and B [Trigilio et al. 2008], twin pulses were observed in *both* observing bands, with the first and second 13 cm pulses arriving later and earlier with respect to their corresponding 20 cm pulses. This effect was noted by Trigilio et al. (2008) for the one pulse detected at 13 cm in Epoch A; this pulse arrived earlier than its corresponding 20 cm pulse. Images showing the Epoch C pulse detections appear in Figures 3.1 and 3.2, and parameters of the pulses from Epoch C, including their strengths, separations and polarisation fractions are presented in Table 3.3. The errors quoted for the fluxes are the rms of the off-pulse parts of the lightcurves. All time errors are 3 minutes (the averaging time). The linear polarisation limits are the rms of the $\sqrt{Q^2+U^2}$ lightcurves as a percentage of the Stokes I peaks. The pulse width given for the 20 cm lightcurve is for the second pulse detected.

The lightcurves, constructed as described in Section 3.2, were averaged across all epochs, with all lightcurves aligned in phase. These are shown in Figure 3.3 for all polarisations (Stokes I, V and $\sqrt{Q^2+U^2}$). These represent the average folded pulse profiles of CU Vir. These lightcurves consist only of the pulses, with all quiescent emission removed along with other sources in the field.

3.3.2 Quiescent emission from CU Vir at 20 and 13 cm

The off-pulse images of CU Vir show quiescent emission in both observing bands in all but one case (13 cm emission was not detected during Epoch B). The emission was detected to at least 6σ in all cases, and appears as point sources coincident with the position of CU Vir. The emission was highly variable between epochs, ranging from 1.6 to 2.7 mJy at 20 cm and zero to 3.7 mJy at 13 cm. The off-pulse emission was found to be randomly polarised (within noise levels). In these observing bands the off-pulse fluxes appeared constant over the observing timespan, in contrast to the higher frequency emission that is modulated with the rotation period [Trigilio et al. 2000].

The quiescent detections and image noise are presented in Table 3.4, and the corresponding images appear in Figures 3.4 (Epoch A), 3.5 (Epoch B) and 3.6 (Epoch C). The fluxes were measured by fitting a two-dimensional elliptical Gaussian to the images using the MIRIAD IMFIT task and measuring the integrated

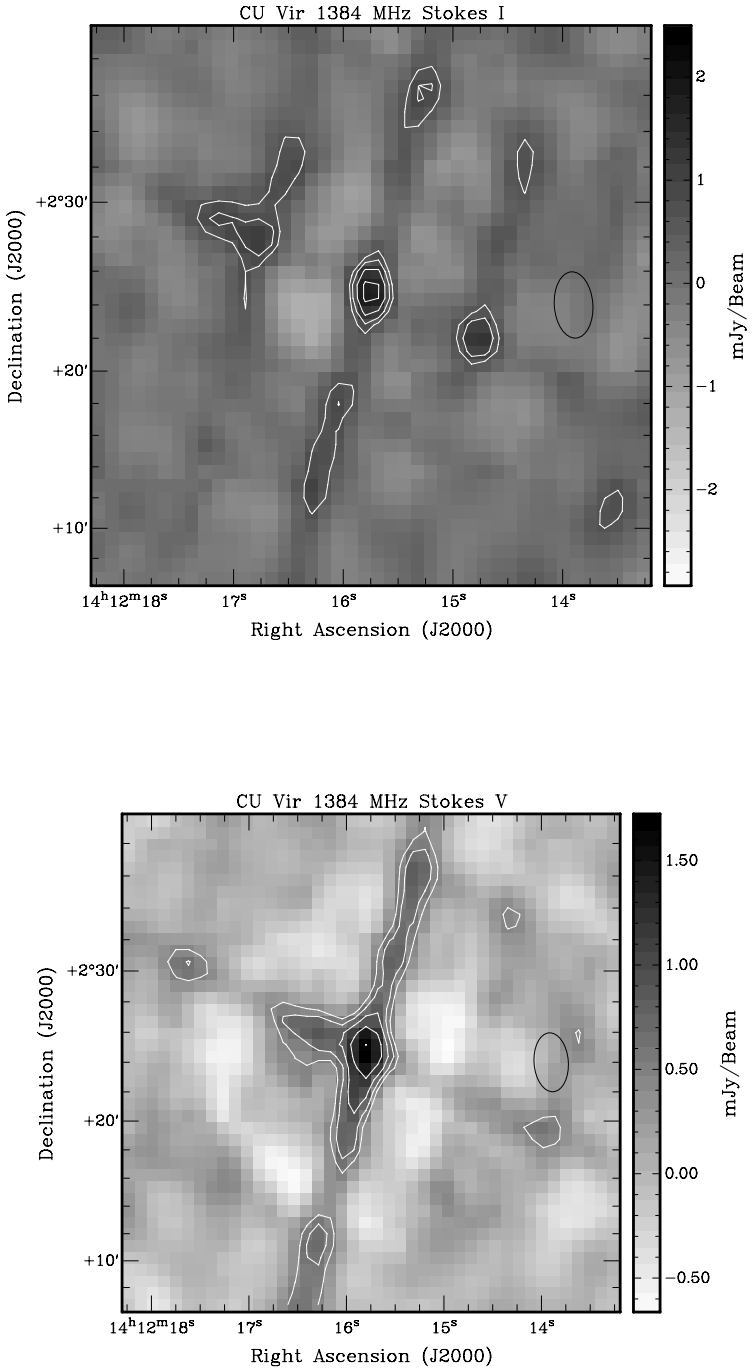

Fig. 3.1: Stokes I (top) and V (bottom) images of the pulsed emission from CU Vir at 20 cm. The peak flux in each image is (from top): 2.49 mJy/beam and 1.72 mJy/beam. Contours begin at a fourth of the peak fluxes and increase in factors of $\sqrt{2}$. All background sources and quiescence from CU Vir have been subtracted. The synthesised beam FWHM are displayed to the right of the images, and the greyscale bars beside the images give the flux scale in mJy/beam. Note the presence of the two 'fan' beams crossing at the centres of the images: these represent the instantaneous synthesised beams when the pulses appeared, and have not been deconvolved from the images.

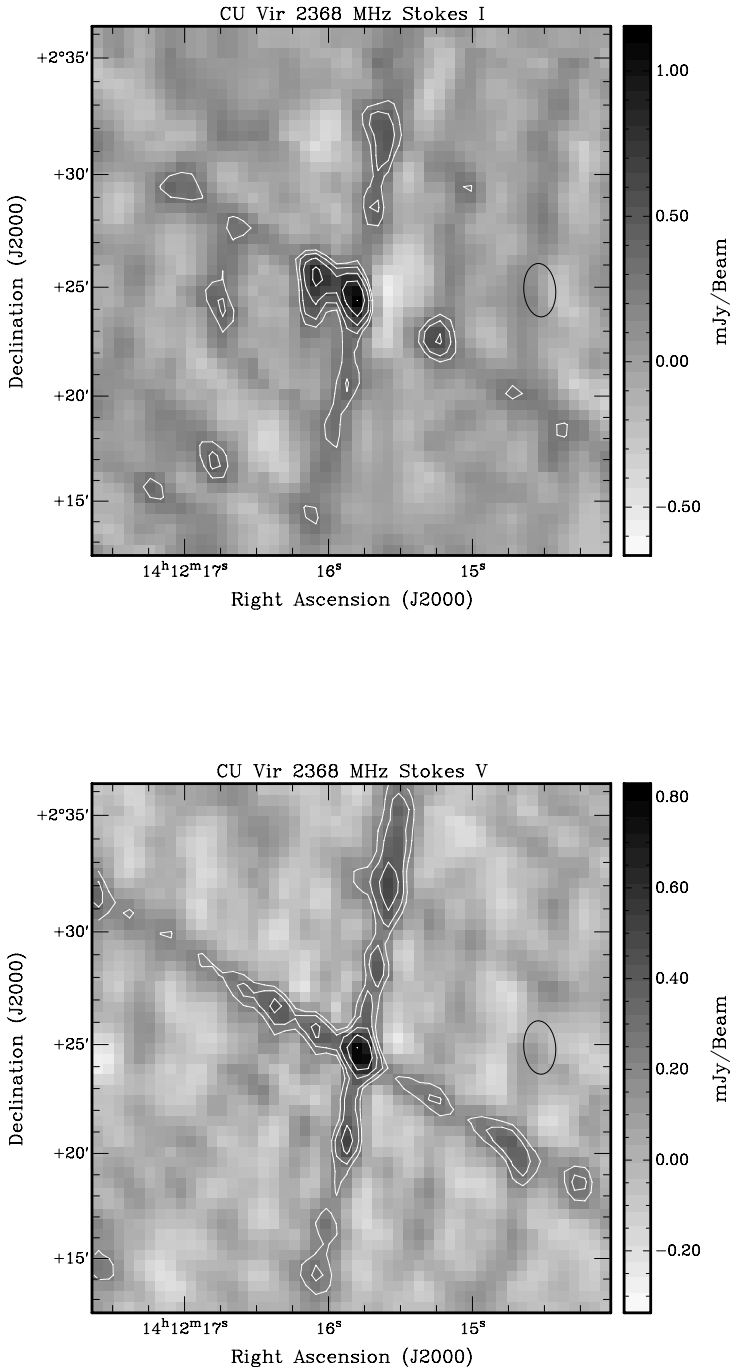

Fig. 3.2: Stokes I (top) and V (bottom) images of the pulsed emission from CU Vir at 13 cm. The peak flux in each image is (from top): 1.15 mJy/beam and 0.83 mJy/beam. Contours begin at a fourth of the peak fluxes and increase in factors of $\sqrt{2}$. All background sources and quiescence from CU Vir have been subtracted. The synthesised beam FWHM are displayed to the right of the images, and the greyscale bars beside the images give the flux scale in mJy/beam. Note the presence of the two 'fan' beams crossing at the centres of the images: these represent the instantaneous synthesised beams when the pulses appeared, and have not been deconvolved from the images.

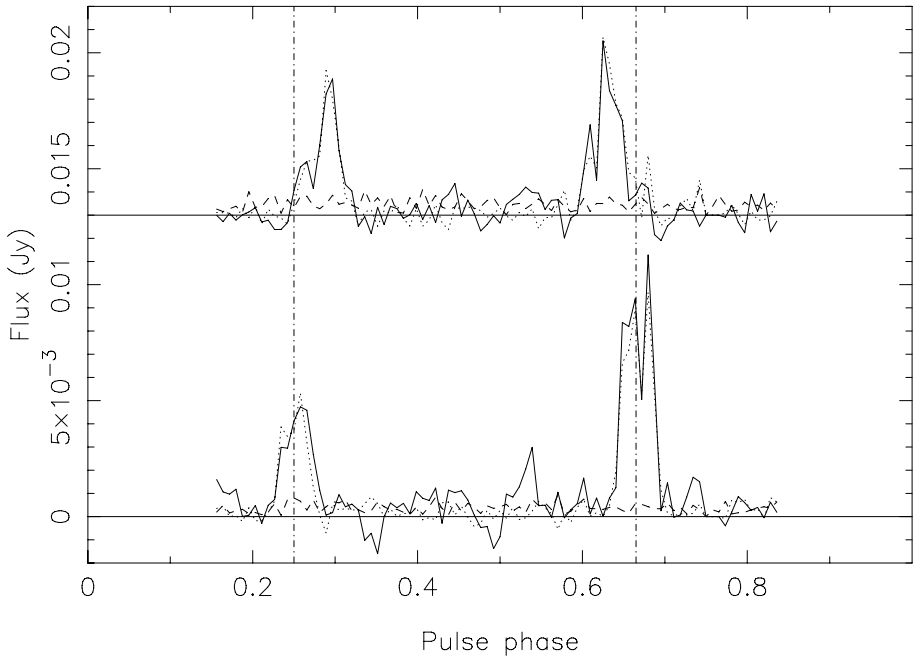

Fig. 3.3: Pulse profiles at 13 cm (top plot; offset by 13 mJy) and 20 cm (lower plot) obtained by aligning and averaging the light curves from Epochs A, B and C. The pulse phase axis is chosen so as to centre the pulses. I plot Stokes I (solid curves), Stokes V (dotted) and $\sqrt{Q^2 + U^2}$ (dashed). The vertical dot-dashed lines represent the visual centres of the pulses at 20 cm. Note that the pulses at 13 cm are closer together than those at 20 cm. All sources, including the quiescent emission from CU Vir, have been subtracted. Time-binning is in 128 bins across a pulse period of 0.5207 days.

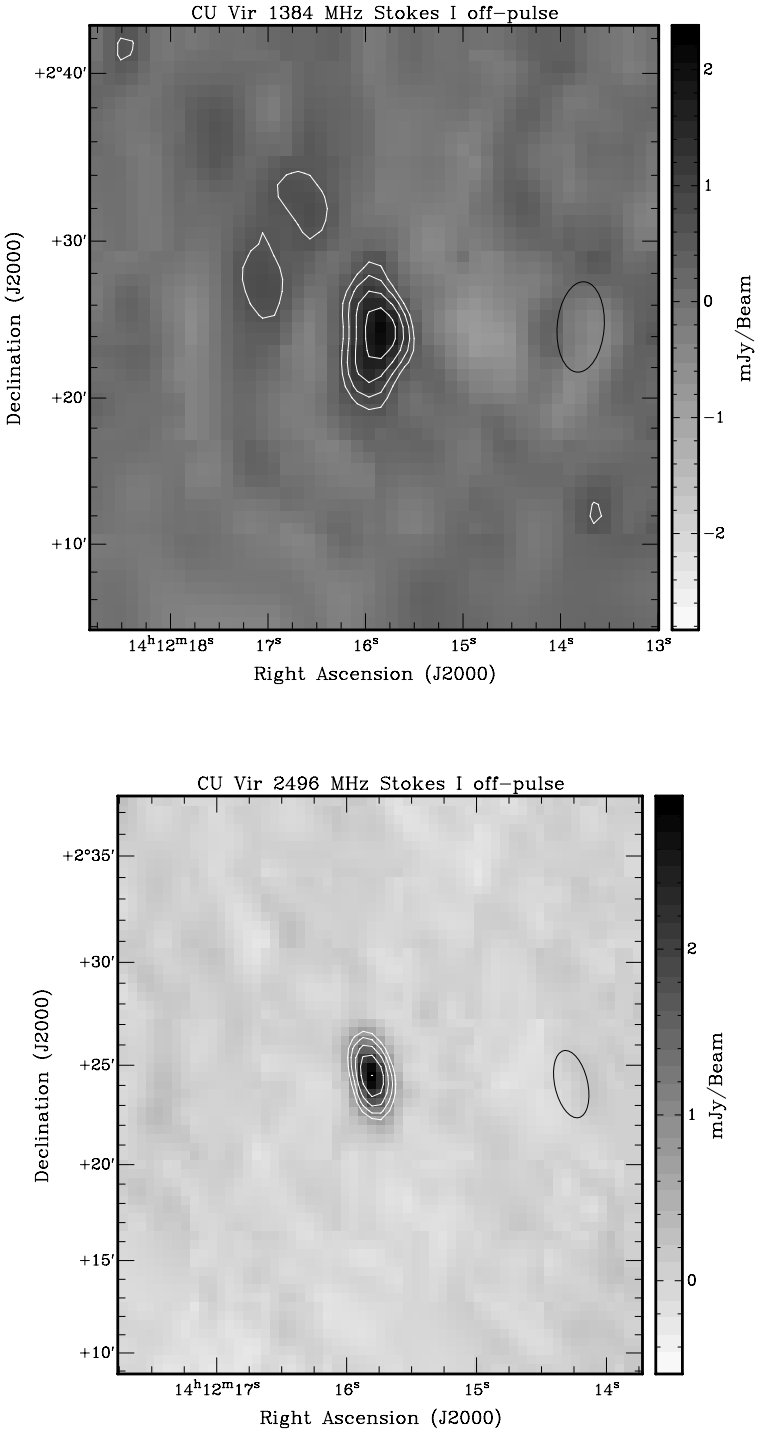

Fig. 3.4: Total intensity radio images of the off-pulse emission from CU Vir during Epochs A at 20 (top) and 13 cm (bottom). The peak flux (and rms noise in mJy/beam) in each image is (from top): 2.37 mJy/beam (0.250) and 2.92 mJy/beam (0.076). Contours begin at a fourth of the peak fluxes and increase in factors of $\sqrt{2}$. The synthesised beam FWHM are displayed on the right of each image, and the greyscale bars beside each image show the flux scale in mJy/beam.

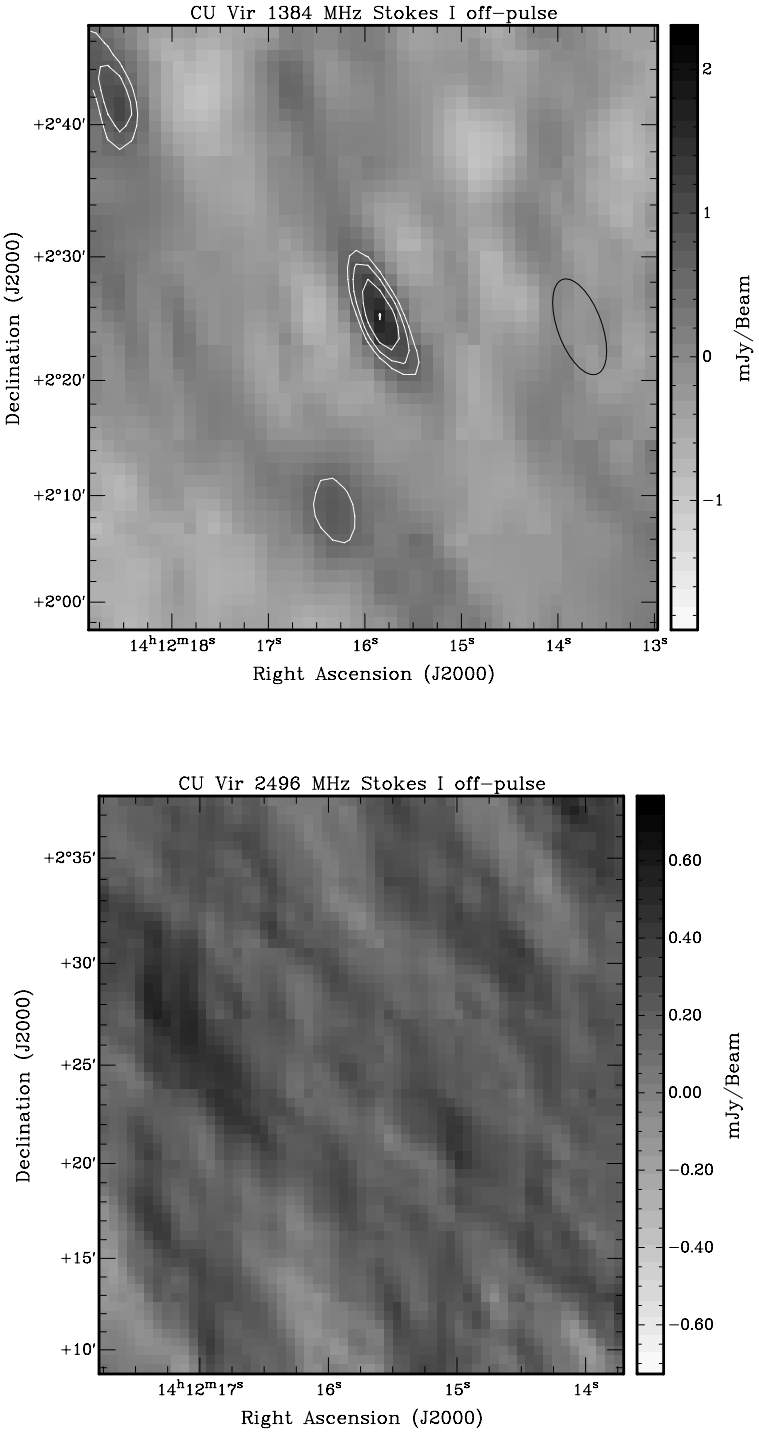

Fig. 3.5: Total intensity radio images of the off-pulse emission from CU Vir during Epoch B at 20 (top) and 13 cm (bottom). The peak flux (and rms noise in mJy/beam) in each image is (from top): 2.30 mJy/beam (0.266) and (none) (0.103). Contours begin at a fourth of the peak fluxes and increase in factors of $\sqrt{2}$. The synthesised beam FWHM are displayed on the right of each image, and the greyscale bars beside each image show the flux scale in mJy/beam.

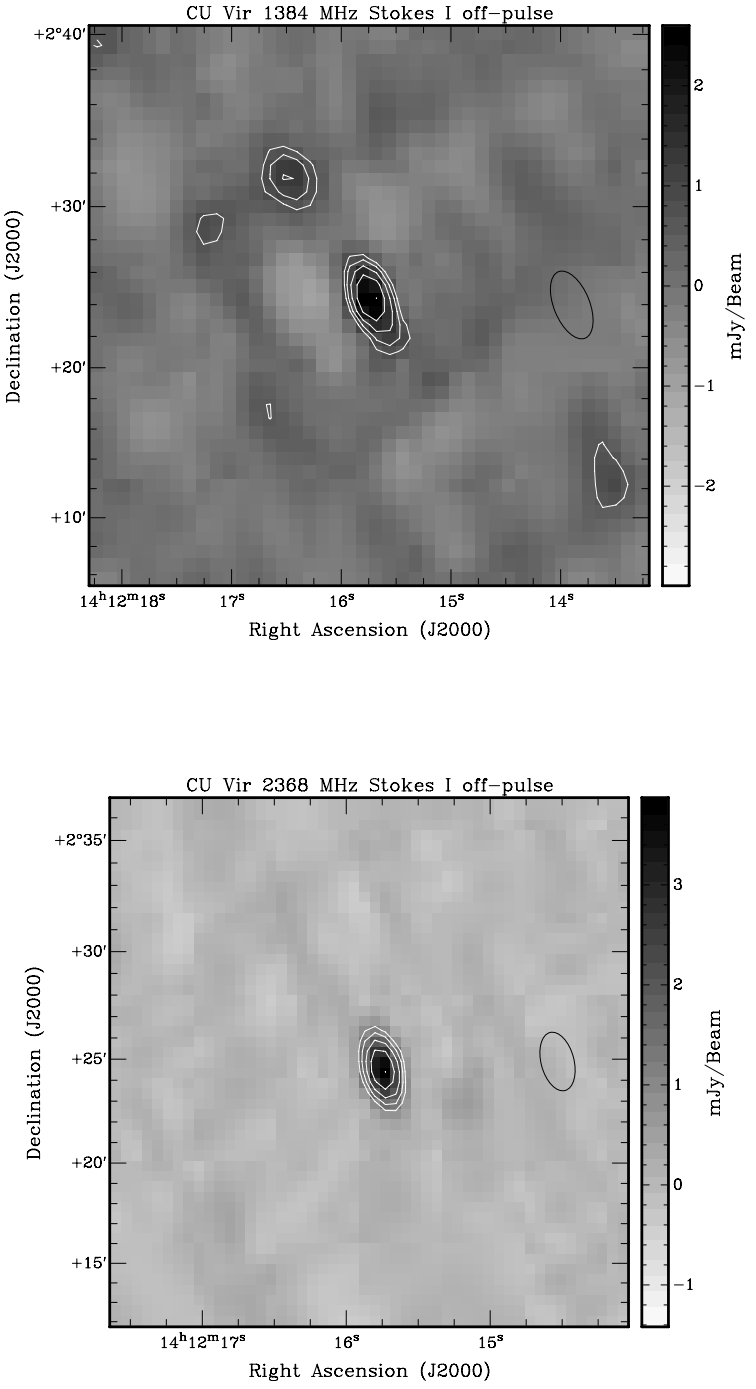

Fig. 3.6: Total intensity radio images of the off-pulse emission from CU Vir during Epoch C at 20 (top) and 13 cm (bottom). The peak flux (and rms noise in mJy/beam) in each image is (from top): 2.59 mJy/beam (0.194) and 3.86 mJy/beam (0.131). Contours begin at a fourth of the peak fluxes and increase in factors of $\sqrt{2}$. The synthesised beam FWHM are displayed on the right of each image, and the greyscale bars beside each image show the flux scale in mJy/beam.

flux. The rms values for the images were computed by masking the inner parts of the images to a radius of two synthesised beams from the centre, and calculating the rms flux of the resultant images.

These detections represent an extension of the quiescent radio spectrum of an MCP star to wavelengths greater than 6 cm. The 13 cm quiescence is the first such detection for an MCP star. While Linsky, Drake & Bastian (1992), and Leone et al. (1996) report 20 cm fluxes for a number of MCP stars, conclusive evidence that this emission was quiescent was not published. Leone et al. (1996) also detected 20 cm emission from CU Vir, which was seen in the off-pulse parts of CU Vir lightcurves of Trigilio et al. (2000). However, we make the first attempt at isolating the quiescence by subtracting other field sources and the pulses.

The measurements made here, when plotted on a spectrum of CU Vir assembled using fluxes from Trigilio et al. (2000) and Leone et al. (2004) (Figure 3.7), indicate that the relatively flat spectrum turns over at lower frequencies. In particular, the difference in flux between the 13 and 20 cm measurements during Epochs A and C remains approximately constant. However, conclusions about the spectral turnover cannot be reached without simultaneous measurements across multiple radio bands, because of the variability of the radio flux at most frequencies on timescales of years [Leone et al. 2004]. The cause of this variability is unclear at present.

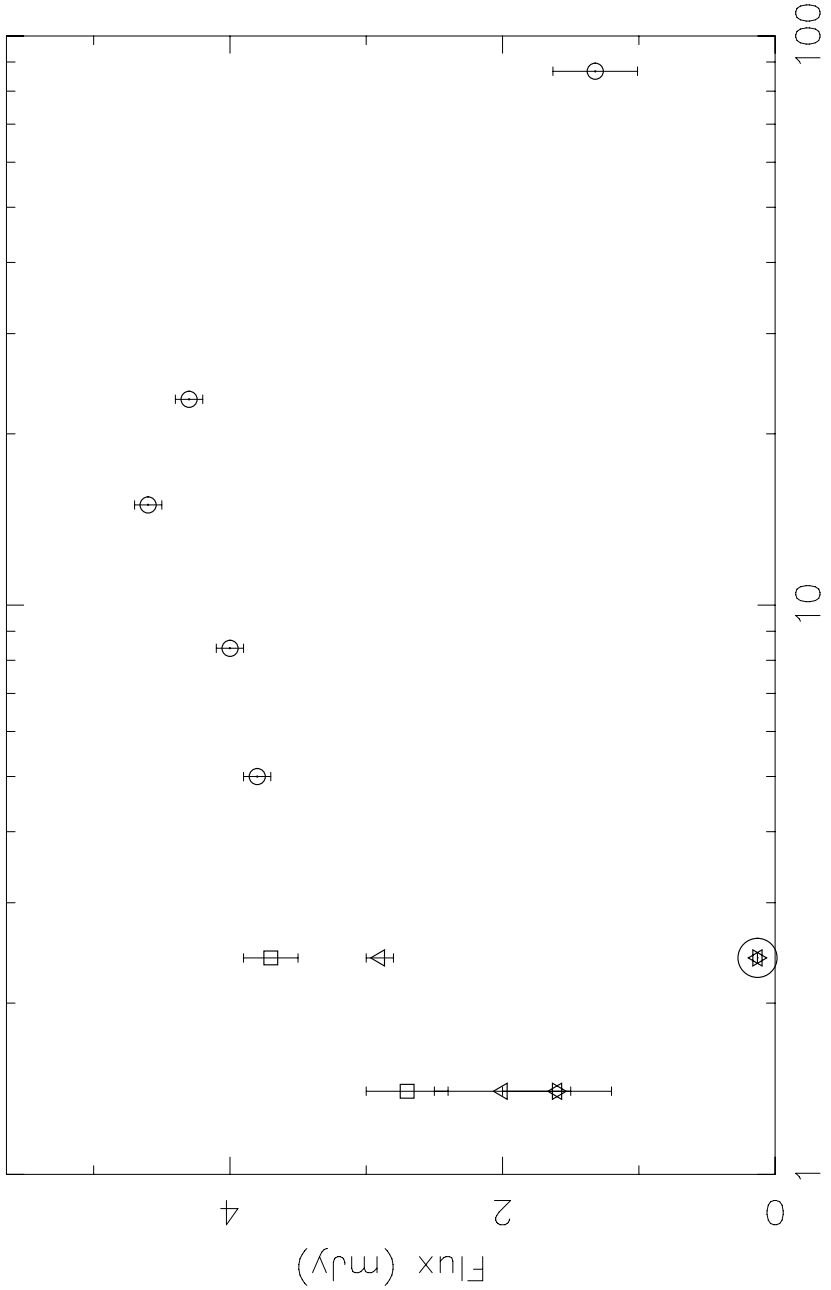

Fig. 3.7: The quiescent Stokes I radio spectrum of CU Vir over a number of epochs. The circles are averaged data from Trigilio et al. (2000), except for the 87.7 GHz point, which is from Leone et al. (2004). These data were not simultaneous, and were taken over 6 years. The triangles, stars and squares are simultaneous 20 and 13 cm data from Epochs A, B and C respectively. The circled star represents the 13 cm non-detection during Epoch B; its value is that of the image noise.

	Epoch A	Epoch B	Epoch C
20 cm flux (mJy)	2.0	1.6	2.7
20 cm rms (mJy)	0.250	0.266	0.194
13 cm flux (mJy)	2.90	0.0	3.70
13 cm rms (mJy)	0.076	0.103	0.131

Tab. 3.4: Fluxes and image rms sensitivities of the quiescent detections.

Epoch	Date	Q_{20}	P_{20}	Q_{13}	P_{13}
A	29/05/99	2.0±0.3	6±1	2.90±0.08	5±1
B	29/08/99	1.6±0.3	2±1	±0.1	±1
C	31/10/08	2.7±0.2	10±1	3.7±0.1	10±1

Tab. 3.5: Variability of the 20 cm and 13 cm Stokes I quiescent ($Q_{20,13}$) and average pulse ($P_{20,13}$) fluxes (in mJy) over Epochs A, B and C.

3.3.3 The correlated flux variability of the pulses and quiescence

The variability of the quiescent emission with time mirrors the variability in the strengths of the pulses. An inspection of Table 5 − a list of the average Stokes I pulse strengths at each epoch along with the quiescent detections at each epoch for both observing bands − shows a clear trend: the stronger the pulsed emission, the stronger the quiescent emission. The absence of a quiescent detection at 13 cm during Epoch B corresponds to an essentially non-existent pulse at this wavelength and time. I argue that scintillation is not the cause of the variability. While scintillation effects, due to interstellar medium density variations with time, can model the simultaneous drop in intensity of emission at both frequencies between Epochs C and A, they cannot model the lack of emission at 13 cm during Epoch B. Therefore, I infer that the quiescent emission mechanism and the coherent pulse emission mechanism are linked. This link could be caused by the same stream of non-thermal electrons feeding both mechanisms, or by perturbations in the magnetosphere that affect both types of emission. The former case is supported by the variability of the spectral index of the quiescent emission (see Figure 3.7): this implies a variable non-thermal electron flow with fresh injections of electrons.

3.3.4 A rotational anomaly in the pulse arrival times

The time-evolution of the pulse phases (calculated using the ephemeris of Pyper et al. 1998) was investigated by Trigilio et al. (2008), who reported phase delays of the radio lightcurves with respect to observations in June 1998 [Trigilio et al. 2000] of 0.012 and 0.018 for Epochs A and B respectively. This was interpreted as a sudden change in the rotation period of CU Vir of ∼1 second between June 1998 and Epoch A. This change was taken to be analogous to the change reported by

Pyper et al. (1998) that occured circa 1984. The Epoch C observations of the CU Vir pulses provided a means to test the period change hypothesised by Trigilio et al. (2008).

Figure 3.8 shows the five lightcurves (Epochs A, B and C for 20 cm, and Epochs A and C for 13 cm) with detected pulses, plotted against the rotation phase derived from the ephemeris of Pyper et al. (1998). The pulse peaks measured by Trigilio et al. (2000) during June 1998 are also included. The delay of the pulses is clear, particularly those during Epoch C.

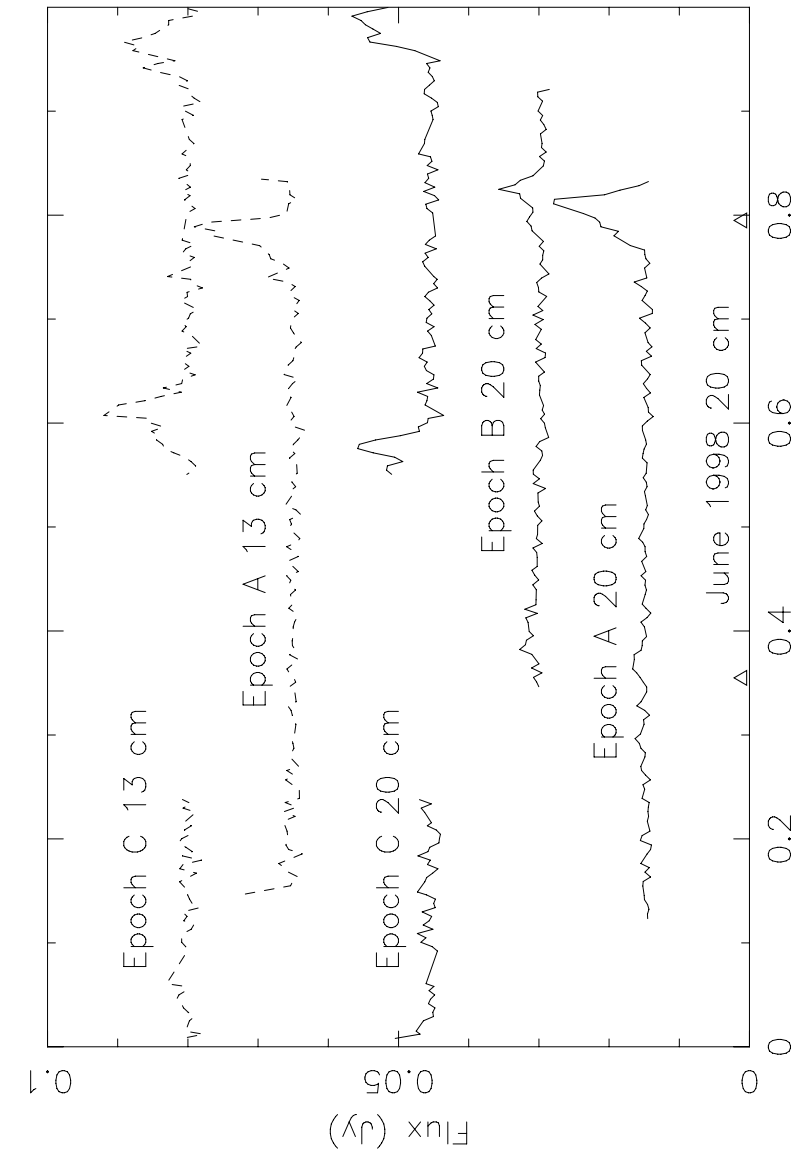

Fig. 3.8: Stokes V pulse lightcurves constructed from our analysis of Epoch A, B and C data plotted against the rotation phase based on the latest ephemeris of Pyper et al. (1998). The lightcurves, with flux increments added, are, from bottom to top: Epoch A, 20 cm (+15 mJy); Epoch B, 20 cm (+30 mJy); Epoch C, 20 cm (+45 mJy); Epoch A, 13 cm (+65 mJy); Epoch C, 13 cm (+80 mJy). The triangles at the bottom of the plot are the Stokes I peaks from Trigilio et al. (2000) measured during June 1998. The time-averaging is on three minute intervals. The solid lines are the 20 cm lightcurves, and the dashed lines are the 13 cm lightcurves. The Epoch C pulses are delayed by 2.44±0.05 hours with respect to the June 1998 ones.

TOA (MJD)	ν_{obs} (GHz)	Epoch	Reference
50966.159(8)	1.425	June 98	Trigilio et al. (2000)
51327.535(3)	1.380	A	Trigilio et al. (2008)
51419.189(3)	1.380	B	Trigilio et al. (2008)
54770.007(3)	1.380	C	this paper
54770.007(3)	2.368	C	this paper

Tab. 3.6: List of TOAs with references derived from all lightcurves of CU Vir, with last decimal place errors in brackets.

To quantify this delay, I attempt to fit an updated rotation period to the data. The times of arrival (TOAs) of the phase centres of the lightcurves were taken as the centres of the twin pulses. TOAs were only measured where pairs of pulses were present (June 1998, and Epochs A, B and C at 20 cm and Epoch C at 13 cm), and are listed in Table 3.6. The data were then fitted to a simple expression for the number of periods, N, as a function of the time, t, since the first observed TOA at t_0:

$$N = \nu_r(t - t_0) \tag{3.1}$$

where ν_r is the rotation frequency. The period was measured with respect to the same epoch used in Pyper et al. (1998) (MJD 35178.1417). The fit was conducted so as to minimise the rms error between subsequent TOAs and the corresponding expected TOAs, using the pulsar timing package TEMPO2 [Hobbs, Edwards & Manchester 2006]. Frequency dispersion was ignored because of the coarse time sampling. A period derivative was not measurable with the current data. The resulting best-fit period was $44989.967 \pm 0.008\,s = 0.52071721 \pm 9 \times 10^{-8}\,days$. This is 1.221 ± 0.008 seconds slower than that of Pyper et al. (1998). The residuals of fits of the TOAs to the period of Pyper et al. (1998) are shown in Figure 3.9.

Three possible explanations for this result are that:

- A glitch event, such as that reported by Pyper et al. (1998), occured before June 1998 (when Trigilio et al. 2000 first observed pulses from CU Vir).

- The ephemeris of Pyper et al. (1998) does not accurately represent the rotation of CU Vir, or

- The radio and optical lightcurves do not have the same periods.

Further monitoring is necessary to characterise the observed trend.

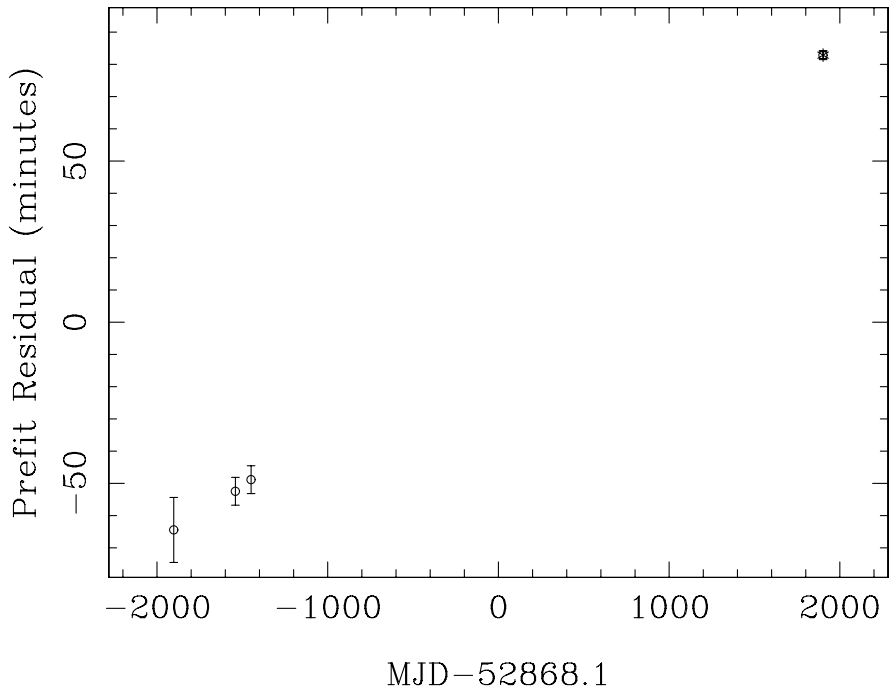

Fig. 3.9: Pre-fit residuals of the CU Vir pulse TOAs. The pre-fit residuals are the differences between the expected TOAs from the period of Pyper et al. (1998), and the measured TOAs listed in Table 3.6. The two Epoch C residuals (at top right) appear on top of each other.

3.4 An ECM model for the pulsed emission

The Epoch C observations clearly show that the CU Vir pulse profiles at both 20 and 13 cm have two distinct peaks. The peaks are closer in phase at 13 cm than at 20 cm and share the same phase centre. The 20 cm peaks were shown by Trigilio et al. (2000) to be symmetric about a magnetic pole of CU Vir, by comparing the CU Vir magnetic field lightcurves measured by Borra & Landstreet (1980) and the pulse lightcurve in phase. The Epoch C observations provide further evidence that the geometry of the pulse emission region is centred on this magnetic pole.

The pulsed emission from CU Vir has been hypothesised to be caused by an electron-cyclotron maser (ECM) mechanism [Trigilio et al. 2000; Leto et al. 2006; Kellett et al. 2007; Trigilio et al. 2008]. The electron distributions necessary for an ECM in the CU Vir magnetosphere are thought to arise upon the magnetic mirroring of large pitch angle non-thermal electrons flowing towards the magnetic poles [Kellett et al. 2007; Trigilio et al. 2008]. These electrons are accelerated on the magnetic equator beyond the Alfvén radius [Leto et al. 2006]. The Alfvén radius is defined as the point beyond which the stellar wind radial speed exceeds the Alfvén speed $v_A = B_r/\sqrt{\mu_0 \rho}$ (B_r is the radial magnetic field component and ρ is the local plasma density). Generally, the Alfvén radius is also where the kinetic energy density of the stellar wind becomes greater than the magnetic energy density of

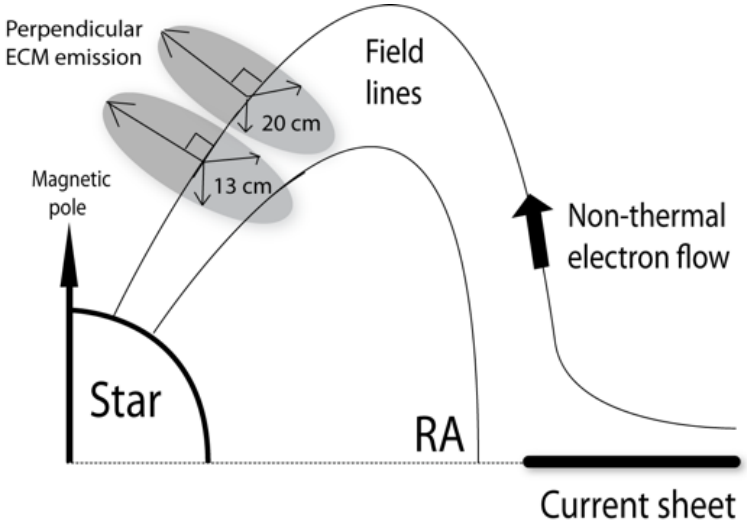

Fig. 3.10: Illustration of the assumed magnetosphere geometry of CU Vir. The Alfvén radius RA is between 12 and 17 stellar radii (Leto et al. 2006). The non-thermal electron flow from the current sheet is indicated by a thick arrow. The ECM emission, indicated by thin arrows and perpendicular emission sheets, is beamed at $\theta = 90°$ to the field lines. The 20 cm emission originates in regions of lower field strength than the 13 cm emission, further away from the star.

the dipole field.

Here, I test models of the CU Vir magnetosphere and coherent emission suggested by Kellett et al. (2007), Leto et al. (2006) and Trigilio et al. (2008) by simulating the pulse lightcurves from the model geometry. The following assumptions are made:

- The magnetic field is a dipole centred at the centre of the star.
- The non-thermal electron flow from the current sheets is symmetric about the magnetic poles and occupies the field lines beyond the last closed field lines.[4]
- The flow is only mildly relativistic, with a low-energy Lorentz factor cutoff of $\gamma \sim 1.02$ (corresponding to 10 keV electrons) and a power law energy spectrum [Leto et al. 2006].

ECM emission is tightly beamed. The negligible relativistic effects imply that the beaming angle[5] θ is related to the mean pitch angle α_0 of the radiating electrons and their drift velocity along the magnetic field v_d as

$$\cos(\theta) = \frac{v_d}{c}\cos(\alpha_0) \tag{3.2}$$

[4] The last closed field lines are those that cross the magnetic equator just inside the Alfvén radius.

[5] ECM emission is beamed in hollow cones centred on magnetic field lines. The *beaming angle* is the half-angle of such an emission cone.

[Melrose & Dulk 1993]. As $v_d/c \ll 1$, Equation 3.2 implies that the beaming angle is approximately given by

$$\theta \sim \frac{\pi}{2} - \frac{v_d}{c}\cos(\alpha_0) \sim \frac{\pi}{2}.$$

Given an electron distribution with a pitch angle distribution concentrated at α_0, the ECM flux decreases sharply with the angular deviation from the beaming angle [Hewitt, Melrose & Ruennmark 1981]. In the following simulations, I allow maximum deviations from a beaming angle of $\pi/2$ of $\sim 1°$, after the value derived for the Jovian decametric emission (DAM) [Dulk 1967]. All ECM mechanisms proposed for CU Vir, including those involving loss-cone [Trigilio et al. 2000] or horseshoe [Bingham, Cairns & Kellett 2001] electron pitch-angle distributions, are beamed perpendicularly to the field lines. This is the case for most ECM mechanisms [Treumann 2006]. See Figure 3.10 for an illustration of the magnetosphere geometry.

Most ECM mechanisms predict maximum growth rates in the extraordinary magneto-ionic mode (the X-mode) occuring near the fundamental cyclotron frequency $\nu_B = \frac{q_e B}{2\pi m_e}$ [Melrose & Dulk 1982; Melrose, Dulk & Hewitt 1984; Melrose 1994]. When both modes propagate perpendicularly to magnetic field lines, the O-mode remains linearly polarised while the X-mode becomes elliptically or circularly polarised. For the loss-cone driven ECM, growth is effective provided that the plasma frequency $\nu_P \sim 9\sqrt{N}$ Hz is less than $0.3\nu_B$ (N is the electron number density in m^{-3}). These plasma conditions are thought to hold for CU Vir [Trigilio et al. 2008], which shall be confirmed in Chapter 4. Emission at the fundamental frequency must pass through a layer where its frequency is equal to the second harmonic of the cyclotron frequency. This layer is optically thick, due to cyclotron absorption at the second harmonic, as shown in an application to the solar corona [Melrose & Dulk 1982]. The plasma density needs to be very low for the optical depth to be small enough to allow fundamental frequency radiation to escape through this layer. If this condition is not satisfied, then one needs to appeal to weaker ECM growth at the second harmonic, as assumed by Trigilio et al. (2008). However, spacecraft measurements for the Jovian decametric emission [Melrose & Dulk 1982; Melrose 1994] and the Auroral Kilometric Radiation (AKR) in the Earth's magnetosphere [Melrose 1976] indicate that emission at the fundamental frequency does escape in specific cases. In these cases, the plasma density is extremely low, with essentially no cold plasma, allowing other forms of ECM to operate [Bingham, Cairns & Kellett 2001; Kellett et al. 2007; Begelman, Ergun & Rees 2005]. These alternatives require extremely low plasma densities, which I consider implausible in a stellar atmosphere. Growth at the fundamental frequency caused by a loss-cone driven ECM in a moderately low density plasma therefore seems the most likely possibility for CU Vir.

ECM emission from a loss-cone distribution of electrons was first analysed by Hewitt, Melrose & Ronnmark (1982). A loss cone distribution $f(p_\perp, p_\parallel)$ in

perpendicular ($p_\perp$) and parallel ($p_\parallel$) momentum (with respect to the field lines) space can be expressed in terms of the total momentum p and the average electron temperature T as:

$$f(p_\perp, p_\parallel) \propto (p_\perp)^j e^{p^2/(k_B T)^2} \tag{3.3}$$

where $j > 0$ is the loss-cone index. Equation 3.3 essentially describes a distribution with no electrons with zero perpendicular momentum, but with increasing numbers at higher values of $p_\perp$. This represents a population inversion, and is the source of the free energy for the maser emission.

The emission frequency ν_B is proportional to the magnetic field strength. Higher frequency emission must always originate closer to the star (in regions of higher field strength) compared to the lower frequency emission. 20 cm emission requires a magnetic field strength of 0.0500 T and 13 cm emission requires a field strength of 0.0857 T. In the simple approximation of the dipole field strength B reducing with radius r as $B = B_p(\frac{R}{r})^3$ (with the stellar radius R and the polar magnetic field B_p), a field strength at the poles of $B_p \sim 0.3$ T gives emission heights of $\sim 1.8R$ for the 20 cm pulses and $\sim 1.5R$ for the 13 cm pulses.

I numerically simulated the CU Vir pulse phases in both bands using the assumptions above. In all simulations, the rotation period of CU Vir was split into 100 phases, and the emission was calculated at each phase to produce lightcurves. The zero phase was taken to occur when the magnetic South pole points towards the Earth, which represents the (negative) minimum of the magnetic field lightcurve. The maximum of the magnetic field lightcurve occurs at phase 50, when the North magnetic pole points towards the Earth. The effective magnetic field lightcurve was numerically derived by adding the line-of-sight magnetic field components across the face of the star for each rotation phase. I considered a 30×30 square grid with side lengths of the CU Vir diameter perpendicular to the line of sight. The line-of-sight dipole magnetic field components were summed out to 15 stellar radii along the line of sight for each grid point on the CU Vir face. The summation interval was $R/100$. The choice of 15 stellar radii reflects the estimate of the Alfvén radius of CU Vir by Leto et al. (2006). This curve is shown in the bottom panel of Figure 3.11.

The pulse lightcurves were simulated using ECM emission from the North magnetic pole, in the assumption that, as previous authors have remarked [Kellett et al. 2007; Trigilio et al. 2008], the emission originates from a single pole. The emission was taken to be perpendicular to the field lines from points where the field strength corresponded to emission at the fundamental frequency. 49 different values of the initial field line latitude λ, between $99\pi/200$ and $50\pi/200$, were considered. These represented different Alfvén radii. The field line latitudes λ are related to the radii L where the field lines cross the magnetic equator as

$$R = L\cos^2(\lambda) \tag{3.4}$$

where R is the stellar radius. Hence, the choice of $\lambda > 45^\circ$ means that field lines

with $L > 2R$ were sampled. The assumption that the field lines along which ECM emission occurs are those just beyond the last closed field lines implies that Alfvén radii greater than $2R$ were considered. For each λ, 100 field lines evenly spaced in azimuth about the magnetic pole were simulated. At the points along these field lines where the field strengths corresponded to fundamental frequency emission, 100 emission unit vectors perpendicular to the local magnetic field direction, evenly spaced in azimuth about the field lines, were identified. For a particular rotation phase and choice of λ, the angles δ between each of these emission vectors and the line of sight were calculated. Following Dulk (1967), only vectors with angular deviations from $\pi/2$ of $< 1^\circ$ were included in the flux estimates. These unit vectors were scaled by $(1^\circ - |90^\circ - \delta|)^2$ and summed for each rotation phase to prodece flux estimates. The star was assumed to be opaque, but no other propagation effects, such as absorption and refraction, were considered. The magnetic field calculations and the transformation between the magnetic field frame and the line of sight frame follow the methods given in the Appendices of Trigilio et al. (2004). Lightcurves (shown in Figure 3.11) were produced for each choice of λ for each of the two observing bands.

Our model is clearly successful in two respects. First, the rotation phases of the pulses in Figure 3.11 are approximately 20% from the zero phase. Given the symmetry of the situation about phase 0.5, this implies a $\sim 40\%$ separation between these pulses and the ones at phase 0.8 during the previous rotation phase. This corresponds to the observed pulse separations. Second, the correspondence between the pulse phases and the null line-of-sight magnetic field phases (shown in the bottom panel of Figure 3.11) matches the correspondence derived from the observations of Trigilio et al (2000). The pulses observed by Trigilio et al. (2000) matched the rotation phases of the magnetic field nulls observed by Borra & Landstreet (1980).

However, the observed difference in phase between the 13 cm pulses and the 20 cm pulses of ~ 0.03 is not similarly clear from the simulations. In fact, for the lightcurves constructed using higher latitude field lines ($\lambda > 70^\circ$), the pulse peaks, widths and positions are the same for both observing bands. However, for the lower latitude field lines, the 13 cm pulses broaden more towards the lower rotation phases (corresponding to smaller pulse separations), and the peaks are shifted by $\sim$0.01 towards the magnetic minimum. However, this is still less than the observed shift of 0.03. Hence, while the present model reproduces the general trend of the pulse separations in the different observing bands, the extent is not reproduced. Moreover, this model implies that the 13 cm pulse separation reduces more for lower latitude field lines.

Leto et al. (2006) estimated that the Alfvén radius of CU Vir lies between 12 and 17 stellar radii, which corresponds to a range of $73^\circ < \lambda < 76^\circ$. Therefore, the fact that the observed pulse separation difference between the observing bands is only reproduced for latitudes lower than $\sim 70^\circ$ implies that the model is not

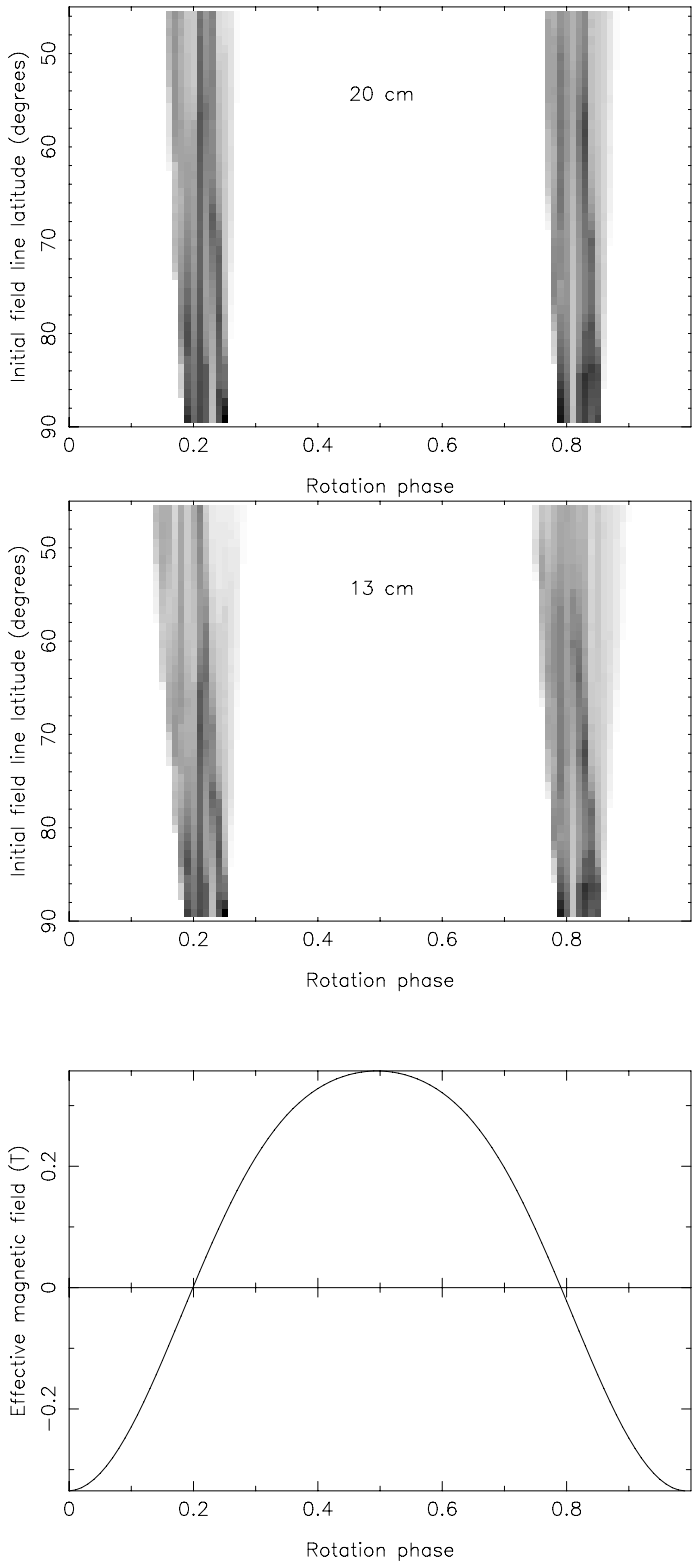

Fig. 3.11: Magnetosphere geometry simulations for CU Vir. *Top and middle:* representations of the simulated CU Vir lightcurves at 20 cm (top) and 13 cm (middle) for different values of the initial field line latitudes λ. The flux scale is in arbitrary units; greater flux is represented by darker pixels. *Bottom:* simulated effective line of sight magnetic field lightcurve of CU Vir. The rotation phase axes of the three images correspond exactly.

Star	20 cm flux (mJy)	Period (days)
HD37017	1.5−2.4	0.90
HD37479	1.5−3.2	1.19
HD142301	1.81±0.19	1.46
HD145501C	1.57±0.18	1.72
HD215441	1.07±0.09	9.49

Tab. 3.7: The sample of 20 cm MCP detections by Linsky, Drake & Bastian (1992), along with fluxes and rotation periods.

complete. I note in this context that the model also predicts two pulses from a non-thermal electron flow onto the South magnetic pole. These are offset from the North pole pulses and are not observed.

The above discrepancies may be resolved when more realistic models that allow for non-dipolar field geometries and propagation effects are constructed. There is indeed evidence from Doppler spectroscopic imaging of the CU Vir photosphere that the magnetic field is in fact not centred [Hatzes 1997]. For assumed offset dipole field geometries, the field could be displaced by as much as 0.3 stellar radii [Glagolevskij & Gerth 2002].

The choice of the North magnetic pole as the source of the emission appears to be accurate, as shown by our reproduction of the correspondence observed between the magnetic field lightcurve nulls and the pulse phases by Trigilio et al. (2000). However, the rotation glitch in 1984 [Pyper et al. 1998], between the magnetic field measurements of Borra & Landstreet (1980) and the pulse measurements of Trigilio et al. (2000), places this result in some doubt. The rotational anomaly we have identified exacerbates the situation. Simultaneous optical and radio measurements are necessary to accurately determine the phase relationship between the radio pulses and the magnetic field lightcurve.

Further, understanding the short-timescale and high-resolution spectral properties of the pulses is essential to pinning-down the emission mechanism. Such observations would reveal any variations in the electron population causing the emission, instability in the magnetosphere, and the narrow-band properties of the emission.

3.5 The incidence of CU Vir-type radio transients

It has required targeted observations to identify the pulsed emission from CU Vir. Typical continuum surveys are not searched for short-timescale transient emission. Also, standard time-domain surveys, such as pulsar surveys, are only sensitive to pulses with periodicities of less than ∼10 s.

Star	S_{6cm} (mJy)	Ref.	Rotation velocity (km.s^{-1})	B_p (kG)	Distance (pc)
HD37808 (1)	0.97	1	30	-	164
HD142301	3.78	1	69	2.10	140
HD142990	1.99	1	103	1.39	150
HD145501C	2.06	1	59	1.39	-
HD164429 (2)	0.30	1	194	-	143
HD171247 (3)	3.04	1	50	-	485
HD174637	3.55	1	-	225	
HD36485	0.95	2	30	3.4	250
HD37017	2.00	2	170	1.66	373
HD37479	3.20	2	160	2.04	-
HD34452	0.48	2	53	0.43	137
HD215441	0.95	2	5	1.69	714
HD35298	0.28	3	55	3.23	543
HD143699	0.21	3	151	1.70	162
HD144334	0.42	3	28	0.78	149
HD144844	0.19	3	-	0.32	131
HD146001	0.32	3	163	6.5	142
HD175362	0.38	3	28	3.92	130
HD124224=CU Vir	2.80	1	195	0.30	80

Tab. 3.8: A list of the MCP stars detected by Ref. 1 (Leone, Trigilio & Umana 1994), Ref. 2 (Drake et al. 1987) and Ref. 3 (Linsky, Drake & Bastian 1992) at 6 cm with flux S_{6cm}. 1) Rotation velocity from Leone, Catalano & Manfre (1993). 2) Rotation velocity from Catalano, Megazzu & Strazzulla (1979). 3) Rotation velocity from Leone & Manfre (1996).

Future telescopes such as the Australian Square Kilometre Array Pathfinder (ASKAP) [Johnston et al. 2008] will carry out deep all-sky continuum surveys whilst being sensitive to transient emission.

Here, I determine the maximum number of CU Vir-type radio transient sources detectable in upcoming surveys. Only a small fraction of MCP stars have been detected at radio frequencies, and even fewer at 20 cm [Linsky, Drake & Bastian 1992]. This analysis is based on the assumption that all the sources detected at 20 cm in the Linsky, Drake & Bastian (1992) radio survey of MCP stars are either transients, or quiescent emitters with the capability of emitting pulses[6]. This assumption is justified by the correlation identified in Section 3.3.3 between the CU Vir pulse and quiescent fluxes over different epochs. This assumption allows an initial estimate to be made of the number of CU Vir-type transient sources that future surveys will be able to detect. As more sources are detected more detailed population analyses will become possible.

Two detection methods are discussed: large-area continuum survey imaging and transient surveys that 'piggyback' on these experiments. Interferometric imaging can be used to detect transients such as CU Vir using the instantaneous synthesised beams that correspond to the pulses. Figures 3.1 and 3.2 provide examples of this method with the instantaneous ATCA fan beams. Piggyback transient surveys directly search the visibility amplitudes collected in continuum surveys for transient flux increases, much like the lightcurves presented in Figures 3.3 and 3.8. In the following, I consider two examples of such upcoming surveys with the ASKAP interferometric array [Johnston et al. 2008]:

- The Evolutionary Map of the Universe (EMU) survey [Norris & the EMU team 2009]: a survey that aims for a 10 μJy rms sensitivity over the entire sky visible to ASKAP (3/4 of the sky) at 20 cm. This survey will spend a total of 12 hours on every pointing in its field. I assume that these integrations are essentially continuous.

- The ASKAP Variables and Slow Transients (VAST) survey [personal communication from S. Johnston]: a survey that will process all continuum survey data in real time to attain a 1σ sensitivity of $\sim$0.3 mJy in 100 second integrations. The survey will cover 3/4 of the sky every 24 hours.

An interesting application of EMU-style survey data is in searching for transient or pulsed emission on different timescales. An optimal pulse detection is one where the observation lasts only for the pulse duration. Longer or shorter integrations respectively add extra noise to the radio images or reduce the sensitivities. A key advantage of large-area radio continuum imaging surveys over VAST-style

[6] No lightcurves were constructed for these 20 cm detections, and a full Stokes analysis was not carried out.

transient surveys is in being optimally sensitive to transients slower than the transient survey integration times. However, imaging surveys are impaired by their limited time-sampling of the sky. In the calculations below, I assume that radio image noise is Gaussian and is proportional to the square root of the integration time. Note that I do not consider confusion limits.

First, consider the duty cycles and periods of CU Vir-type transient pulses. The CU Vir pulses are 'on' for approximately 1 hour in 12.5 hours. I assume that this duty cycle applies to all such transients. The CU Vir rotation velocity of $195\,\mathrm{km\,s^{-1}}$ is abnormally high, as evidenced both by Table 3.7 and the fact that most MCP stars have rotation velocities between 0 and $200\,\mathrm{km\,s^{-1}}$ [Shore & Brown 1990]. It is unclear whether this is evidence for a selection effect in the detection of pulses from MCP stars, or whether the fast rotation is necessary for the pulse emission mechanism. I take the median of the rotation periods of the 20 cm sample of Table 3.7 − 1.46 days for HD142301 − as the typical period for CU Vir-type transients. The twin pulses for CU Vir lead to the argument that CU Vir in fact pulses twice every rotation period, and that this could apply to all CU Vir-type transients. However, the CU Vir emission has been characterised using the twin pulses, and similar transients will only be characterised by probing the full lightcurves. Hence, I take the median 'pulse duration' as 2.8 hours (the duty cycle multiplied by the median rotation period).

I now consider the MCP star population. There are 57 MCP stars within 100 pc of the Sun [Power et al. 2008]. I assume that these are uniformly distributed in space out to 785 pc (see below for explanation). Next, from unbiased radio surveys of MCP stars by Drake et al. (1987), Willson, Lang & Foster (1988), Linsky, Drake & Bastian (1992) and Leone, Trigilio & Umana (1994), where 94 MCP stars were observed, I derive a population fraction of MCP stars with 20 cm radio fluxes. Recall that I assume that all stars with 20 cm radio emission in such surveys are taken to be capable of emitting transients beamed towards the Earth. Table 3.7 presents the sample of all radio detections at 6 cm of MCP stars in the aforementioned surveys. All MCP stars detected at other radio frequencies also had 6 cm emission. Therefore, the sample of MCP star detections at 6 cm is $f_1 = \frac{19}{94}$. Further, out of 16 detections at 6 cm, Linsky, Drake & Bastian (1992) discovered 5 MCP stars with 20 cm emission (a fraction of $f_2 = \frac{5}{16}$): this sample is listed in Table 3.8. Therefore, I estimate the fraction of MCP stars with detectable 20 cm transient emission as $f_1 f_2 = \frac{95}{1504}$.

The 12 mJy pulses from CU Vir, at a distance of 80 pc, have a 20 cm monochromatic luminosity of $7.3\times10^{8}\,\mathrm{W\,Hz^{-1}}$. I make the assumption that the CU Vir pulse luminosity is common to all other MCP radio transients. Also, I assume that the off-pulse sensitivity is extremely good compared to any on-pulse measurements by VAST or EMU. This means that, when making the differential measurement between on-pulse and off-pulse data from a CU Vir-type transient, the pulse flux error is approximately the sensitivity of the on-pulse observation. Under these

assumptions, the VAST survey will detect a 6σ pulse of 1.8 mJy at a distance of 200 pc. For EMU, the best on-pulse sensitivity is obtained by an observation of the duration of the pulse, which we take to be the median CU Vir-type transient pulse duration of 2.8 hours. Then, applying the square root of time dependence of the sensitivity, a 6σ detection for EMU is 125 μJy. Therefore, the EMU survey will detect CU Vir-type pulses to a distance of 785 pc.

From the results of Power et al. (2008) for the MCP stellar population density, and the CU Vir-type transient population fraction $f_1 f_2$ derived above, the EMU survey will sample a maximum of ∼1750 CU Vir-type transients, and the VAST survey will sample at most 25 such transients. This accounts for the limited sky coverage. These numbers correspond to 1 star per 25 square degrees and 1 star per 1400 square degrees respectively.

The EMU survey spends 0.5 days on each pointing. However, the available time to sample the *full* 2.8 hour pulse duration is only 0.38 days. This gives a probability $P_1 = 0.38/1.46$ for any CU Vir-type transient in the field of view to pulse during a pointing. As the entire sky visible to ASKAP will be covered with these pointings, and because EMU is sensitive to pulses from a maximum of 1750 CU Vir-type transients, EMU can expect to see a maximum of $1750P_1 \sim 450$ CU Vir-type pulses. This corresponds to ∼300 detections per year, over the 1.5 year timespan.

The VAST survey scans the entire sky visible to ASKAP every 24 hours with 100 second integrations. During each pointing, the probability that a CU Vir-type transient in the ASKAP field of view will pulse is simply the duty cycle $P_d = 1/12.5$, assuming that the sampling is much less than the pulse length. Therefore, VAST could expect to see pulses from at most $25P_d = 2$ CU Vir-type transients every day, giving a total of 730 per year.

3.6 Conclusions

I have shown that

- The typical CU Vir pulse profile at both 13 cm and 20 cm consists of a pair of pulses. Unpolarised quiescent emission is also detected in both observing bands.

- The rotational ephemeris of Pyper et al. (1998) does not fit the pulse arrival time data.

- An ECM emission model assuming perpendicular beaming at the fundamental frequency partly fits the data.

- The upcoming EMU 10 μJy imaging survey with ASKAP can be expected to detect a maximum of 300 CU Vir-type transients per year, and the VAST

slow transient survey with ASKAP will detect at most 730 such transients every year.

Monitoring of future pulses is necessary in order to characterise the period discrepancy, as are simultaneous radio and optical observations. High time and frequency resolution observations of the pulses would also help probe the emission mechanism, in the hope that the population of CU Vir-type radio transient sources can be further constrained.

Modelling the CU Virginis Magnetosphere

Abstract

The quiescent modulated radio lightcurves of CU Virginis are used to fit a magnetospohere gyrosynchrotron emission model. This model is an improvement over previous models for MCP stars in that I directly model the radiatively driven wind, the current sheet geometry and the non-thermal electron spectral decay. By fitting the 6 cm lightcurve, I find a confined plasma temperature of 10^8 *K, an initial plasma density of* 10^{-17} *kg m*$^{-3}$*, a current sheet length of 0.5R, an electron acceleration rate in the current sheet of* $100\,s^{-1}\,m^{-2}$ *and a negative power law electron distribution spectral index of* $\delta = 2$*. This set of parameters models the 6 and 3 cm quiescent lightcurves of CU Vir to an accuracy of better than 15%. The model is used to confirm the possibility of ECM emission at the fundamental frequency along the non-thermal electron return field lines. Finally, previous hypotheses for the CU Vir rotation glitches involving a violent emptying of the inner magnetosphere are found to be impractical under my model.*

4.1 Introduction

The quiescent radio lightcurves of a number of MCP stars exhibit variability on the order of 50% of the peak fluxes [Leone 1991; Leone & Umana 1993; Lim, Drake & Linsky 1996]. In all known cases, the variability is periodic on the periods of the magnetic lightcurves, which implies that the emission arises from a stable, confined, co-rotating magnetosphere. This variability is seen in the case of CU Vir [Trigilio et al. 2000] at 6 cm, 3 cm and 2 cm, though the variability amplitude decreases with shortening observing wavelength. Despite our detection of quiescent emission at 20 and 13 cm, no variability is observed in these bands, besides the pulses. The characteristics of the modulated lightcurves of CU Vir are given in Table 4.1. At 6 cm, circular polarisation fractions of up to 10% are observed at rotation phases coinciding with the lower frequency pulses; though this has been interpreted as being caused by a residual of the coherent emission mechanism as opposed to the mechanism that produces the quiescence [Leto et al. 2006]. The CU Vir modulated quiescent lightcurves are characterised by two peaks and two nulls (see Figure 4.1).

Trigilio et al. (2004) described a general model for the modulated radio lightcurves of MCP stars. This model was applied to CU Vir by Leto et al. (2006). The quiescent emission is modelled as gyrosynchrotron emission from accelerated

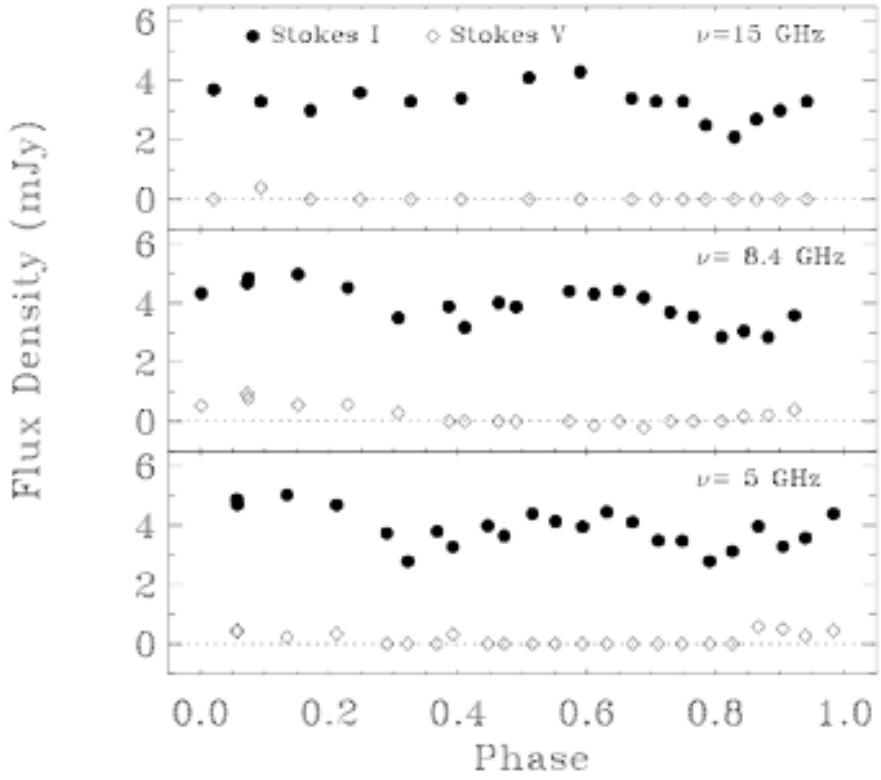

Fig. 4.1: Stokes I and V lightcurves of CU Vir at 6 cm (5 GHz), 3 cm (8.4 GHz) and 2 cm (15 GHz) from Trigilio et al. (2000).

non-thermal electrons in an anisotropic radiatively-driven wind that interacts with the magnetic field. The stellar winds of MCP stars are thought to be anisotropic in that they contain two components: strong jet-like flows from the polar regions and confined corotating areas near the equators [Shore 1987]. The presence of such jets and dense circumstellar matter is thought to explain the UV spectra of MCP stars [Shore & Brown 1990]. The winds are thought to be radiation pressure and line-driven because of the high effective surface temperatures (> 10000 K) [Groote & Hunger 1997]. Electron acceleration is thought to occur in magnetic reconnection events in current sheets on the magnetic equator formed just beyond the Alfvén radius.

The Trigilio et al. (2004) model was applied to CU Vir by Leto et al. (2006). Following the scenario proposed by Havnes & Goertz (1984) and Usov & Melrose (1992) for the magnetospheres of early-type OB and MCP stars, two zones are identified by Leto et al. (2006) in the magnetosphere of CU Vir: a *dead zone* and a *wind zone*:

- *Dead zone*: a region of confined, thermal plasma ($\sim 10^7 - 10^8$ K, from Leto et al. 2006) close to the star, where the magnetic energy density is greater than the wind kinetic energy density. This zone ends at the Alfvén radius, which was fitted by Leto et al. (2006) to range between 12 and 17 stellar radii.

Observing band	Peak flux (mJy)	Minimum flux (mJy)	Difference (mJy)
6 cm	5.0	2.7	2.3
3 cm	5.0	2.5	2.5
2 cm	4.1	1.9	2.2

Tab. 4.1: Quiescent lightcurve characteristics of CU Vir from Leto et al. (2006). All flux errors are 0.2 mJy.

The plasma is corotating with the star, resulting in the dipole structure of the field being maintained.

- *Wind zone:* Beyond the Alfvén radius, the net radial plasma flow dominates the magnetosphere structure. This region of radial outflow dragging the field lines out radially is the wind zone. As the plasma is no longer corotating here, the field lines twist azimuthally due to the rotation of the star. I stress that until the Alfvén radius is reached, the magnetosphere resembles the dead zone.

The field lines just beyond the largest closed field line form oppositely directed radial fields along the magnetic equator beyond the Alfvén radius in the wind zone. These oppositely directed fields necessitate an azimuthal planar current to separate them: this is the current sheet. Current sheet density fluctuations are believed to cause magnetic reconnection events, where the field lines reform their original dipolar structure, releasing large amounts of energy by accelerating particles of the plasma. Acceleration of particles due to magnetic reconnection in current sheets is a stable source of non-thermal electrons [Petschek 1964]. Indeed, much of the radio emission from solar flares is emitted by electrons accelerated in reconnection events [Dulk 1985]. The accelerated electrons are modelled with power law energy distributions. It is these electrons that are believed to cause the quiescent radio emission from CU Vir through a non-thermal gyrosynchrotron mechanism, as they flow back along the field lines towards the magnetic poles.

It is clear that the quiescent radio lightcurves of CU Vir are closely linked to the magnetosphere structure and composition. Leto et al. (2006) fitted the following free parameters to the lightcurves: the initial plasma density and temperature in the dead zone, the size of the dead zone (ie. the Alfvén radius), the non-thermal accelerated electron density and spectral index and the dimensions of the current sheet.

Here, I aim to improve upon the MCP star magnetosphere and gyrosynchrotron emission model of Trigilio et al. (2004), applied to CU Vir by Leto et al. (2006), in the following ways:

- The location of the Alfvén radius is crucial to the geometry of the magnetosphere, and as such I calculate its position by numerically integrating the stellar wind momentum equations. Trigilio et al. (2004) simply apply a ra-

dial wind velocity function derived for the non-magnetic case. As opposed to assuming radial wind flow in the dead zone, I assume flow along the field lines, as befits the magnetic confinement.

- The propagation effects in the confined plasma in the dead zone are highly important, because this is the only optically thick region surrounding the star. I therefore decided to derive a dead zone density profile. The thermal plasma was assumed to be isothermal. I did not include the cold dense opaque torus near the surface applied by Trigilio et al. (2004) as that area was in any case opaque in our model.

- Furthermore, in order to accurately model the effects of spectral decay for the non-thermal electrons, I resolved to integrate magneto-hydrodynamic (MHD) equations of motion for the free-streaming zone outside the Alfvén radius, including the influence of stellar rotation. This was done in two planes on either side of the current sheet, where non-thermal electrons, accelerated in the current sheet, could propagate.

- The decay of the non-thermal spectrum was also estimated, assuming a tenuous medium and no diffusion (after Hasegawa & Sato 1989), and taking into account magnetic mirroring. The pitch-angle and energy distributions were parametrised to enable these calculations.

I apply this model to the 6 cm radio lightcurve of CU Vir measured by Trigilio et al. (2000) to fit the free parameters, and check its predictions against the 3 cm lightcurve. The model is not applied to the higher frequency emission, described in Trigilio et al. (2000) and Leone et al. (2004) because, following the work of Leto et al. (2006), the higher frequency emission originates primarily from regions closer to the stellar surface where the magnetosphere plasma characteristics are not well modelled. The improvements I make here do not erase this limitation. Also, I do not test the model with the lower frequency quiescent emission, described in Chapter 3, because the variability of the 20 and 13 cm lightcurves is not constrained.

The aim of this study is threefold. First, I compare the fitted parameters to those of Leto et al. (2006). This is done in order to identify the differences caused by the more evolved physics applied here, especially in terms of the Alfvén radius not being a free parameter. Second, and most importantly, I examine the zones within our model where one could expect the coherent pulsed emission to originate, as identified in the previous chapter, to probe the local plasma and propagation conditions. The link described in Section 3.3.3 between the pulse and quiescent emission fluxes is interpreted here as implying that the quiescent gyrosynchrotron and pulse coherent ECM mechanisms originate in the same stream of non-thermal electrons from the current sheets. Finally, I attempt to model the anomaly discovered between the radio pulse and optical lightcurve periods (discussed in Section

3.3.4) in terms of a sudden emptying of the inner magnetosphere. In this model, sudden mass loss from the dead zone could cause the rotation period to reduce abruptly. I estimate what fraction of the plasma mass contained within a fitted dead zone would need to be released to cause the observed period discrepancy.

4.2 Description of the new model

In this model, the dead zone consists of a corotating, isothermal plasma, confined by the kinetic energy density being less than the dipole magnetic field energy density. The dead zone is filled by a radiatively driven wind, as justified by the high effective surface temperature and ultraviolet spectroscopic observations [Shore & Brown 1990]. The wind zone lies beyond the Alfvén radius, and the plasma essentially free-streams outwards, dragging the field lines along with the wind. The magnetosphere in the wind zone is quite similar to the original magnetic rotator scenario proposed by Parker (1967). I define a spherical polar coordinate system with the zero theta axis aligned with the magnetic axis. I assume no polar (theta) components to the field and the flow in the wind zone, but take radial and azimuthal components into account. The current sheet is believed to form in the wind zone to separate the magnetic hemispheres. Non-thermal electron backflow is modelled as occuring in two planes on either side of the sheet until the Alfvén radius, from which point onwards they follow the dipole field lines towards the poles. The layout of the model is shown in Figure 3.2.

Two key assumptions are made. First, the dipole field is assumed to be centred at the centre of the star. Second, I essentially assume an aligned rotator, except in that the angular rotation velocity Ω is taken as the component along the magnetic axis.

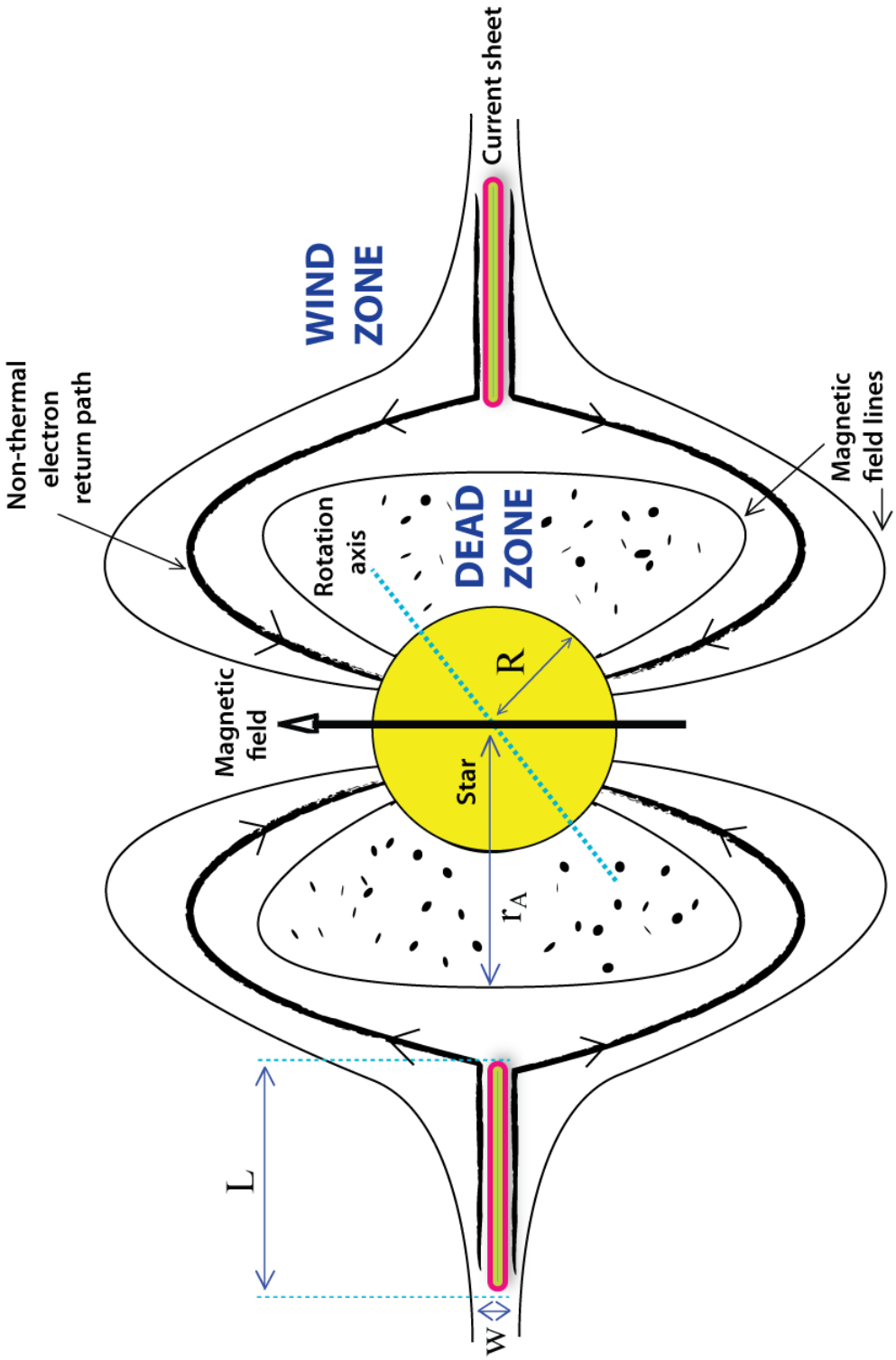

Fig. 4.2: Schematic layout of the model magnetosphere of CU Vir. The dimensions L, w, r_A and R are described in the text.

4.2.1 The dead zone

I assume that the confined plasma is in thermal equilibrium with the innermost parts of the stellar wind. Calculations by Babel & Montmerle (1997) for the plasma flow in the dead zones of Ap stars indicate that most of the plasma approximately maintains the same temperature. A caveat is these calculations, when applied to the confined zone of the A0p star IQ Aur, is that they also predicted the formation of a shock at the magnetic equator, caused by wind outflow along magnetic field lines from both hemispheres. This shock is not accounted for in my model, as its extent is not significant with respect to the dead zone size. The assumption of an isothermal plasma allows the plasma density $\rho(r)$ to be written in terms of an initial electron density ρ_0. The effective potential $\Phi(r)$ at different points in the magnetosphere along field lines can be described through Boltzmann statistics (after Michel & Sturrock 1974) as

$$\rho(r) = \frac{m_H}{m_e}\rho_0 e^{(\Phi(r)-\Phi(R))m_H/2k_BT} \tag{4.1}$$

where $\Phi(R)$ is the surface potential, and T is the plasma temperature. Note that the wind is considered as predominantly consisting of a hydrogen plasma.

The effective potential is integrated from the surface along magnetic field lines, as the magnetic force on the plasma is always perpendicular to the field. The gravitational, centrifugal, and radiative effective potentials are taken into account as

$$\Phi(r) = \frac{GM(1-\Gamma_e)}{r} + \frac{(\omega r cos(\lambda))^2}{2} + \phi_L \tag{4.2}$$

where $\Gamma_e = \frac{\sigma_T L_*}{4\pi cGMm_H}$ is an estimate of the scattering-based continuum radiation pressure fraction (σ_T is the Thomson electron cross-section and L_* is the stellar luminosity), $\lambda = \pi/2 - \theta$, ϕ_L is the effective line-driven potential, and M is the mass of the star. I follow the rationale of Babel & Montmerle (1997) in deriving the radiative acceleration components along field lines. The line-driven potential at a distance s' along a field line from the surface is given by

$$\phi_L = \int_{surface}^{s'} g_L cos(\chi) ds \tag{4.3}$$

where g_L is the line-driven acceleration, and χ is the angle between the field line of interest and the radial vector. The radiative acceleration is described in Lamers & Casinelli (1999): in the present case,

$$g_L = \frac{\sigma_e^{ref} L_*}{4\pi cr^2} k t^{-\alpha} \tag{4.4}$$

where the third force multiplier δ is neglected. Here, $t = \sigma_e^{ref}\sqrt{\frac{2k_BT_{eff}}{m_H}}\rho\frac{dr}{dv}$ is a dimensionless optical depth parameter based on the Sobolev approximation. Also,

$\sigma_e^{ref} = 0.325\,\mathrm{cm^2\,g^{-1}}$ is a reference value chosen by Lamers & Casinelli (1999) for the electron scattering opacity, $T_{eff} \sim 10000\,\mathrm{K}$ is the effective surface temperature of CU Vir [Leto et al. 2006], and, for this value, $k = 0.866$ and $\alpha = 0.454$ are the force multiplier constants of the radiatively driven wind. Initially, I approximate $v_r = \frac{\dot{M}}{4\pi R_*^2 \rho_0}.\frac{m_e}{m_H}$ and get $\frac{dr}{dv}$ from the radial velocity solution to the equation of motion in the point source approximation $v(r) = v_\infty\sqrt{1 - \frac{R_*}{r}}$ with $v_\infty = v_{esc}\sqrt{\frac{\alpha}{1-\alpha}}$ (v_{esc} is the gravitational escape velocity for CU Vir). Note that this radial velocity function was applied to the entire stellar wind of CU Vir by Leto et al. (2006). For the calculation, the solution for the velocity of the plasma along the field lines is iterated by repeatedly solving for

$$v = \sqrt{v_{init}^2 + 2g_L cos(\chi)\Delta s}$$

over length intervals Δs along field lines. Here, v_{init} is the wind velocity at the start of the interval and v is the velocity at the end of the interval.

The Alfven radius r_A is determined by equating the kinetic energy density of the wind and the magnetic energy density. Given that we assume a frozen-in dipole field within the dead zone, the magnetic energy density is simply $B^2/2\mu_0$. The kinetic energy density is taken as $\frac{1}{2}\rho(v^2 + (r\omega)^2)$.

4.2.2 The wind zone

As seems the norm for this chapter, I make a number of assumptions about the wind zone magnetosphere. First, the plasma flow, and hence the magnetic field, are considered as only possessing radial and azimuthal components (after Usov & Melrose (1992)). In keeping with the isothermal assumption, I express the pressure p in the wind as $p \sim \rho(r)a^2$, where a simple radial density profile $\rho(r) = \rho_A(\frac{r_A}{r})^3$, with the A subscripts indicating the Alfvén point, is used. The isothermal sound speed is given by $a = \sqrt{\frac{RT}{\mu}}$ from the perfect gas law, where R is Rydberg's constant, T is the plasma temperature and μ is the molecular weight of the plasma species, taken to be hydrogen in our case. I also apply the initial conditions at the Alfvén point for the radial magnetic field B_r and velocity V_r and the azimuthal magnetic field B_ϕ and velocity V_ϕ:

$$V_r = v_{r_A}$$

where v_{r_A} is the plasma radial velocity within the Alfvén surface, and

$$B_r = B_{dipole},\ V_\phi = r_A\Omega,\ B_\phi \ll 1$$

Here, B_{dipole} is the dipole field strength at the Alfvén radius on the magnetic equator. The equations of motion are derived from the equatorial wind theory of Weber & Davis (1967). From the equation of motion

$$\rho(\mathbf{v}\cdot\nabla)\mathbf{v} + \nabla(\rho a^2) + \rho\frac{GM}{r^2}\hat{\mathbf{r}} - \mathbf{J}\times\mathbf{B} = 0 \tag{4.5}$$

where **J** is the current vector, I neglect θ-components to derive, in the above assumptions,

$$\frac{\partial B_\phi}{\partial r} = \frac{1}{r}(-\frac{\mu_0 r}{B_\phi}(\frac{\dot{M}V_r}{4\pi r^3} - \frac{3\rho_A r_A^3 a^2}{r^4} + \frac{CGM}{r^2}\rho_A(\frac{r_A}{r})^3) - B_\phi) \quad (4.6)$$

$$\frac{\partial V_\phi}{\partial r} = -\frac{B_r}{B_\phi \rho V_r}(\frac{\dot{M}V_r}{4\pi r^3} - \frac{3\rho_A r_A^3 a^2}{r^4} + \frac{CGM}{r^2}\rho_A(\frac{r_A}{r})^3) \quad (4.7)$$

where $C = 1 - \Gamma_e$. Further, from mass loss, the radial velocity can be estimated as

$$V_r = \frac{\dot{M}}{4\pi r^2 \rho} \quad (4.8)$$

and by applying the frozen-in field approximation $\mathbf{E} = \frac{1}{\mu_0}\mathbf{v} \times \mathbf{B}$ (this occurs in almost fully ionised plasmas, where the conductivity is near infinite), we have

$$B_r = \frac{B_\phi V_r}{V_\phi - r\Omega} \quad (4.9)$$

Equations 4.6, 4.7, 4.8 and 4.9 were numerically solved in two radial planes on either side of the current sheet. All non-thermal electron capture and backflow was assumed to occur here.

4.2.3 Decay of the electron spectrum

Non-thermal electrons with a simple power law spectrum, with an energy distribution $N(E) = N_e E^{-\delta}$ (where δ is the negative power law index, E is the electron energy and N_e is constant), are injected at points on either side of the current sheet. These electrons are propagated back along the field lines towards the Alfvén surface, and then along the dipole field to the poles. During this propagation, the electrons are potentially subject to a number of decay processes, outlined in Longair (1994). Those of relevance are:

- Ionisation losses:
  $-(\frac{dE}{dt}) = 7.64 \times 10^{-15} N(3ln\gamma + 19.8)\ eV.s^{-1}$.
- Bremsstrahlung:
  $-(\frac{dE}{dt}) = 3.66 \times 10^{-22} NE\ eV.s^{-1}$.
- Synchrotron radiation:
  $-(\frac{dE}{dt}) = 6.6 \times 10^4 \gamma^2 B^2\ eV.s^{-1}$.
- Inverse Compton scattering:
  $-(\frac{dE}{dt}) = 1.32 \times 10^5 \mu_0 \gamma^2 U_{rad}\ eV.s^{-1}$.

Here, γ is the Lorentz factor, N is the electron density, and U_{rad} is the radiation energy density. If we consider the decay timescale of an electron of energy E,

such an electron will lose all its energy in a time $\tau = \frac{E}{dE/dt}$. A comparison of decay timescales for the processes listed above for conditions in the model shows that only those proportional to E^2, that is, synchrotron and inverse Compton processes, are significant. Ignoring diffusion effects caused by the strengthening magnetic field in the direction of propagation (after Hasegawa & Sato 1989), the diffusion-loss equation for high energy electrons with an energy distribution $N(E)$ becomes

$$\frac{dN}{dt} = Q(E) + \frac{\partial}{\partial E}(-\frac{dE}{dt}N(E)) \tag{4.10}$$

which with an injection spectrum $Q(E) = N_e E^{-\delta}$ reduces to $N(E) = N_e E^{-\delta}(1 - bEt)^{\delta-2}$, where

$$b = \frac{6.6 \times 10^4}{m^2 c^4}(B^2 + 2\mu_0 U_{rad}),\ t = \frac{d}{v\cos(\theta)}$$

and θ is the electron pitch angle. Essentially, electrons with an energy $E_s \geq 1/at$ cease to be non-thermal after a time t.

Magnetic mirroring also plays an important role in the evolution of the pitch angle distribution. In short, electrons travelling into regions of greater magnetic field strength will be reflected if their pitch angles are too large. The trapping condition is

$$\frac{\mid v_\parallel \mid}{\mid v_\perp \mid} < \sqrt{\frac{B_{max}}{B_{min}} - 1} \tag{4.11}$$

Electrons with smaller velocities $v_\parallel$ along the magnetic field lines, and larger velocities $v_\perp$ perpendicular to the field lines are more likely to be reflected when travelling from a smaller magnetic field B_{min} to a larger magnetic field B_{max}.

4.2.4 Model evaluation

The aim of the model is to fit a non-thermal gyrosynchrotron lightcurve to the quiescent emission from CU Vir at 6 cm, and to test this fit by reproducing the 3 cm lightcurve. These lightcurves were observed by Trigilio et al. (2000). The emission and absorption coefficients were derived from expressions by Klein (1987) appropriate for the low harmonic numbers of interest. Furthermore, these expressions leave the energy distributions and the pitch-angle distributions independent. Only emission and absorption within the dead zone was taken into account because the wind zone consisted mostly of a tenuous plasma. Thermal gyrosynchrotron absorption was also calculated, using expressions from Dulk & Marsh (1982), as well as thermal free-free absorption and Razin-Tsytovich suppression [Dulk 1985]. The emission from each non-thermal electron sample point within the dead zone was integrated towards the Earth along the line of sight. Please refer to the Appendix at the end of this chapter for a description of the radiation calculations.

The free parameters of the model were:

- Thermal plasma temperature T: After some investigation, trial values of $T = 10^8,\ 5 \times 10^8$ & $10^9\ K$ were used. This was in order to achieve a

reasonable estimate for the Alfvén radius ($> 3R_*$) without an unreasonable initial electron density.

- Initial plasma electron density ρ_0: This was essentially the electron density of the plasma at the base of the wind. Trial values included 10^{-18}, 10^{-17} & 10^{-16} kg.m^{-3}, which were again chosen to allow a reasonable Alfvén radius as well as a non-prohibitive thermal absorption within the dead zone.

- Electron acceleration rate per square metre in the current sheet E_{rate}: The trial values used were 10, 100, 1000 & 10000 electrons per second. The fit was most sensitive to this parameter.

- Current sheet radial (L) and thickness (w) dimensions (see Figure 4.2 for their illustration): These defined not so much the current sheet itself as the size of the acceleration volume surrounding the star. Values trialled included $L = r_A/2,\ r_A,\ 2r_A$ and $w = R/10,\ R/5,\ 3R/10$.

- Non-thermal electron injection spectral index δ: Values of 2 and 3 were trialled.

The characteristics of the 6 and 3 cm lightcurves that were compared with the model output were the peak Stokes I flux and the ratio between the peak and the minimum fluxes. These are listed in Table 4.1. The polar magnetic field strength used was $B_p = 0.3\ T$. All fits were carried out over half a symmetric lightcurve in 30 rotation intervals. The zero phase of the lightcurve was chosen as before in Chapter 3, at the minimum of the magnetic field lightcurve. I note here that this does *not* represent the choice of zero phase in Figure 4.1 by Trigilio et al. (2000), as that choice was not published.

The sampling of the model was designed for efficient computation without errors due to sampling discreteness becoming prohibitive. Azimuthal symmetry was assumed about the magnetic axis, and 50 discrete azimuthal values were considered. The flow in the dead zone was evaluated along 50 field lines evenly spaced in initial angles with the equator, in each hemisphere. The flow was iterated along 50 evenly spaced points from the base of each field line to the equator, unless the Alfvén radius was exceeded. The Alfvén radius was identified as the radius of the last dead zone point on the first open field line from the equator. The density was then evaluated in 80 steps along this field line through the corner of the current sheet, along which the backflow of non-thermal electrons was assumed to occur. The wind zone fields were radially evaluated in 50 steps to the parametrised outer radius of the current sheet on either side of it. The initial power law electron spectrum was computed in 19 separate energy bins starting from an initial value of 10 keV defined as $E_i = 1.6 \times 10^{-15}(\sqrt{10})^i$ J running over $i = 0, 1, ...18$. The isotropic pitch-angle spectrum was separated into 49 evenly spaced bins over $\frac{\pi}{100}$

to $\frac{49\pi}{100}$ to take into account magnetic mirroring. The non-thermal electron propagation in the wind zone was computed by injecting an area-scaled number of electrons at each of the 50 radial by 50 azimuthal points below and above the current sheet, and propagating these along the twisted magnetic field lines inwards to the Alfvén surface. This method forms a naturally steady-state solution, as no variability in the acceleration is assumed. From the Alfvén surface, the electrons were propagated along the dipole field lines determined earlier towards the poles in 80 steps of equal length, and radiation from them calculated at each step.

4.3 Fit to the 6 cm CU Vir lightcurve

First, it was noticed that the model was in effect independent of the trial values for the thickness w of the current sheet, and that an electron spectral index of $\delta = 3$ produced no flux for any combination of the other parameters. Therefore, I was unable to fit for the current sheet thickness, and also concluded that $\delta = 2$. The subsequent fit of the magnetosphere model to the 6 cm quiescent lightcurve of CU Vir was narrowed down in three steps:

- Any flux value produced by a set of free parameters for any rotation phase greater than 100 mJy or less than 0.01 mJy was immediately discarded.
- All sets of free parameters that produced peak fluxes S_{max} and minimum fluxes S_{min} such that S_{min}/S_{max} was within 20% of the value of 0.54 for the 6 cm lightcurve (see Table 4.1) were retained. This produced a surprisingly tightly clustered group of parameter sets, listed in Table 4.2.
- The values of S_{min} and S_{max} in Table 4.2 closest to those observed, given in Table 4.1, were identified, and the corresponding parameter set chosen as the fit.

The fitted parameter set (highlighted in Table 4.2 in bold font), apart from the current sheet thickness, is: $T = 10^8$ K, $\rho_0 = 10^{-17}\,\mathrm{kg\,m^{-3}}$, $L = 0.5R$, $E_{rate} = 100\,\mathrm{s^{-1}\,m^{-2}}$ and $\delta = 2$. The fitted 6 cm lightcurve is shown in Figure 4.3. A 3 cm lightcurve was also constructed using the best-fit parameters; this is shown in Figure 4.4. Please refer to Figure 4.1 for a qualitative comparison with the actual lightcurves measured by Trigilio et al. (2000). Quantitatively, I model the fluxes of the 6 and 3 cm lightcurves to within 15%, and hence model the spectral index in these bands to the same accuracy. The error was estimated by manually calculating the average difference between each point in the Figure 4.1 lightcurves and the nearest point in the corresponding Figure 4.3 or 4.4 lightcurve. Note that the lightcurves were appropriately aligned such that the peaks and troughs of the modulation appeared at the same phases.

The fitted parameters are hard to compare to those derived by Leto et al. (2006) for the CU Vir magnetosphere, given the different physics applied in the

T (K)	ρ_0 (kg m^{-3})	E_{rate} (s^{-1} m^{-2})	L (R)	S_{min} (mJy)	S_{max} (mJy)	S_{min}/S_{max}
10^8	10^{-17}	1	0.5	0.031541	0.057960	0.544193
10^8	10^{-17}	1	1	0.063082	0.116620	0.540922
10^8	10^{-17}	1	2	0.126165	0.233141	0.541153
10^8	10^{-17}	10	0.5	0.315412	0.585811	0.538419
10^8	10^{-17}	10	1	0.630824	1.157673	0.544907
10^8	10^{-17}	10	2	1.261649	2.267245	0.556468
10^8	**10^{-17}**	**100**	**0.5**	**3.154121**	**5.658326**	**0.557430**
10^8	10^{-17}	100	1	6.308243	11.397295	0.553486
10^8	10^{-17}	100	2	12.616486	22.935091	0.550095
10^9	10^{-17}	1	0.5	0.147988	0.286829	0.515944
10^9	10^{-17}	1	2	0.592014	1.147315	0.515999
10^9	10^{-17}	10	0.5	1.480874	2.868289	0.516292
10^9	10^{-17}	10	10	2.966706	5.736577	0.517156
10^9	10^{-17}	100	0.5	14.903714	28.682886	0.519603
10^9	10^{-16}	1	0.5	0.289037	0.513920	0.562417
10^9	10^{-16}	10	2	11.561487	20.697012	0.558607

Tab. 4.2: Selected fit results for the 6 cm lightcurve of CU Vir (see text for explanation.)

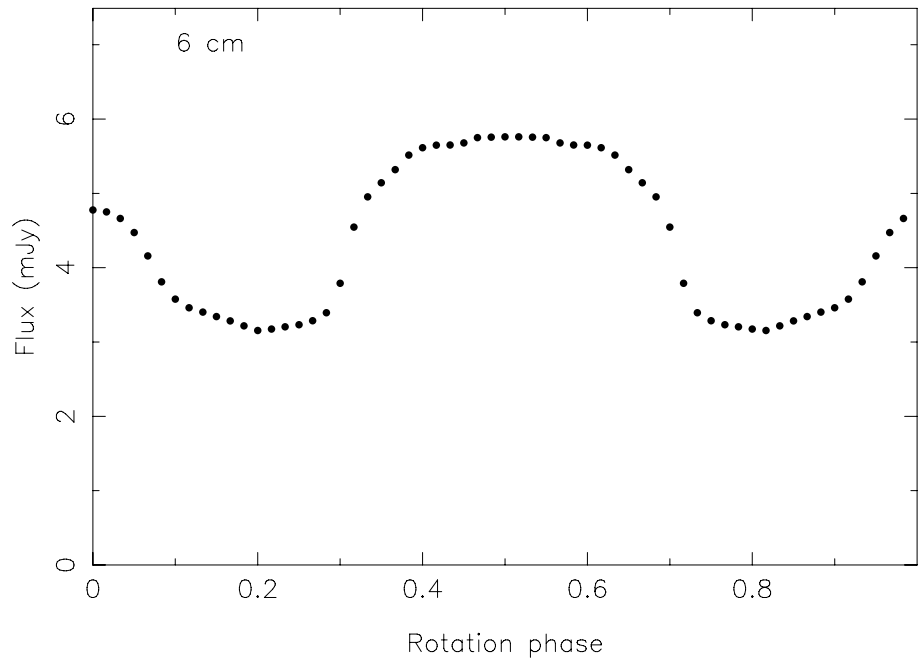

Fig. 4.3: Best-fit 6 cm lightcurve of CU Vir with the magnetosphere model presented here. Compare to the actual lightcurve measured by Trigilio et al. (2000) in Figure 4.1.

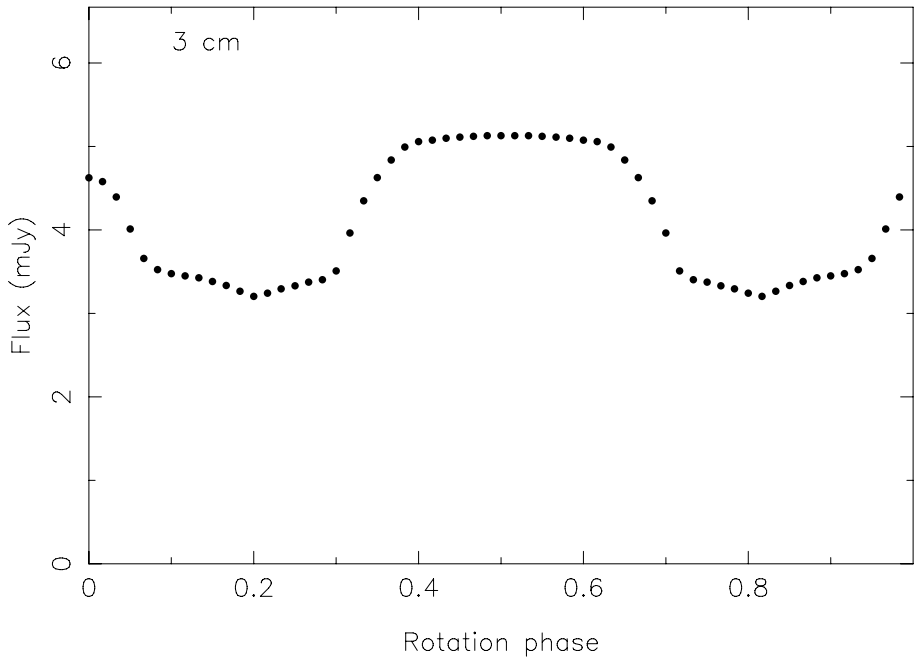

Fig. 4.4: 3 cm lightcurve of CU Vir constructed with the best-fit parameters of the magnetosphere model presented here. Compare to the actual lightcurve measured by Trigilio et al. (2000) in Figure 4.1.

two models, the different free parameters, and the fewer parameters left free here in the fitting process. Both models result in electron spectral indices of $\delta = 2$. One cannot compare the non-thermal electron density of $\sim 10^9\,\mathrm{m}^{-3}$ derived by Leto et al. (2006) with the value of E_{rate}, which is the rate of acceleration of non-thermal electrons per unit area on the current sheet. The models also differ in their wind zone geometries: Leto et al. (2006) model the non-thermal electrons as flowing directly upwards from the current sheet towards the poles without entering the dead zone, whereas I model the electrons as flowing along the current sheet (see Figure 4.2). This difference exists because Leto et al. (2006) do not actually calculate geometry of the edge of the dead zone, whereas this is done in the model presented here. Furthermore, Leto et al. (2006) assumes a constant plasma density as well as temperature throughout the dead zone, meaning that the initial values for ρ_0 at the base of the stellar wind cannot be compared with this value. Figure 4.5 shows the radial thermal plasma density profile along the field lines carrying non-thermal electrons to the poles in the new model. However, the dead zone plasma temperature of $T = 10^8\,\mathrm{K}$ matches the range derived by Leto et al. (2006) of $10^7 - 10^8\,\mathrm{K}$.

A significant difference is in the Alfvén radii derived in the different models. The new model places the Alfvén radius at ~ 6.06 stellar radii, whereas this value is anywhere between 12 and 17 stellar radii in the Leto et al. (2006) model. The discrepancy can be explained through the fact that the Alfvén radius is not free in the new model, but is derived using the physics of a radiatively driven wind in

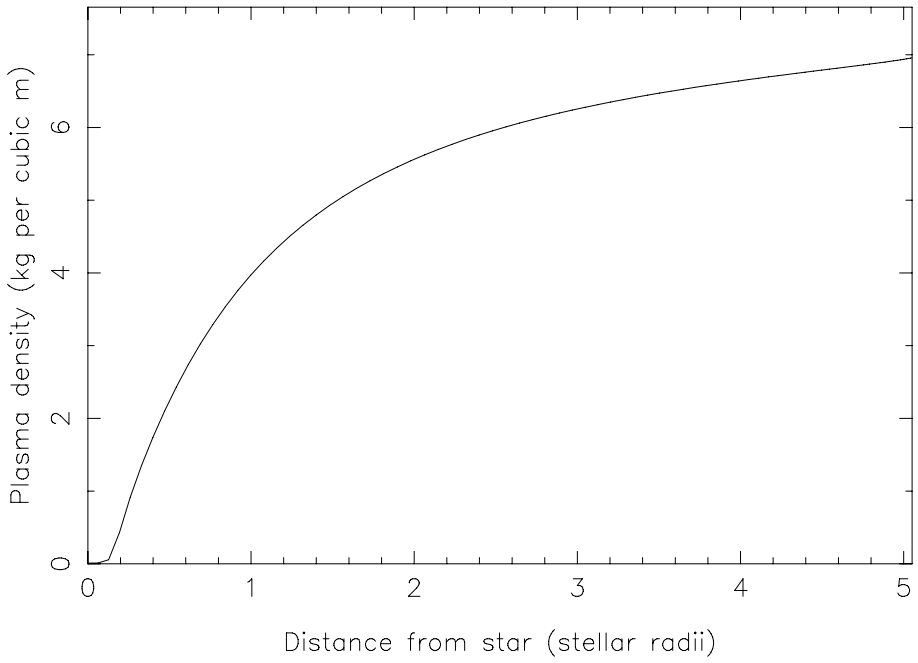

Fig. 4.5: Radial thermal plasma density profile along the non-thermmal electron return field lines. The density is expressed in $10^{15} \times \mathrm{kg\,m^{-3}}$.

a confined corotating plasma. The wind model applied by Leto et al. (2006) to estimate the Alfvén radius was a simple result derived for a non-magnetic plasma. Therefore, I suggest that the estimate of Leto et al. (2006) for the Alfvén radius is wrong, as it is based on less complete physics than that applied here. The stellar diameter of CU Vir at 80 pc subtends an angle of $\sim 2 \times 10^{-6}$ milli-arcseconds. High-frequency VLBI experiments with intercontinental baselines might possibly resolve the confined zone by detecting the boundary of the non-thermal gyrosynchrotron radiation.

4.4 Examination of the ECM zones

We have seen in the Chapter 3 that the approximate pulse phase separations of CU Vir at 20 and 13 cm are approximately maintained regardless of the latitudes of the field lines along which coherent emission occurs (see Figure 3.8). Also, I interpret the link between the fluxes of the pulses and quiescent emission at different epochs as implying that the same stream of non-thermal electrons feeds both the quiescent gyrosynchrotron and pulse ECM emission mechanisms. Therefore, I model the ECM emission at 20 and 13 cm in the fitted CU Vir magnetosphere as originating at the points along the non-thermal electron return field lines where the cyclotron frequencies match the observing bands. This is analogous to the geometry modelled in the previous chapter for the pulse lightcurves.

Consider two properties of these points for pulsed emission in observing bands: the average local plasma frequencies and the average X-mode gyrosynchrotron

absorption coefficients along the line of sight. I calculate the average absorption coefficients including all phases where pulsed emission is visible, as derived in the previous chapter (see Figure 3.8). These include phases 0.16−0.26 and 0.74−0.87 for 20 cm emission, and phases 0.14−0.28 and 0.75−0.89 for 13 cm emission. The averaging is over all sample points along the non-thermal electron return field lines near the North magnetic pole closest to the field strengths of 0.0500 and 0.0857 T required for fundamental frequency emission at 20 and 13 cm emission. The choice of the North pole results from the modelling of the previous chapter. These points are azimuthally symmetric. The absorption coefficient includes the X-mode non-thermal component, and the thermal gyrosynchrotron component (which is the same for O-mode and X-mode propagation) [Dulk & Marsh 1982].

The sample points turned out not to be sufficiently spaced to distinguish between 20 cm and 13 cm emission. This is explained by the $1/r^3$ dependence of the dipole field strength. The resulting average plasma frequency at the ECM emission points is 1.8×10^8 Hz, and the average absorption coefficient along the line of sight is 4.7×10^{-2}. The absorption coefficients for each of the points were integrated along the lines of sight, and then averaged.

I conclude that the new model permits ECM emission being emitted at the fundamental frequency in the geometry described in the previous chapter. ECM emission at the fundamental frequency in a loss-cone mechanism, such as the one we propose for the CU Vir pulses, requires that $\nu_p < 0.3\nu_B$ [Melrose & Dulk 1982]. Here, for 20 cm emission (at $\nu = 1.4 \times 10^9$ Hz), the plasma frequency is 0.13 of the fundamental frequency. For 13 cm emission (at $\nu = 1.4 \times 10^9$ Hz), this factor becomes 0.075. Second, the small average X-mode gyrosynchrotron absorption coefficient along the line of sight during the pulse phases indicates that the magnetosphere is optically thin, at least in thermal and non-thermal gyrosynchrotron absorption, with respect to the ECM emission.

4.5 Modelling the rotational glitch in CU Vir

The rotation period of CU Vir has been shown to be unstable. Pyper et al. (1998) found that the rotation period underwent a sudden increase by 0.005% circa 1984. More recently, I show in Chapter 3 that a discrepancy between the period of the radio pulses and the latest optical rotation ephemeris of Pyper et al. (1998) could be explained as a second period increase of 0.0027%. This second period increase was first detected by Trigilio et al. (2008) only using pulse observations during June 1998, May 1999 (Epoch A) and August 1999 (Epoch B). I accurately quantify it in this thesis using observations during October 2008 (Epoch C).

A number of models have been proposed for the CU Vir glitches. For example, one model suggests an internal magnetic field-driven re-arrangement of mass in the star, causing a change in the moment of inertia while maintaining a constant angular momentum [Stępień 1998]. This has since been ruled out [Trigilio et al. 2008],

because the magnetic field is considered too weak to alter the moment of inertia of the whole star, modelled as a rigid rotator. Trigilio et al. (2008) suggested that the period changes in CU Vir could be caused by a violent emptying of the dead zone plasma in a sudden breaking of the magnetic confinement. Here, I test this model quantitatively by estimating what fraction of the angular momentum contained in the co-rotating dead zone, with the modelled plasma density radial profile, would have to be lost to produce the observed 0.0027% period discrepancy.

The angular momentum J of CU Vir is related to the moment of inertia I as

$$J = \frac{2\pi I}{P} \tag{4.12}$$

where P is the period. Then, assuming a loss of angular momentum in the glitch, the angular momentum change ΔJ is related to the period change ΔP by

$$\frac{\Delta J}{J} = -\frac{\Delta P}{P} \tag{4.13}$$

Writing the angular momentum in terms of the angular momentum J_{star} of CU Vir and the angular momentum J_{dz} of the dead zone as $J = J_{star} + J_{dz}$, the fractional modulus loss of angular momentum in the glitch with respect to J_{dz} is

$$\frac{\Delta J}{J_{dz}} = \frac{\Delta P}{P}\frac{J_{star} + J_{dz}}{J_{dz}} \tag{4.14}$$

Approximating the star as a rigid rotator, its angular momentum is given by $J_{star} = \frac{4\pi}{5P}MR^2$. I estimate the angular momentum of the dead zone by summing the angular momenta of concentric spherical shells with densities given by the radial density profile $\rho(r)$ derived along the non-thermal electron return field lines. This profile is shown in Figure 4.5. Then,

$$J_{dz} = \frac{2\pi}{P}\sum_i \frac{2}{3} r_i^2 \rho(r_i) \frac{4}{3}\pi(r_i^3 - r_{i-1}^3) \tag{4.15}$$

where the index i runs over the radial shells at radii r_i that were sampled in the model. Finally, we already have $\frac{\Delta P}{P} = 0.000027$.

The result is striking: $\frac{\Delta J}{J_{dz}} = 5.44 \times 10^7$. Clearly, the abrupt loss of all the angular momentum contained in the dead zone is insufficient to cause the observed period change, as claimed by Trigilio et al. (2008). In fact, the observed period change requires a fraction of 2.7×10^{-5} of the angular momentum J of the whole system to be lost. Therefore, I conclude that the suggestion of Trigilio et al. (2008) is wrong: a sudden emptying of the magnetosphere is not sufficient to explain the observed rotational anomalies of CU Vir, neither the one analysed here nor the one identified by Pyper et al. (1998).

A possible mechanism for the period change could be the more gradual loss of dead zone plasma from the Alfvén radius caused by instabilities in the wind

density. In this mechanism, a single sudden breaking of the magnetic confinement is not invoked; instead, mass, and angular momentum, is lost in a series of small breaks. Further work is necessary in order to estimate reasonable timescales and the rates of mass loss to explain the period changes.

4.6 Conclusions

I have shown that:

- The MCP star magnetosphere model of Trigilio et al. (2004), applied to CU Vir by Leto et al. (2006), can be improved in its physics by making the Alfvén radius a dependent variable, by accounting for the twisting of the magnetic field lines in the wind zone, and by considering the evolving and decaying energy and pitch angle distributions of the non-thermal electrons. Using the modulated 6 cm lightcurve of CU Vir, measured by Trigilio et al. (2000), I find a best fit set of parameters: $T = 10^8\,\mathrm{K}$, $\rho_0 = 10^{-17}\,\mathrm{kg\,m^{-3}}$, $L = 0.5R$, $R/10 \leq w \leq 3R/10$, $E_{rate} = 100\,\mathrm{s^{-1}\,m^{-2}}$ and $\delta = 2$. These parameters reproduce the 6 cm and 3 cm lightcurves and the spectral index of the emission in these bands to an accuracy of better than 15%.

- This new magnetosphere model permits ECM emission in the geometry derived in the previous chapter, as evidenced by the low local plasma frequencies at the ECM emission regions and the optically thin propagation paths during the derived pulse phases.

- The rotational glitches of CU Vir cannot be explained by a violent emptying of the dead zone plasma, a mechanism suggested by Trigilio et al. (2008).

Further work is necessary to refine the model to include the following:

- quiescent emission at other frequencies,

- a non-isothermal stellar wind,

- the presence of a shock where the stellar winds from the two magnetic hemispheres collide at the magnetic equator,

- an identification of the development of the electron pitch angle distribution, possibly into a loss-cone, with a view to directly modelling the ECM emission,

- a measure of the polarisation of the emission, both quiescent and pulsed.

Finally, a more careful comparison needs to be made with the original model of Trigilio et al. (2004), so that the generality of the new model can be tested.

4.7 Appendix - Radiation calculations

4.7.1 Gyrosynchrotron radiation fluxes

The evolving electron distributions in energy and pitch angle made it necessary to calculate the non-thermal gyrosynchrotron radiation fluxes using the analytical expressions presented in Klein (1987). These expressions are based on the rigourous treatment of Ramaty (1969), and offer a means to calculate the emission and absorption coefficients using electron numbers at different energies and pitch angles in both magneto-ionic modes. The analysis is optimised for small harmonic numbers and mildly relativistic distributions. Refractive indices were calculated from Ramaty (1969). Of note is the technique used to estimate the pitch angle and energy distribution gradients. With the discrete sampling $N(E_i, \theta_j)$ over indices i and j running across the energy E and pitch angle θ ranges, the pitch angle gradient was simply calculated as

$$\frac{\partial N}{\partial \theta} = \frac{N(\theta_{i+1}) - N(\theta_{i-1})}{\theta_{i+1} - \theta_{i-1}} \tag{4.16}$$

However, the essentially power-law nature of the energy spectrum led me to assume that this was so in the estimation of the gradient, giving

$$\frac{\partial N}{\partial E} = -nE^{-n-1},\ -n = \frac{ln(N(E_{i+1})) - ln(N(E_{i-1}))}{ln(E_{i+1}) - ln(E_{i-1})} \tag{4.17}$$

These expressions were appropriately modified at the ends of the spectra.

The viewing angle to the magnetic field at a point with respect to the line of sight was calculated by comparing the component of the magnetic field in the direction of the Earth with the magnetic field strength. Rotations between the magnetic field frame and the sky frame were performed using the rotation matrices given in the Appendices of Trigilio et al. (2004).

4.7.2 Radiative transfer and absorption

The gyrosynchrotron radiation from each point in the dead zone along the propagation path of the non-thermal electrons was evaluated along the line of sight, and propagated towards the Earth. The transfer was iteratively integrated in steps of $r_A/100$ until the edge of the dead zone as

$$I_i' = I_i e^{-\alpha_i \Delta s} + \frac{\eta_i}{\alpha_i}(1 - e^{-\alpha_i \Delta s}) \tag{4.18}$$

where $\Delta s = r_A/100$ is the length of the unit volume element in the line of sight into which I_i passes and from which I_i' exits. The absorption and emission coefficients are α_i and η_i respectively, and the index i refers to the i'th step. Absorption beyond the dead zone was ignored.

Non-thermal gyrosynchrotron radiation from the accelerated electrons was calculated from Klein (1987). Absorption due to non-thermal and thermal gyrosynchrotron mechanisms [Dulk & Marsh 1982] was also taken into account, as was free-free absorption, which was calculated from Dulk (1985). Razin-Tsytovich suppression of emission at frequencies where the plasma (ν_P) and cyclotron (ν_B) frequencies were related as $\nu\nu_B \leq \nu_P^2$ was included [Dulk 1985].

Clearing the Atmosphere of a Flaring Brown Dwarf

Abstract

I present the results of a search for transient and quiescent emission from the brown dwarfs DENIS 1048−3956 and LHS 3003 with the new wide-band correlator at the ATCA, at 6, 3 and 1.2 cm. While no transient emission, nor quiescent emission from LHS 3003, was detected, I detect quiescence from DENIS 1048−3956 across all bands, and derive a negative power law spectral index of -1.7 ± 0.6. *This is the first proof of a negative power law spectrum for brown dwarfs, and is interpreted as optically thin gyrosynchrotron emission from a non-thermal power law electron population with a negative spectral index of* 3.2 ± 0.6. *A circular polarisation fraction of* 0.24 ± 0.05 *from DENIS 1048−3956 is detected in the 6/3 cm band, which implies a line-of-sight magnetic field of* 0.007 ± 0.002 *T. The average non-thermal electron number density is constrained as less than* $2.7 \times 10^{14}\, m^{-3}$, *the tightest constraint yet on a radio-loud brown dwarf. Finally, I interpret the lack of emission from LHS 3003 (a previously detected quiescent emitter) as indicative of a two-state model for brown dwarf activity. The activity states vary between a radio-quiet state where the Güdel-Benz relation for radio and X-ray luminosities from cool stars dominates, and a radio loud state. LHS 3003 is interpreted as being in a radio quiet state, and I predict that more sensitive measurements would detect a flux of 4 μJy in the 6/3 cm band; DENIS 1048−3956 is thought to currently be in the radio loud state, as it violates the Güdel-Benz relation.*

5.1 Introduction

Ultracool dwarf stars [Kirkpatrick et al. 1999] are the coolest members of the stellar zoo. They are defined as those stars with spectral types of M7 or later, ranging across the spectral classes L and T. Ultracool dwarfs occupy the mass gap between the largest planets and the smallest hydrogen-burning stars, with masses usually taken to be < 0.08 solar masses [Neuhäuser et al. 1999]. Ultracool dwarfs with masses greater than ~ 0.01 solar masses are characterised by thermonuclear fusion of deuterium or lithium in their cores. This isolates the population of *brown dwarfs* [Oppenheimer, Kulkarni & Stauffer 1998], a subset of the ultracool dwarfs, from massive discrete gaseous objects or planets, which are not massive enough to support fusion of any kind. All brown dwarfs are formed by gravitational collapse in protostellar clouds, as opposed to the formation of planets in protostellar accretion

disks around young stars. Typical brown dwarf stars have radii on the order of the radius of Jupiter ($\sim 7 \times 10^6$ m) [Burrows et al. 2001], but are, of course, much more massive.

While a large fraction of early M stars (spectral classes M1−M6) exhibit high-temperature chromospheric and coronal emission from radio to X-ray wavelengths, this surface activity generally decreases sharply for ultracool dwarfs [Gizis et al. 2000]. Surface activity, particularly in the form of Hα emission, is linked to the presence of magnetic fields. Magnetic fields are integral to the dynamics of stars, playing crucial roles in the initial accretion, spin evolution and interaction processes. High brightness temperature radiation from early M stars is interpreted as originating in non-thermal surface plasma populations. Magnetic activity, much like on the surface of the Sun [Dulk 1985], is associated with the creation of these non-thermal populations. The surface activity in early M dwarfs consists of both quiescent and flaring components at all wavelengths [Güdel 2002]. While brown dwarfs display a sharp decrease in quiescent emission as compared to early M dwarfs, the flaring component is slower to decrease, with X-ray flares seen from stars as cool as spectral type M9.5 [Fleming, Giampapa & Schmitt 2000] and optical flares seen down to L5 stars [Liebert et al. 2003]. However, the general trend towards lower surface activities in ultracool dwarfs can be explained by an expected decline in magnetic activity. The cool chromospheres of ultracool dwarfs are thought to have less ionized material than those of early M dwarfs, which leads to the magnetic fields being decoupled from the surfaces.

Radio emission from ultracool dwarfs is therefore expected to be weak or non-existent. The Güdel-Benz emperical relation between radio and X-ray quiescent and flaring emission from low-mass magnetically active stars supports this conjecture [Benz & Güdel 1994]. The low X-ray fluxes from a sample of nearby brown dwarfs imply radio flux densities that are less than 1 μJy [Berger 2002]. An illustration of the Güdel-Benz relation from Güdel (2002) is shown in Figure 5.1.

However, a small number of brown dwarfs appear to violate the Güdel-Benz relation, displaying both quiescent and transient radio emission. Berger et al. (2001) discovered the M9 dwarf LP944−20 to be a persistent radio emitter, with a 6 cm quiescent radio flux that violated the Güdel-Benz predicted flux by more than four orders of magnitude. Two flares on timecales of minutes were also detected. Subsequently, Berger (2002) detected three further brown dwarfs with significantly higher quiescent radio fluxes than expected. Currently, around 13 brown dwarfs have been detected at radio wavelengths, out of a sample of $\sim$ 110 surveyed [Berger 2006]. Six of these, including LP944-20, have also been observed to flare. Unlike the flares from LP944-20, the flares from the other brown dwarfs are highly circularly polarised and in most cases periodic. The M9 dwarf TVLM 513−46546 is perhaps the protptypical example of a class of periodic stellar radio transient, with short duty-cycle 100% circularly polarised pulses observed during every $\sim$3.3 hr rotation [Hallinan et al. 2007]. However,

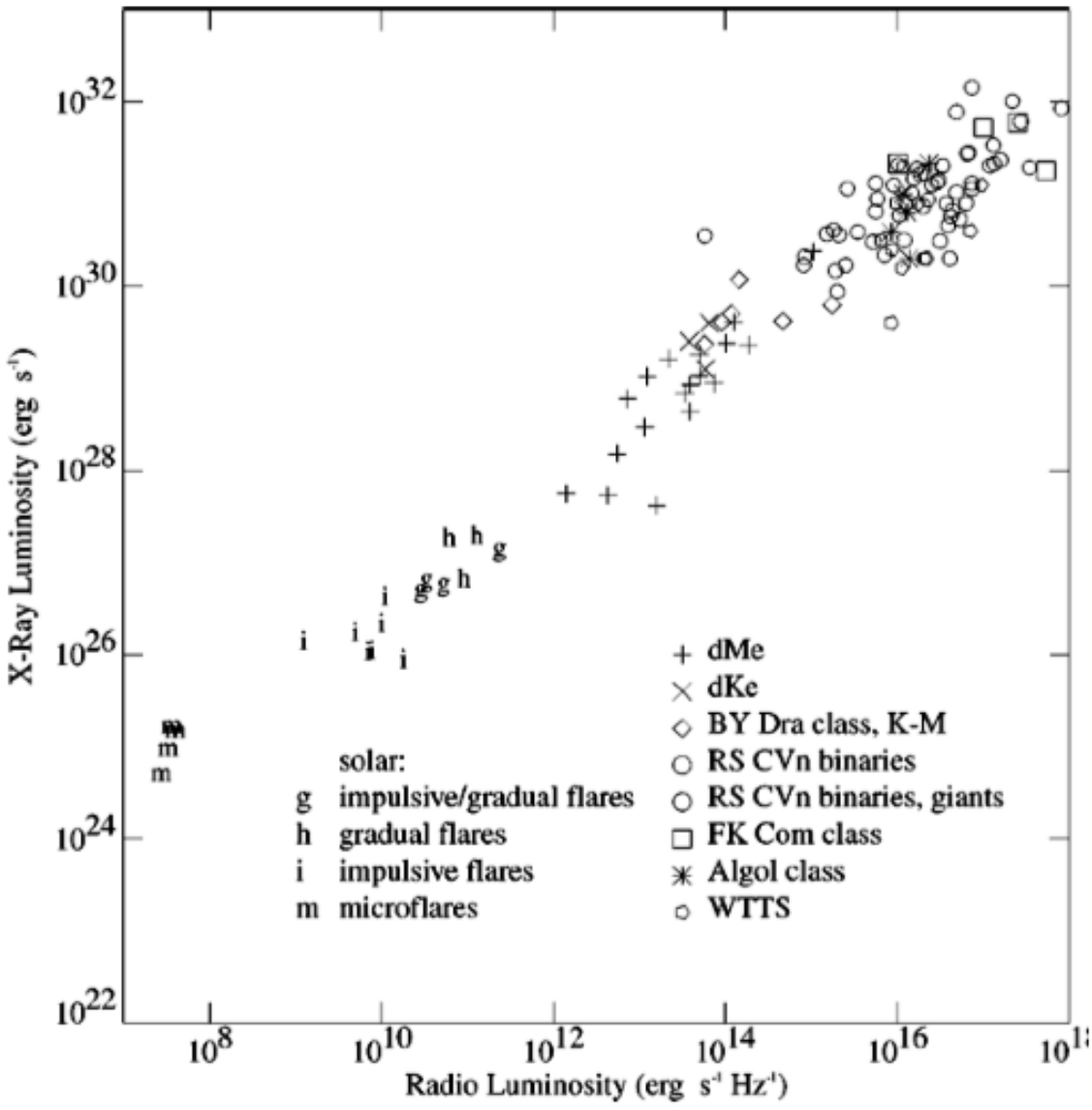

Fig. 5.1: The Güdel-Benz correlation between the X-ray and radio luminosities of samples of magnetically active stars (symbols) and flares from cool stars (letters), from Güdel (2002).

both flaring and quiescent emission from brown dwarfs is highly variable with time [Osten et al. 2009], with persistent emission and periodic flares turning on and off on timescales of months to years. Indeed, the pulses from TVLM 513−46546 were not seen when observed a year before the flaring epoch [Hallinan et al. 2007].

Burgasser & Putman (2005), in a survey for 6 and 3 cm radio emission from seven nearby M and L dwarfs with the ATCA, detected the brown dwarfs LHS 3003 (M7) and DENIS 1048−3956 (M8) as quiescent radio emitters persistent over the observing times of 12 hours. The quiescent fluxes were 0.27 and 0.14 mJy respectively at 6 cm; neither source was detected at 3 cm. Since this epoch, Osten et al. (2009) re-observed LHS 3003 and failed to detect any radio emission in the same bands. DENIS 1048−3956 was also observed to flare once in each observing band, with peak fluxes of ~ 6 mJy at 6 cm and ~ 30 mJy at 3 cm. The flares lasted for a few minutes each, and the 6 cm flare preceded the 3 cm flare by 10 minutes. Both flares were completely circularly polarised.

The large quiescent brightness temperatures of the radio emitting brown dwarfs ($> 10^7$ K) [Berger 2006] imply non-thermal emission. The recent detections of kilo-Gauss (~ 0.1 T) magnetic fields in a large fraction of brown dwarfs [Reiners & Basri 2007] have led to the radio emission being interpreted in terms of incoherent non-thermal gyrosynchrotron emission [Burgasser & Putman 2005] for the quiescence and coherent electron-cyclotron maser emission for the pulses and flares [Hallinan et al. 2008]. The origins of the non-thermal electron populations in these stars is unknown; they are however postulated to be caused by surface instabilities leading to magnetic field line reconnection events [Hallinan et al. 2008]. The lack of observational constraints on the magnetic fields of brown dwarfs (their low optical luminosities make spectrophotometric measurements of Zeeman lines extremely difficult [Reiners & Basri 2007]) means that magnetospheric models for the non-thermal radio emission similar to those for magnetic Ap stars (such as CU Vir - see Chapters 3 and 4) are not yet feasible.

Here, I utilise the unprecedented wide-band spectral characteristics of the recently implemented Compact Array Broadband Backend (CABB)[1] correlator for the ATCA to attempt to re-detect and characterise flares from DENIS 1048-3956, and to measure its radio spectrum between 6 and 1.2 cm. I did not observe a known periodic pulsator because, at the time when I submitted the observing proposal, no such source was known that is in regions of the sky visible to the ATCA. CABB provides two 2.048 GHz bandwidths for each polarisation[2] at wavelengths shorter than 13 cm. Un-allocated observing time was also used to attempt a re-detection of LHS 3003 at 6 and 3 cm. The spectral properties of the quiescent emission constrain the emission mechanisms. Further, the measurement of the spectral properties of any flares from DENIS 1048-3956, or possibly from LHS 3003, would

[1] http://www.atnf.csiro.au/technology/electronics/docs/cabb/p1629.pdf

[2] All ATCA receivers sample the sky signals in two orthogonal linear polarisations, as well as measure the cross products.

allow an indirect mapping of the magnetosphere. Electron-cyclotron maser emission is emitted at the fundamental cyclotron frequency [Melrose & Dulk 1982], and is tightly beamed perpendicularly to the magetic field. The cyclotron frequency is proportional to the magnetic field strength. Any delay of the flares at different frequencies would indicate emission from different regions in the magnetosphere.

This study is motivated partly by the ambiguity over the magnetic field structures, plasma environments and radio emission mechanisms of brown dwarfs. Furthermore, it appears that brown dwarfs could form a key part of the transient radio sky. Upcoming large-area continuum imaging and transient surveys with next generation radio telescopes will target the transient radio sky. It is therefore important to characterise transient radio emitters. Dwarf stars are believed to be the most common stars in the galaxy [Oppenheimer, Kulkarni & Stauffer 1998], and it is expected that future studies will detect a large number of brown dwarf transients.

The structure of this chapter is as follows. In §2, I outline the observing and analysis techniques used to search for flares and quiescence and measure the spectra of DENIS 1048−3956 and LHS 3003. I present the results in §3, including the redetection of quiescence from DENIS 1048−3956 and a measurement of the spectral index of the emission. I discuss the emission mechanism for DENIS 1048−3956 and derive constraints on the magnetospheric non-thermal electron density in §4. The conclusions are summarised in §5.

5.2 Observing and data analysis techniques

I observed DENIS 1048−3956 (10:48:14.64,−39:56:06.24) on 2009 August 10, 11 and 15, and LHS 3003 (14:56:38.314,−28:09:47.38) on 2009 August 13, with the ATCA in its fully extended 6D configuration. A fully extended configuration was chosen so as to minimize source confusion from extended structure (see Section 5.3.2 for a discussion of source confusion). DENIS 1048−3956 was observed with two different frequency setups: one with the two simultaneous 2.048 GHz CABB bandwidths centred at 18 and 24 GHz (1.2 cm), and another with the two 2.048 GHz bandwidths centred at 5.5 and 9 GHz (6/3 cm). LHS 3003 was observed only with the latter setup[3]. Data were recorded in 2049 channels each with a 1 MHz bandwidth across each 2.048 GHz band, with integration times of 10 s. The channels had 'square' responses, meaning that no smoothing had to be applied to the data to account for channel edge defects. The 100 channels at the edges of each 2.048 GHz CABB bandwidth were discarded from the data because of bandpass edge defects. Flux, bandpass and polarisation calibrations were obtained from the ATCA primary calibrator PKS 1934-638 for all observations. A secondary cali-

[3] When discussing the simultaneous 6 cm and 3 cm observations, or combined 6 cm and 3 cm data, I shall refer to the *6/3 cm band*. However, when discussing observations or data at 6 cm and 3 cm independently, I shall refer to the *6 and 3 cm bands*.

brator was also observed at short intervals during the observing runs for phase and gain calibrations. Pointing calibrations with known strong point sources near the targets were also undertaken every hour while observing in the 1.2 cm band. Details of the observations are presented in Table 5.1. The phase centres for all on-source observations were placed 10" South of the target positions in order to avoid the possibility of image artefacts at the ATCA pointing centres due to correlator offsets.

The target position for DENIS 1048−3956 was calculated by taking into account the high proper motion of the star ($-0.08\,\mathrm{sec\,yr^{-1}}$, $-1\,\mathrm{arcsec\,yr^{-1}}$, from SIMBAD). Burgasser & Putman (2005) detected DENIS 1048−3956 at the position (10:48:14.2, −39:56:10) during May 2002. I modified this position for the 2009 observations to (10:48:13.6, −39:56:17).

I carried out the data reduction using the MIRIAD software package. The analysis was tailored to produce three results:

- lightcurves in each observing band with the target fluxes averaged over different time bins in order to search for transient and variable emission,
- quiescent source flux detections or limits in each observing band, and
- measurements of the spectral properties of any detected emission.

First, narrow-band and short-timescale RFI was removed from the visibilities, along with any short-timescale amplitude excursions in the secondary calibrator data. The data were split into bins of 256 MHz and calibrated separately to enable conventional flux, bandpass, phase and gain calibration techniques. This negated the need to account for the variations in the calibrators due to intrinsic spectral properties across the wide CABB bands. The polarisation calibrations were always obtained from the primary calibrator data because the secondary calibrator visibilities invariably had a limited parallactic angle coverage. The datasets were then recombined, the phase centres shifted to the target positions, and then imaged out to one primary beam FWHM. Self calibration using the MIRIAD task GPSCAL was applied to the visibilities using strong (> 5 mJy) sources within the central primary beam FWHM. All sources detected to greater than 6σ beyond three synthesised beams from the target positions and within one primary beam FWHM were then modelled using the MIRIAD task CLEAN and subtracted from the visibilities.

Source	Start (UT)	T_{obs}	Cal 2	Observing band (cm)	Frequencies (GHz)	Beam size
DENIS 1048−3956	9/8/09 21:08	9.5	PKS1104−445	1.2	18, 24	0.65"×1.03"
	11/8/09 03:23	4.34	PKS1104−445	1.2	18, 24	2.09"×3.33"
	15/8/09 02:27	4.87	PKS1104−445	6/3	5.5, 9	2.09"×3.33"
LHS 3003	14/9/09 10:49	2.52	PKS1514−241	6/3	5.5, 9	2.09"×3.33"

Tab. 5.1: ATCA observing log for DENIS 1048−3956 and LHS 3003. T_{obs} is the observing time in hours, and Cal 2 is the secondary calibrator. The beam size gives the synthesised beam dimensions for the band centres, which are given in turn by the frequencies.

Source-subtracted lightcurves were then constructed for data in the 1.2 cm and 6/3 cm bands in all Stokes polarisations by calculating the real components of the vector-averaged visibilities. The averaging was conducted over time bins of different lengths to check for variability and flaring on different timescales. Next, the 6/3 cm data for LHS 3003 and DENIS 1048−3956 and the 1.2 cm data for DENIS 1048−3956 were imaged in all polarisations using the source-subtracted visibilities. The sensitivities of the images were calculated by finding the rms values of the thermal noise in the images everywhere except within three synthesised beams of the image centres. Any case of a detection within three synthesised beams of the target positions had the synthesised 'dirty' beam deconvolved using the MIRIAD tasks CLEAN and RESTOR. Finally, spectra at 6/3 cm were constructed by splitting the combined datasets into eight 512 MHz bins, imaging each bin, deconvolving the 'dirty' beam from the central target sources and measuring the source fluxes by fitting two dimensional Gaussian synthesised beam profiles with the MIRIAD task IMFIT.

5.3 Results

5.3.1 Transient emission search

Neither DENIS 1048−3956 nor LHS 3003 was detected as a source of transient radio emission. The source-subtracted lightcurves for each observation listed in Table 5.1 are shown in Figures 5.5 to 5.12 (see the Appendix at the end of this Chapter) in Stokes I and V, with time averaging bins of 10 s 1 min and 10 min. The $\pm 1 rms$ and $\pm 3 rms$ levels are shown as dashed horizontal lines, where the rms values were calculated using the modulus of all data in each lightcurve. Lightcurves in Stokes Q and U similarly showed no transient emission. Flares were taken to require a detection threshold of at least six times the rms values (after Niinuma et al. 2009). While a full statistical analysis of the significance of each measurement given the spread of the data is necessary, no clearly visible transient emission is present. The one case of a negative Stokes I peak (Figure 5.11; LHS 3003) in the 10 s time-averaged data appears to be caused by internal system temperature variations or interference, as evidenced by there only being a few points over that time that form part of the variation.

This result is in contrast to the number of brown dwarfs that in recent years have been observed to produce periodic highly circularly polarised periodic pulses of radio emission [Hallinan et al. 2007, Hallinan et al. 2008, Berger et al. 2009]. It was our goal to detect such emission from either of DENIS 1048−3956 or LHS 3003 in order to probe the properties of the pulses. The high brightness temperatures ($> 10^{12}$ K) of detected pulses and almost complete circular polarisations indicate a coherent emission mechanism, such as the electron-cyclotron maser. Such a mechanism was proposed for the flare observed from DENIS 1048−3956

Source	Band (cm)	Stokes	Peak flux	σ
DENIS 1048−3956	6/3	I	0.21	0.01
DENIS 1048−3956	6/3	V	0.05	0.009
DENIS 1048−3956	1.2	I	0.028	0.007
DENIS 1048−3956	1.2	V	–	0.0069
LHS 3003	6/3	I	–	0.020
LHS 3003	6/3	V	–	0.017

Tab. 5.2: Quiescent detections and sensitivities in mJy at 6 and 3 cm and 1.2 cm for DENIS 1048−3956 and LHS 3003.

[Burgasser & Putman 2005]. The periodicity of pulses observed from brown dwarfs and their short duty cycles are reminiscent of pulsar emission [Hewish et al. 1968]. It was this link that motivated the search for pulses, along with the opportunities that periodic pulses offer to constrain the emission physics, non-thermal electron populations, magnetosphere structures and rotational characteristics of such stars, much like what has been achieved in the case of CU Vir (see Chapters 3 and 4).

5.3.2 Quiescent detections

DENIS 1048−3956 was detected in Stokes I as a quiescent point source in the 6, 3 and 1.2 cm bands. Additionally, Stokes V emission was detected from DENIS 1048−3956 in the 6/3 cm images. No emission was detected in either Stokes Q or U. DENIS 1048−3956 was detected at the position (10:48:13.6, −39:56:16), in close agreement with the modified position accounting for the proper motion of the star. LHS 3003 was not detected as a quiescent emitter, though the most constraining radio flux limits yet applied to a non-detected brown dwarf were derived. Details of the measurements are given in Table 5.2. Figure 5.2 shows the 6/3 cm detections for DENIS 1048−3956, and Figure 5.3 shows the 1.2 cm detection.

I placed the detection thresholds at the source positions at the relatively low limit of 3σ, in contrast to the $4-5\sigma$ limits used for blind radio surveys [Richards et al. 1998]. This is justified by the targeted nature of the observations: the phase centre of the visibilities were ultimately placed at the expected source positions, and assuming purely Gaussian image noise, a 3σ detection implies that, at the expected source position, there is a 0.1% possibility of such a result being noise. This implies that the 3σ Stokes I and V flux constraints on LHS 3003 are 0.060 and 0.051 mJy respectively.

Burgasser & Putman (2005) estimate that, at 6 and 3 cm, the confusion probability for similar ATCA observations of DENIS 1048−3956 is less than 0.2%. The confusion probability is given by $P_c = 1 - e^{-N}$, where N is the number of sources within the targeted area. Their estimate of N was derived from the source counts per unit area on the sky in blind 6 and 3 cm surveys, and the flux range of their sources was chosen to match the range of sources within their fields.

Similarly, I now derive a confusion probability for the 1.2 cm observations of DENIS 1048−3956. No blind survey at 1.2 cm has been conducted to date to match the continuum sensitivities I achieve. For example, the most sensitive survey attempted in this band − the AT20G all-sky survey with the ATCA − achieved a final sensitivity of $\sigma = 300$ mJy, more than a factor of 3×10^5 greater than the sensitivities of my observations. Therefore, rather than attempting a population synthesis of weaker 1.2 cm sources based on these counts, I use the models of De Zotti et al. (2005) for extragalactic sources at 1.2 cm, including flat spectrum radio quasars and BL Lacertae objects, star-forming galaxies, extreme GHz peaked radio sources, advection-dominated accretion flows, and Sunyaev-Zeldovich effect sources on galactic and cluster scales. Fits of models of the luminosity functions of these sources to blind survey source counts yield a total differential source count at 10 μJy of 10^8 sr^{-1} $(d \log S)^{-1}$, where S is the flux in mJy. Given that all sources detected to greater than 6σ have been subtracted from the 1.2 cm Stokes I image, I integrate the differential source count between $3\sigma = 20.7\,\mu$Jy and $6\sigma = 41.4\,\mu$Jy to derive, given the 1.2 cm beam size of 0.65"×1.03", a source count $N = 1.63 \times 10^{-4}$ sources per beam. Therefore, for any detection within three synthesised beams of the source position, the confusion probability is $P_c = 1 - e^{-28N} = 0.46\%$ (the factor of 28 accounts for the ~ 28 beams within the area under consideration).

DENIS 1048−3956 was detected to $> 4\sigma$ at 1.2 cm, with a flux of 0.028±0.007 mJy. While this source was detected by Burgasser & Putman (2005) at 6 cm, the 3 and 1.2 cm detections presented here are new. I estimate the probability of the 1.2 cm detection being either noise or source confusion as $0.1 + 0.46 = 0.56\%$ (the 0.1% comes from the 4σ detection). While the 6/3 cm detection is well above 6σ, the confusion probability for this detection, from Burgasser & Putman (2005), is 0.2%. I however conclude, to a high degree of certainty, that the detected sources are in fact DENIS 1048−3956.

Furthermore, I consider the $> 5\sigma$ detection of circular polarisation from DENIS 1048−3956 as real, because of the paucity of astronomical sources of circularly polarised radiation [Fender 2003], along with the positional correspondance with the Stokes I emission. Given that I have accepted 3σ as the lower limit of detectability in Stokes I, I apply the same principle to the Stokes V detectability. Therefore, DENIS 1048−3956 is detected with a quiescent circular polarisation fraction of $r_c = 24 \pm 5\%$.

5.3.3 Applying the Güdel-Benz relation to DENIS 1048−3956 and LHS 3003

The Güdel-Benz relation [Benz & Güdel 1994] is an emperical correlation between the $5 - 8$ GHz radio monochromatic and X-ray bolometric luminosities of almost all low-mass coronally (and hence magnetically) active stars, both in flares and quiescence. The X-ray bolometric luminosities L_X and the radio monochromatic

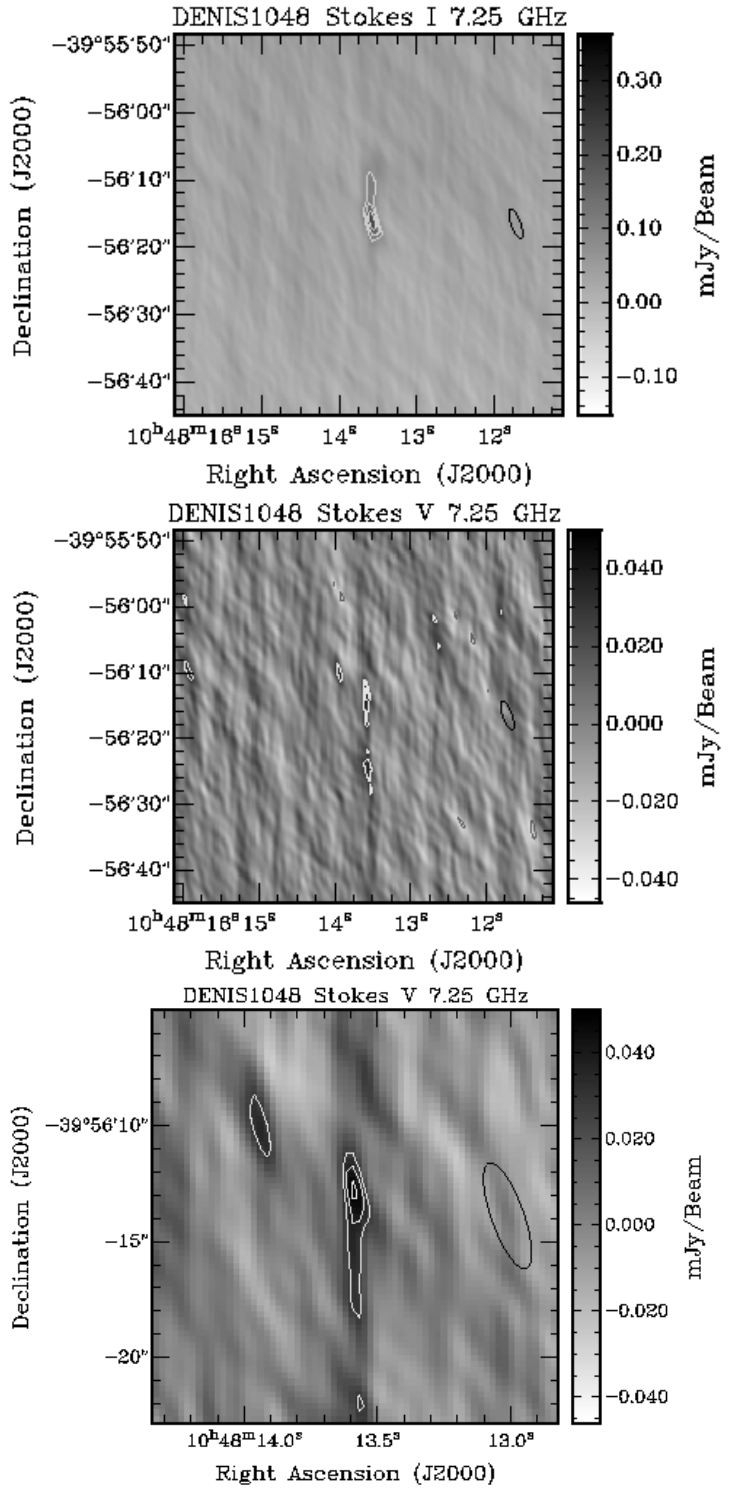

Fig. 5.2: Images of DENIS 1048−3956 at the combined 6 and 3 cm bands. From top: Stokes I ($\sigma = 10\,\mu$Jy), Stokes V ($\sigma = 9\,\mu$Jy) and a closeup of the Stokes V image centre. The Stokes I contours begin at a fourth of the peak flux of 218 μJy and increase in factors of $\sqrt{2}$. The Stokes V contours are at $\pm 3\sigma$, 4σ, 5σ and 6σ (positive contours are light, and negative contours are dark; no negative contours are present in the images). The synthesised beam shapes are shown to the right of the images, and the colour bars show the flux scales.

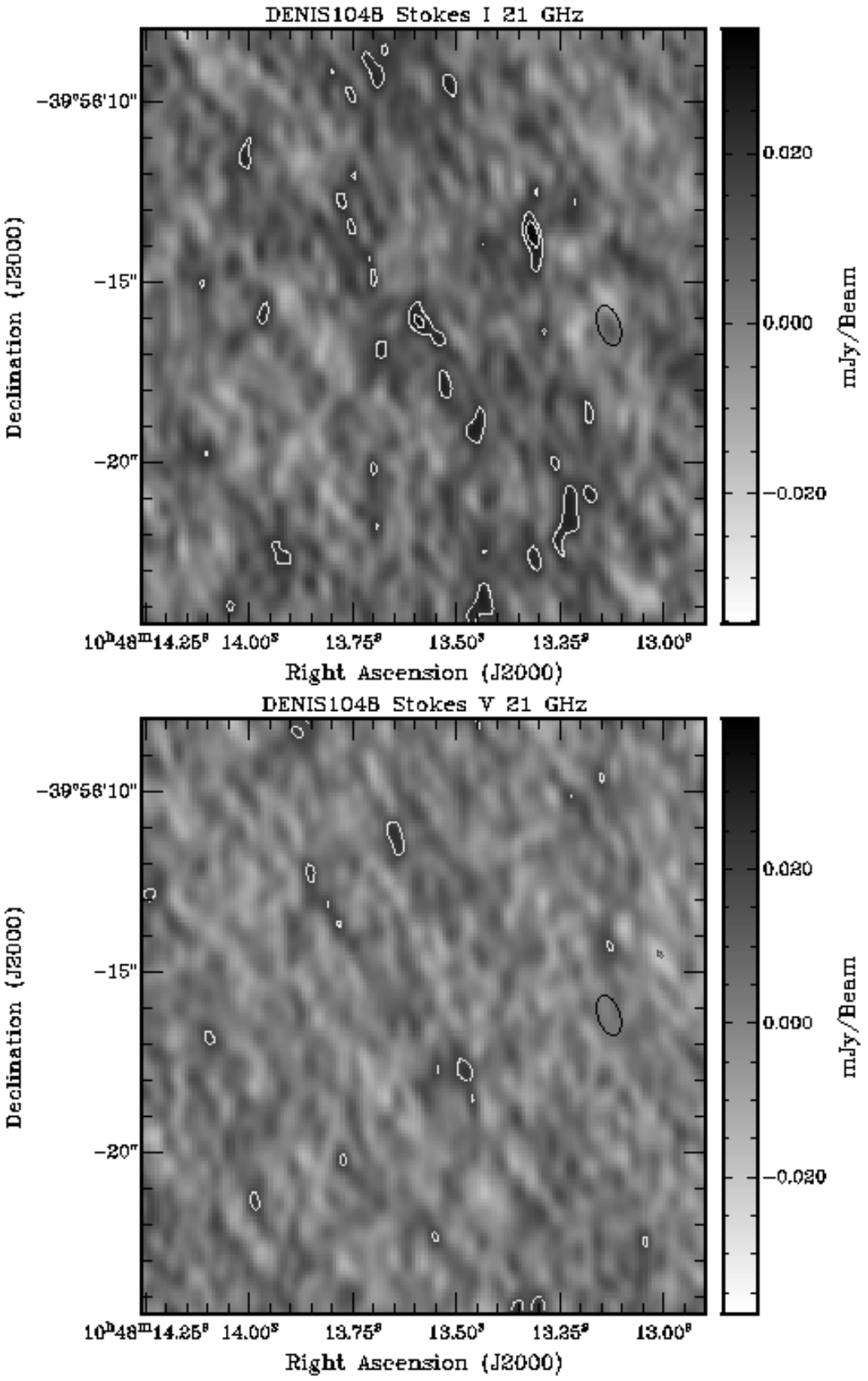

Fig. 5.3: Images of DENIS 1048−3956 at 1.2 cm. From top: Stokes I (σ = 6.8 μJy), Stokes V (σ = 6.9 μJy). Contours are at $\pm 3\sigma$, 4σ, 5σ and 6σ (positive contours are light, and negative contours are dark). The synthesised beam shapes are shown to the right of the images, and the colour bars show the flux scales.

luminosities L_R are related as

$$\frac{L_X}{L_R} \sim 10^{15} \tag{5.1}$$

It is suggested that both the radio and X-ray luminosities are tracers of magnetic activity on the surfaces of cool stars [Güdel et al. 1993]. The mechanism of plasma heating is not constrained, though various models ranging from energy release from magnetic loops to numerous small coronal flares have been suggested [Güdel 2002].

For DENIS 1048−3956, at a distance of $D = 4.3\,\mathrm{pc}$ (from SIMBAD), I calculate a monochromatic luminosity across the 6/3 cm band ($5 - 8\,\mathrm{GHz}$) as $L_R = 4\pi D^2 \times 2.1 \times 10^{-30} = 4.65 \times 10^5\,\mathrm{J\,s^{-1}\,Hz^{-1}}$. From Equation 5.1, this implies a Güdel-Benz X-ray luminosity of $L_X = 4.65 \times 10^{20}\,\mathrm{J\,s^{-1}}$. However, Burgasser & Putman (2005) limit the X-ray luminosity of DENIS 1048−3956 to $L_X < 2.00 \times 10^{19}\,\mathrm{J\,s^{-1}}$. Therefore, the Güdel-Benz relation is violated for DENIS 1048−3956. This is consistent with other brown dwarfs detected with radio emission, but is not as strong a violation as in some instances [Berger 2002].

I now use the Güdel-Benz relation to estimate the radio flux of LHS 3003. This star has a known X-ray luminosity of $L_X = 2.00 \times 10^{19}\,\mathrm{J\,s^{-1}}$ [Burgasser & Putman 2005]. Given its distance of 6.6 pc (from SIMBAD), the predicted radio luminosity of $L_R = 2.00 \times \times 10^4\,\mathrm{J\,s^{-1}\,Hz^{-1}}$ implies a radio flux of $\sim 4\,\mu$Jy in the 6 and 3 cm bands. This is a factor of 5 below the σ-value of the Stokes I radio image of LHS 3003 (see Table 5.2).

These results lead to an interesting proposition for the magnetospheric activities of brown dwarfs. I suggest that the Güdel-Benz relation always holds, even for brown dwarfs, except when dominated by an extreme epoch of electron acceleration in the coronal plasma. That is, I predict that whatever mechanism that drives the Güdel-Benz relation in magnetically active early M stars applies to magnetic brown dwarfs as well, except when dominated by an unusually active radio-loud epoch during which the radio emission dramatically increases. This two-state model seems to apply to the variability seen in the radio emission from a number of brown dwarfs [Osten et al. 2009], including, from the evidence in that paper, LHS 3003. I therefore predict that highly sensitive radio observations of LHS 3003 during its 'quiet' phase will reveal quiescent flux of $\sim 4\,\mu$Jy at 6/3 cm. Future observations are necessary to test this prediction.

5.3.4 The Stokes I spectrum of DENIS 1048−3956

The detections of Stokes I emission from DENIS 1048−3956 in the 6, 3 and 1.2 cm bands, combined with the wide bandwidths sampled by CABB, allow an analysis of the spectrum of the quiscent emission from this system. The spectrum, displayed in Figure 5.4, was constructed in 512 MHz bins as described in Section 5.2. The spectral points are listed in Table 5.3. The spectrum in Figure 5.4 is plotted on a log-log scale, with the errors scaled appropriately. The errors in the points between

Frequency (GHz)	Flux (μJy)
4.731	484±5
5.244	330±4
5.756	100±20
6.268	150±20
8.232	128±6
8.744	107±6
9.256	105±5
9.768	133±6
19.000	28±7

Tab. 5.3: Spectral measurements of DENIS 1048−3956 between 4.5 GHz and 21 GHz.

4.5 and 10 GHz (6/3 cm) are the errors of the 2-dimensional Gaussian fits to the frequency-binned source images, and the error of the 21 GHz flux measurement is the σ-value for the image[4].

I fit a power law spectrum for the flux $S(\nu)$ as a function of the frequency ν in terms of a spectral index α

$$S(\nu) = K\nu^{\alpha} \tag{5.2}$$

where K is a constant of proportionality. The fit utilised a least-squares fitting method with points weighted by the squares of the errors. The resulting curve, also shown in Figure 5.4, had a spectral index $\alpha = -1.7 \pm 0.6$.

This negative spectral index is consistent with the limits placed by the non-detection at 3 cm by Burgasser & Putman (2005) of DENIS 1048−3956, and is also consistent with tentative results for other brown dwarfs using data just at 6 cm and 3 cm [Berger et al. 2009]. However, the detection at 1.2 cm along with the highly sampled spectrum between 6 and 3 cm establishes incontrovertibly, for the first time, the power-law nature of the spectrum across a wide band. Previous estimates of brown dwarf radio spectra only utilised at most two points. The 1.2 cm detection is also the first of its kind for brown dwarfs.

[4] This is because the MIRIAD two-dimensional Gaussian fitting routine IMFIT failed to converge on a solution.

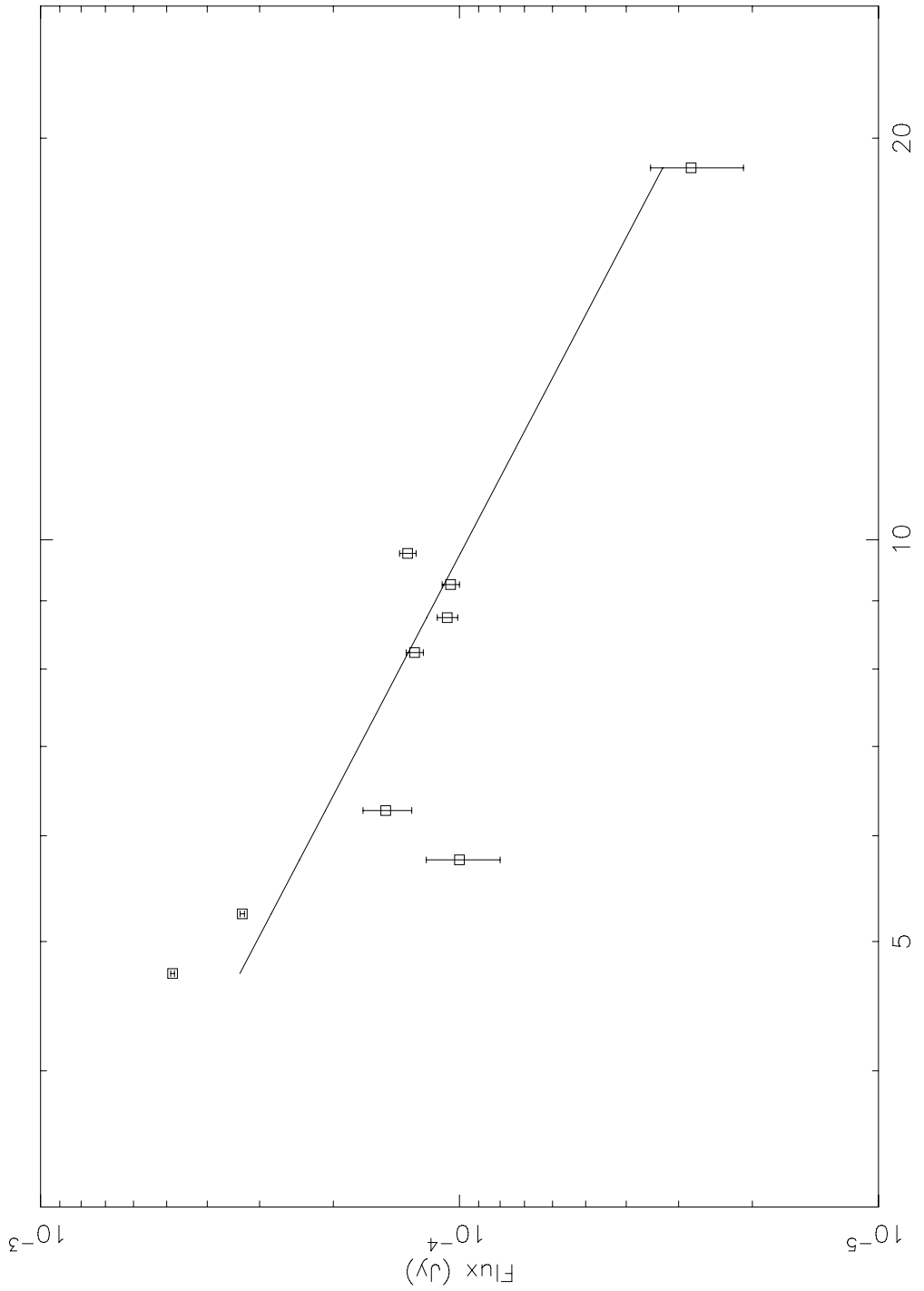

Fig. 5.4: Radio spectrum of DENIS 1048−3956. The fitted power law has an index of -1.7 ± 0.6.

5.4 The magnetosphere of DENIS 1048−3956

The tightly constrained spectral index of the radio emission from DENIS 1048−3956, combined with the measurement of circular polarisation in the 6/3 cm band, allows a set of inferences to be made about the emission mechanism, magnetic field and plasma density around the star. I make use of the following facts:

- DENIS 1048−3956 is at a distance of $D = 4.3\,\mathrm{pc}$, with an effective diameter of the confined plasma of $L \sim 3$ stellar radii [Benz, Alef & Güdel 1995].
- I take the radius of DENIS 1048−3956 to be $R \sim 7 \times 10^6\,\mathrm{m}$, consistent with the commonly assumed radii for brown dwarfs [Burrows et al. 2001].

First, I derive the brightness temperature of the emission in order to constrain the emission mechanism. The brightness temperature in the Rayleigh-Jeans approximation is given by

$$T_b = \frac{c^2 S(\nu) \times 10^{-26}}{k_B \nu^2 \Omega} \tag{5.3}$$

where $S(\nu)$ is the observed flux at a frequency ν in Jy, and $\Omega = L^2/(D \times 3.08568 \times 10^{16})^2 \sim 2.8 \times 10^{-19}\,\mathrm{sr}$ is the solid angle subtended by the confined plasma. Then, from Table 5.3, I estimate T_b for $\nu = 5.224\,\mathrm{GHz}$ and $S(\nu) = 3.30 \times 10^{-4}\,\mathrm{Jy}$ as $T_b \sim 3.1 \times 10^9\,\mathrm{K}$. The choice of ν simply reflects the spectral point with the least error.

The fact that $T_b \sim 10^9\,\mathrm{K}$, coupled with the negative spectral index $\alpha = -1.7$ of the emission, implies optically thin gyrosynchrotron emission [Dulk 1985, Güdel 2002]. This describes gyromagnetic emission from mildly relativistic electrons with Lorentz factors $\gamma > 1.02$ (energies of more than 10 keV) through a plasma with an optical depth, caused by gyrosynchrotron self-absorption, of $\tau \ll 1$. This is the scenario previously proposed for DENIS 1048−3956 by Burgasser & Putman (2005), and for radio emission from other highly active brown dwarfs [Berger 2002], which has now been proved.

Gyrosynchrotron emission from a plasma forms a spectrum with two regions: an optically thick region at lower frequencies where the spectral index $\alpha \sim 2.5$ is positive, and an optically thin region at higher frequencies where the spectral index is negative and given by $\alpha = 1.22 - 0.9\delta$ [Dulk 1985]. Here, δ is the negative spectral index of the power law electron distribution $n(E)$ as a function of energy E

$$n(E) \propto E^{-\delta} \tag{5.4}$$

radiating in the plasma. Hence, the value of $\alpha = -1.7 \pm 0.6$ yields an electron spectral index of $\delta = 3.2 \pm 0.6$. This is well within the range for gyrosynchrotron radiation from a power law distribution of electrons; the generally considered range is $2 < \delta < 7$ [Güdel 2002].

The detection of the circular polarisation fraction of the emission at 6/3 cm yields an estimate of the magnetic field strength in the emitting region. While optically thick gyrosynchrotron emission does not allow for any circular polarisation, optically thin gyrosynchrotron emission includes a circularly polarised component with a fractional flux

$$r_c = 10^{3.35+0.035\delta}(\frac{\nu}{B})^{-0.51} \tag{5.5}$$

[Dulk 1985]. Given the values of $\delta = 3.2 \pm 0.6$ and $r_c = 0.24 \pm 0.05$ at a frequency $\nu = 7.25 \times 10^9$ Hz (the middle of the 6/3 cm band), I estimate the magnetic field strength as $B = 0.007 \pm 0.002$ T. This is in contrast to the field strength estimated by Burgasser & Putman (2005), which was ~ 0.1 T. Their value was based on the assumption that the pulses seen at 6 and 3 cm from DENIS 1048−3956 were coherent electron-cyclotron maser emission radiated at the fundamental cyclotron frequency $\nu_B = q_e B/(2\pi m_e)$. There could be three explanations for this discrepancy:

- First, the estimate of B from Equation 5.5 is actually the line-of-sight magnetic field strength, not the surface field strength of the star. Therefore, this result suggests that the average line-of-sight field strength is ~ 0.007 T, as opposed to describing the field strengths of any high-field regions closer to the star.

- Second, the field structures of brown dwarfs are not constrained: for example, they have not been shown to be dipolar. This is because of the diffuculty of measuring surface field strengths and hence magnetic field lightcurves [Reiners & Basri 2007]. Indeed, recent evidence based on simultaneous radio and optical $H\alpha$ observations of the periodically pulsing brown dwarf 2MASSW J0746425+200032 [Berger et al. 2009] indicates that its magnetic field is either dominated by a quadrupolar component, or that the emission zones are not symmetric about the dipole axis. Further, the lack of variability in the radio quiescent emission from 2MASSW J0746425+200032 was interpreted as this emission being dominated by field components on the largest scales not influenced by rotation. A similar scenario might be in effect for DENIS 1048−3956. We note that the Berger et al. (2009) did not consider the possibility of an offset dipole rotator; indeed, the dynamo field models normally applied to low mass stars [Güdel 2002] preclude this. Further monitoring and timing of the pulses from known brown dwarf pulsators, such as TVLM 513−46546 and 2MASSW J0746425+200032, is necessary to characterise the pulsed emission geometry and the magnetic field structures. Coherent pulses are powerful probes into the field structures because particular field strengths correspond to narrow emission bandwidths: the emission being radiated at the fundamental cyclotron frequency means that the field can be mapped by studying the dynamic spectral characteristics of the pulses.

- The third possibility, not wholly removed from the second, is that the quiescent emission originates from regions well away from the surface of the star, and that emission from close to the star is attenuated by opacity effects. In a simple dipole field model, assuming a surface polar field strength of $B_p = 0.1\,\mathrm{T}$ after Burgasser & Putman (2005) and a field dependence on radius r as $B(r) = B_p(R/r)^3$, the height of the quiescent emission region would be $r \sim 2.4R$. Regions closer to the star could possibly be much denser than regions further away. Evidence based on high-resolution Very Long Baseline Interferometry observations by Benz et al. (1995) of a number of M stars suggest that the radii of the confined plasma zones in the magnetospheres are $\sim 1.5R$. These regions could perhaps be extremely optically thick at our observing frequencies.

I end by constraining the electron number density in the quiescent emitting region of DENIS 1048−3956. The peak frequency of the non-thermal gyrosynchrotron spectrum ν_{pk}, separating the optically thick and optically thin regions of the spectrum, is given by

$$\nu_{pk} = 2.72 \times 10^3 \times 10^{0.27\delta} (\sin\theta)^{0.41+0.03\delta} (n_e L)^{0.32-0.03\delta} B^{0.68+0.03\delta} \tag{5.6}$$

[Dulk 1985], where θ is the viewing angle with respect to the magnetic field lines and n_e is the electron number density in cm^{-3} (B is the magnetic field strength in Gauss). From the fact that the spectrum of the quiescence from DENIS 1048−3956 (see Figure 5.4) does not appear to peak in any region, I take $\nu_{pk} < 4.731 \times 10^9$ Hz to constrain n_e. Using, from above, $L = 2.1 \times 10^9\,\mathrm{cm}$, $B = 70\,\mathrm{G}$, $\delta = 3.2$, and taking $\theta = \pi/3$ as an average viewing angle after Güdel (2002), we have $n_e < 2.7 \times 10^8\,\mathrm{cm}^{-3} = 2.7 \times 10^{14}\,\mathrm{m}^{-3}$. This is a tighter constraint that that placed by Burgasser & Putman (2005), which had $n_e < 2 \times 10^{15}\,m^{-3}$. In fact, this constraint is the tightest yet placed on the emitting regions of a brown dwarf magnetosphere. I note that the constraints discussed here are purely on the *non-thermal* populations of electrons: thermal components could also exist. No evidence is found for a hot thermal component in the emitting regions based on thermal gyrosynchrotron absorption features.

5.5 Conclusions

I have shown the following:

- While neither of the brown dwarfs DENIS 1048−3956 or LHS 3003 were observed to pulse or flare at 6 cm, 3 cm or 1.2 cm, and while LHS 3003 was not even detected in quiescence, DENIS 1048−3956 is a strong stable quiescent emitter with a power law spectrum of index of -1.7 ± 0.6 ranging across all observing bands. This is the first proof of a power law spectrum for a brown dwarf, and the first brown dwarf detection at 1.2 cm.

- The LHS 3003 observations did not reach the detection limit of $4\,\mu$Jy at 6 and 3 cm imposed by the Güdel-Benz relation from its X-ray luminosity. I suggest a two-state model for brown dwarf activity, between active radio-loud states and a quiet Güdel-Benz dominated state, and predict that sensitive observations of LHS 3003 down to $\sigma < 1.34\,\mu$Jy would detect a persistent radio source at 3σ. DENIS 1048−3956 violates the Güdel-Benz relation: I consider it in the active radio-loud state.

- The emission from DENIS 1048−3956 is caused by a gyrosynchrotron mechanism in an optically thin ($\tau \ll 1$) plasma with a power law electron energy distribution with index $-\delta = -3.2$.

- The average line-of-sight field strength in the emission region is 0.007 ± 0.002 T, as derived from the circular polarisation fraction at 6/3 cm of 0.24 ± 0.05. The stability of the emission indicates a stable, rotation-independent large-scale component of the magnetic field that dominates the quiescent emission, as opposed to the high-field component from which the pulses observed by Burgasser & Putman (2005) for DENIS 1048−3956 must have originated.

- The non-thermal electron number density in the quiescent emitting regions is less than $2.7 \times 10^{14}\,\mathrm{m}^{-3}$. This is a tighter constraint than that of Burgasser & Putman (2005) by an order of magnitude, and is the tightest such constraint on a radio-loud brown dwarf.

A radio survey of a large sample of brown dwarfs down to the Güdel-Benz detection thresholds is necessary to prove the existence of two activity states in magnetic brown dwarfs, and to characterise the transition between the states. Timing observations of known or newly detected brown dwarf pulsators would also help characterise the pulse emission mechanism, emission region and geometry, and the masss loss. Radio-loud brown dwarfs appear to form an ever-expanding component of the radio transient sky, and it is imperative that this fascinating popoulation is characterised.

5.6 Appendix - Lightcurves of DENIS 1048−3956 and LHS 3003

The lightcurves made from the observations of DENIS 1048−3956 and LHS 3003 are shown in the following few pages. Each observing timespan, listed in Table 5.1, has lightcurves displayed in Stokes I and Stokes V. Time averaging intervals of 10 s, 1 minute and 10 minutes are used. Horizontal dashed lines show the $\pm 1\sigma$ and $\pm 3\sigma$ levels.

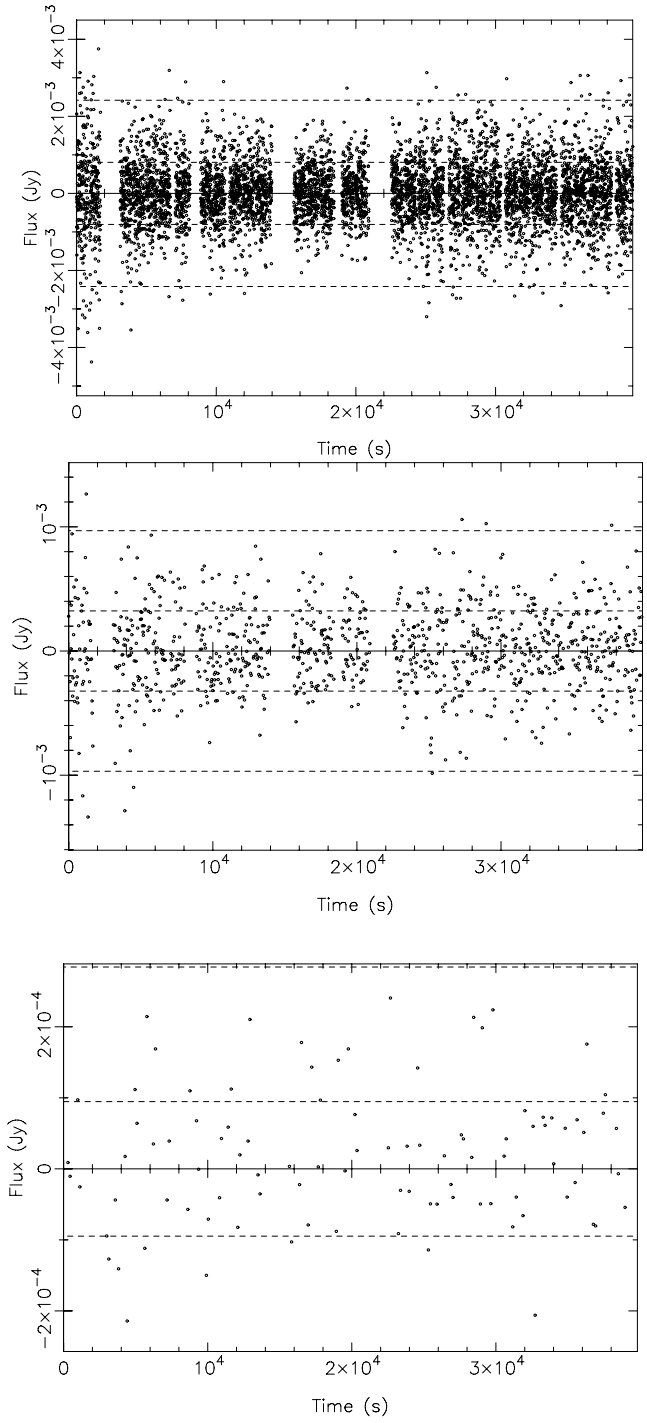

Fig. 5.5: Stokes I lightcurves of DENIS 1048−3956 during 2009 August 10 at 1.2 cm. Time averaging is (from top) over 10 s, 1 min and 10 min.

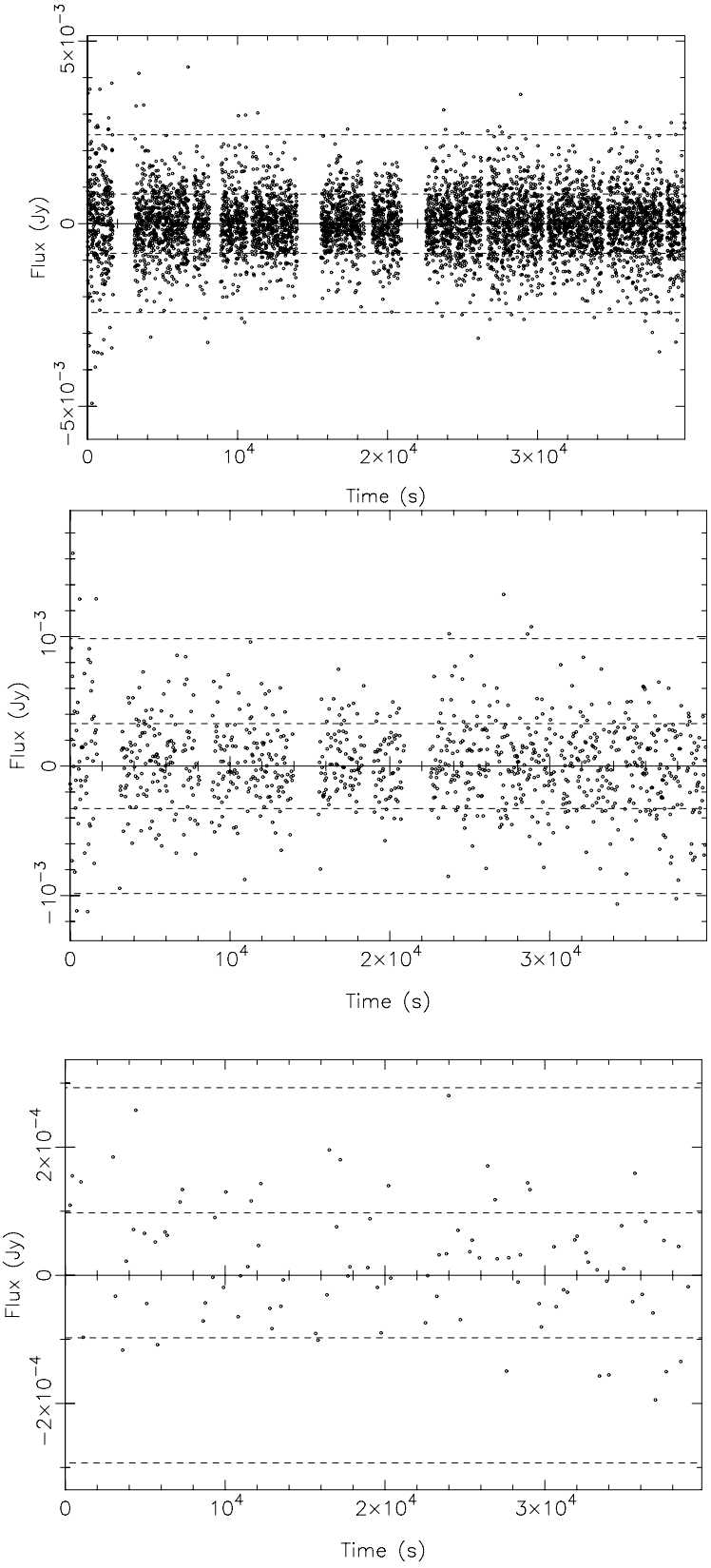

Fig. 5.6: Stokes V lightcurves of DENIS 1048−3956 during 2009 August 10 at 1.2 cm. Time averaging is (from top) over 10 s, 1 min and 10 min.

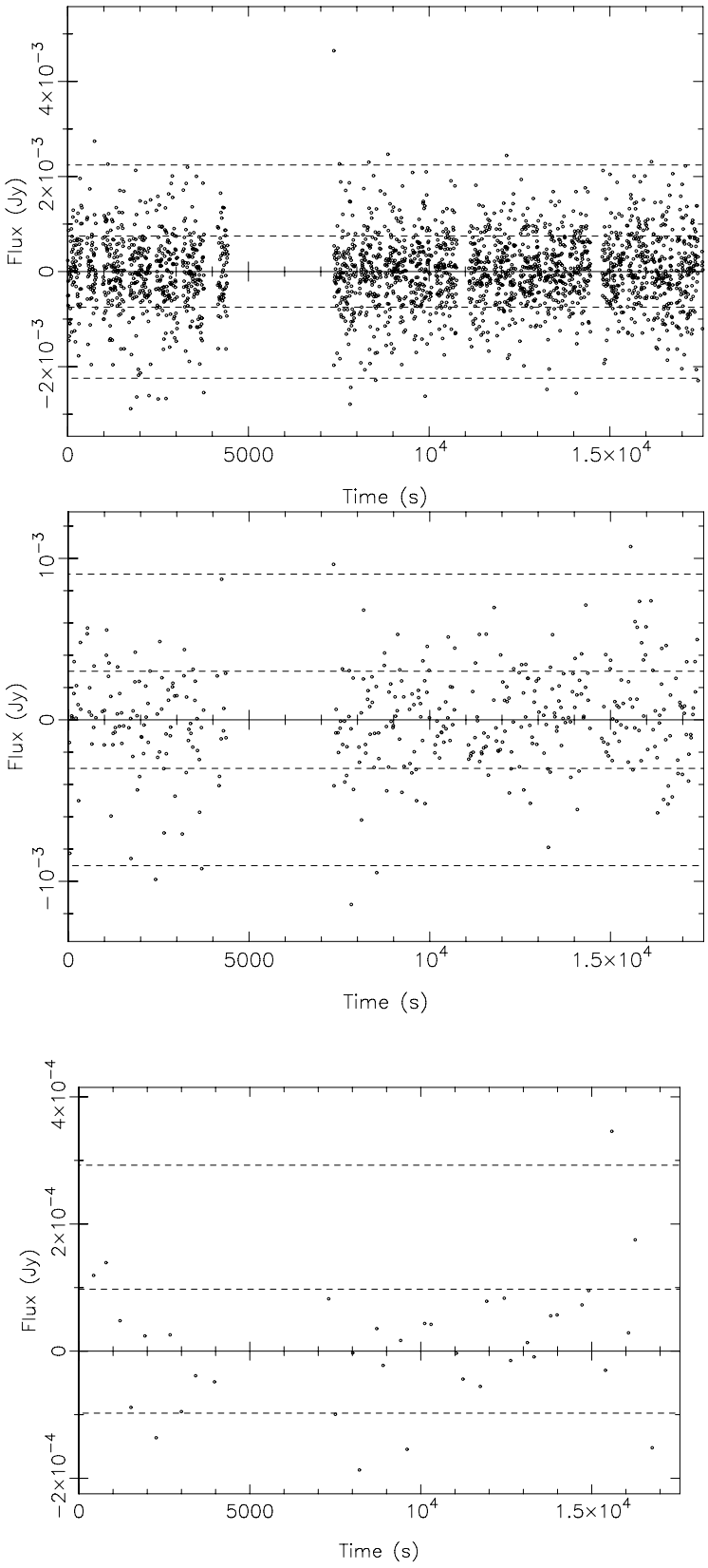

Fig. 5.7: Stokes I lightcurves of DENIS 1048−3956 during 2009 August 11 at 1.2 cm. Time averaging is (from top) over 10 s, 1 min and 10 min.

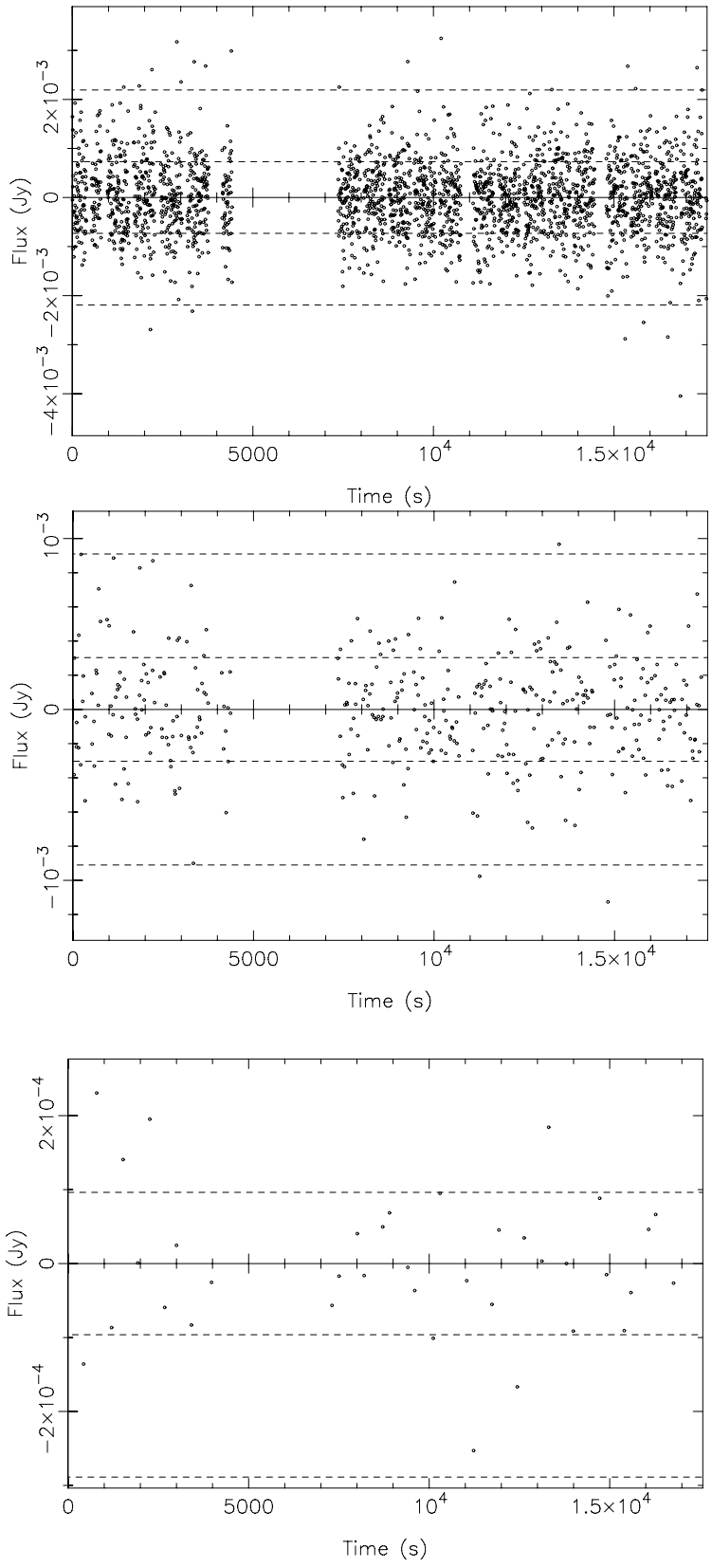

Fig. 5.8: Stokes V lightcurves of DENIS 1048−3956 during 2009 August 11 at 1.2 cm. Time averaging is (from top) over 10 s, 1 min and 10 min.

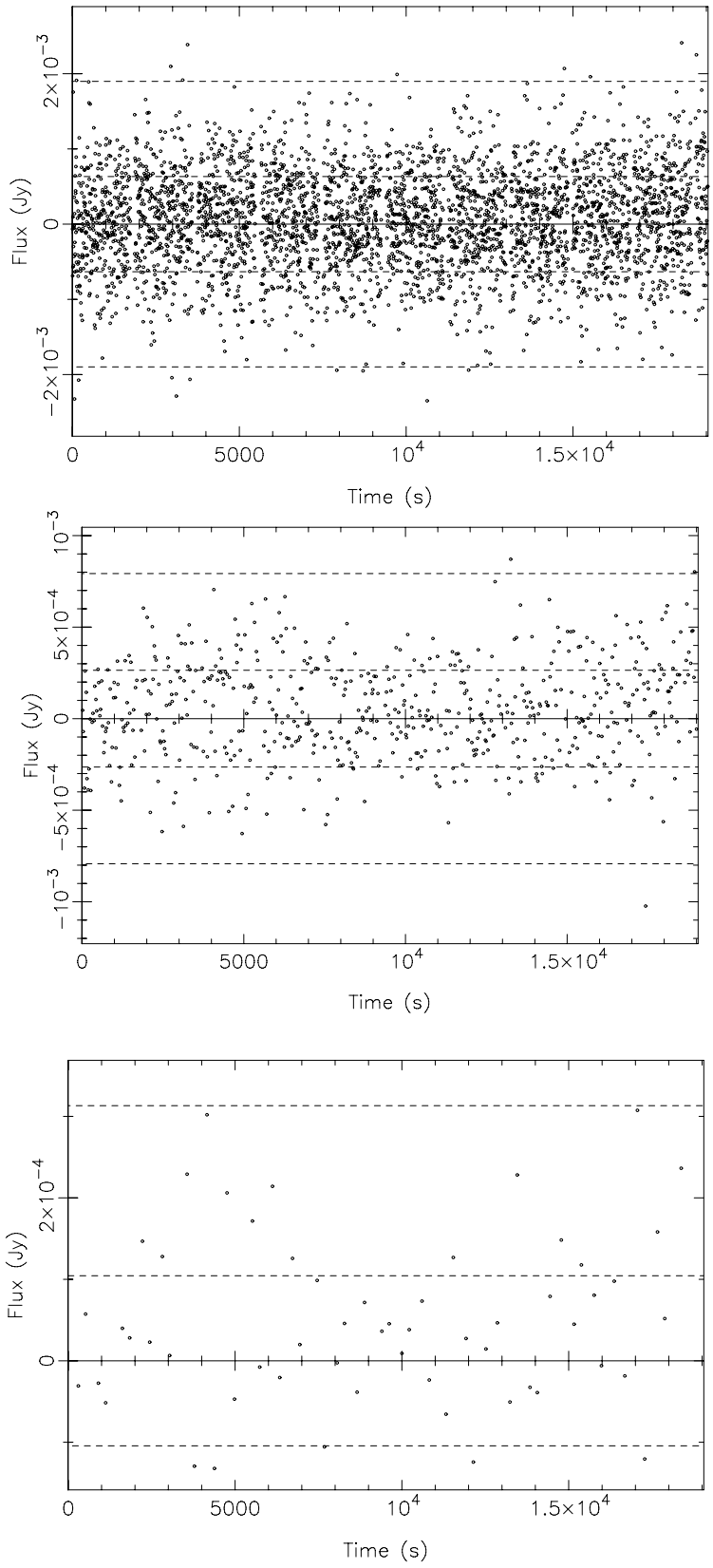

Fig. 5.9: Stokes I lightcurves of DENIS 1048−3956 during 2009 August 15 at 6 and 3 cm combined. Time averaging is (from top) over 10 s, 1 min and 10 min.

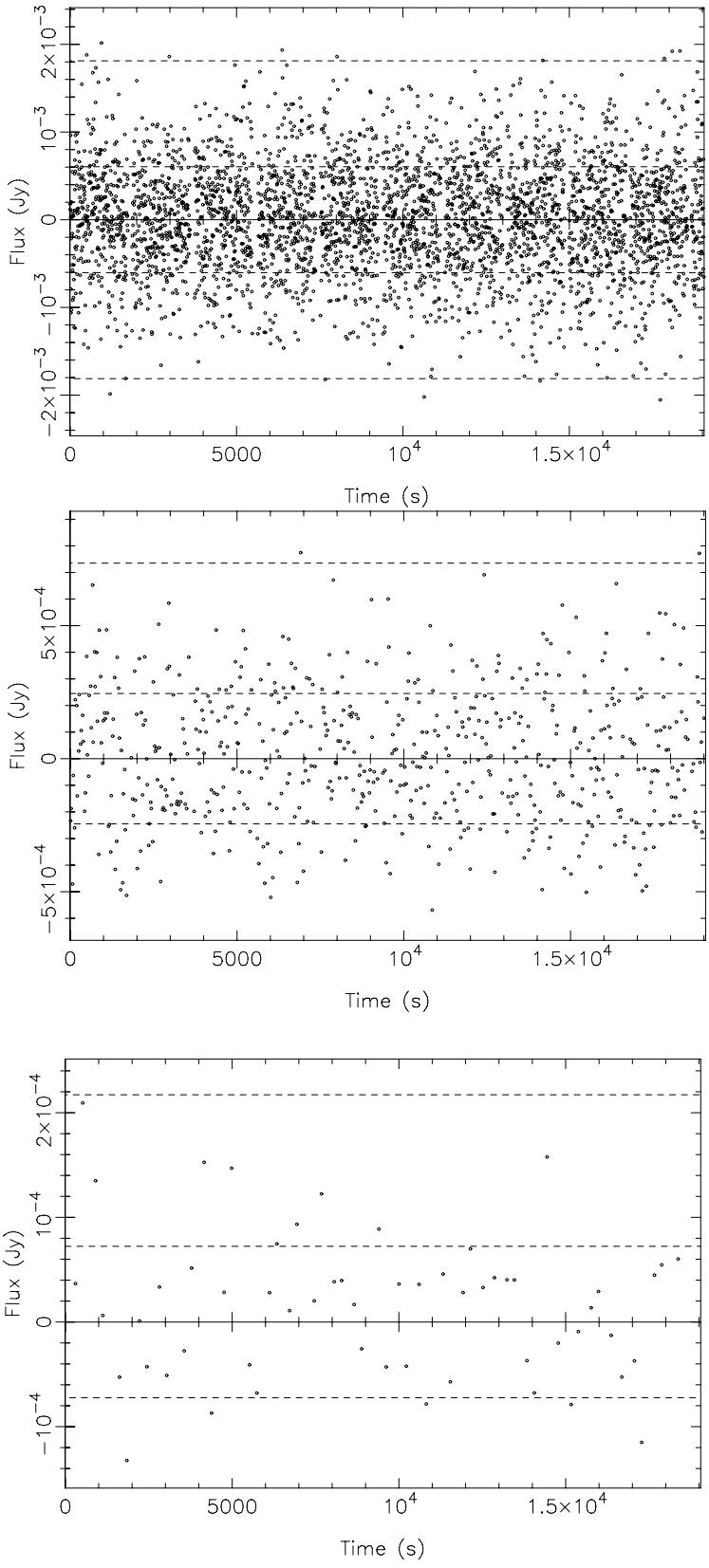

Fig. 5.10: Stokes V lightcurves of DENIS 1048−3956 during 2009 August 15 at 6 and 3 cm combined. Time averaging is (from top) over 10 s, 1 min and 10 min.

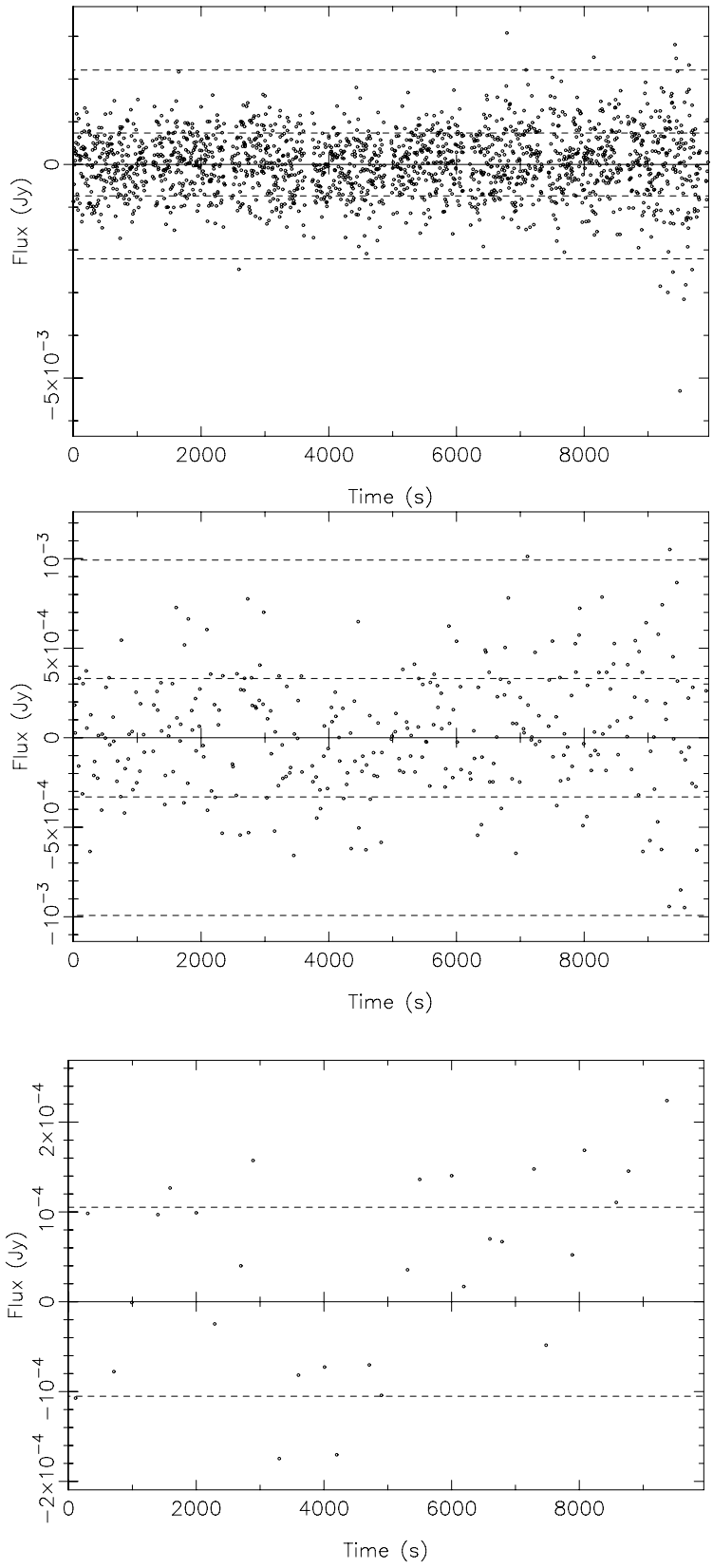

Fig. 5.11: Stokes I lightcurves of LHS 3003 during 2009 August 13 at 6 and 3 cm combined. Time averaging is (from top) over 10 s, 1 min and 10 min.

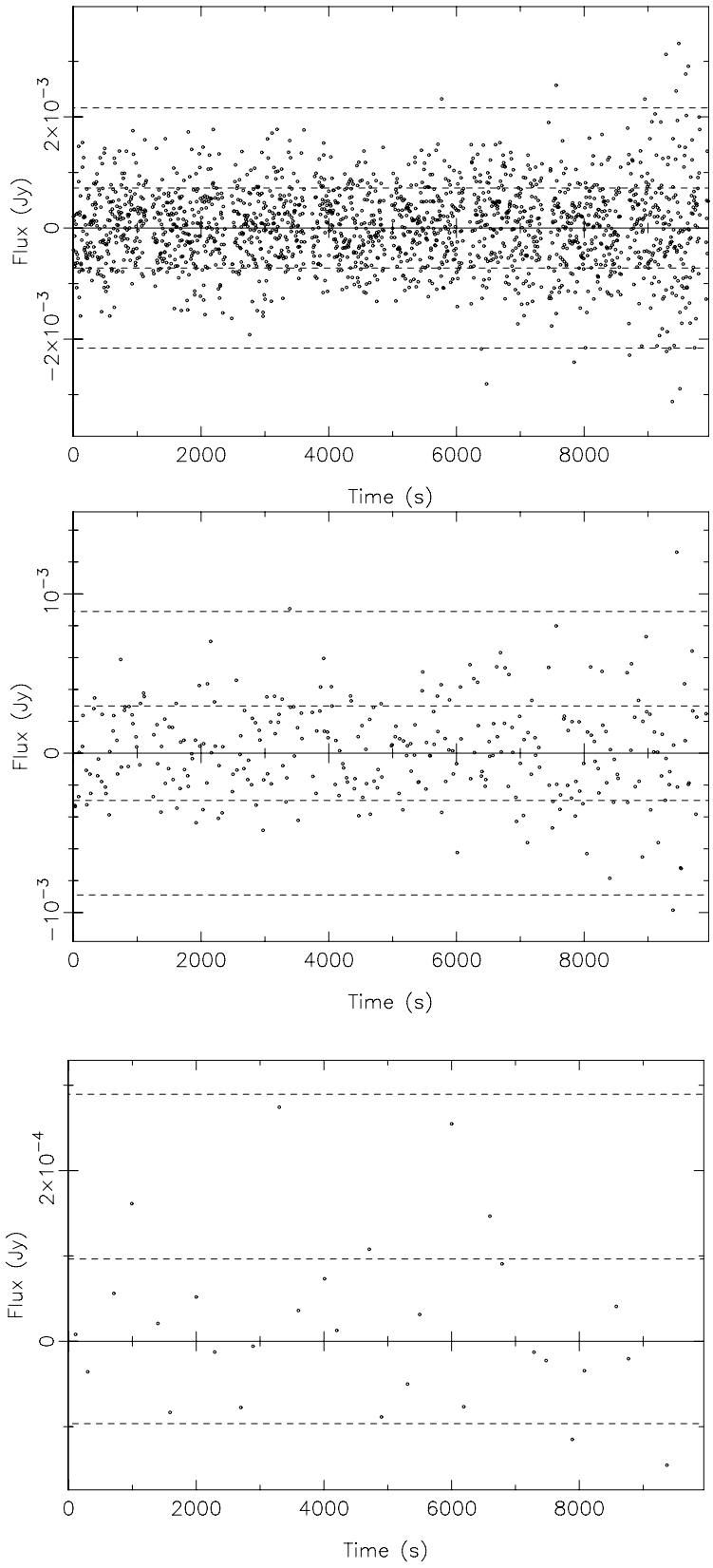

Fig. 5.12: Stokes V lightcurves of LHS 3003 during 2009 August 13 at 6 and 3 cm combined. Time averaging is (from top) over 10 s, 1 min and 10 min.

Isolated Highly Magnetic White Dwarfs as Pulsars

Abstract

Isolated highly magnetic white dwarfs are close analogues of radio pulsars, with slightly slower rotation rates and slightly weaker magnetic fields. I present observations of the white dwarfs EUVE J0317−853 and PG 1031+234 with the ATCA at 20 and 13 cm, that target transient and quiescent emission from the magnetospheres of these sources. No emission was detected. I also analyse archival data of EUVE J0317−853 during which a large circularly polarised flare was thought to be observed: again, no emission was detected. The flux limits on the quiescence of the targets are used to derive constraints on the magnetosphere electron densities, and these are compared with theoretical predictions in a Goldreich-Julian model for highly magnetic white dwarf magnetospheres.

6.1 Introduction

Isolated magnetic white dwarfs are thought to constitute more than 15% of the white dwarf population [Kawka et al. 2003]. Of these, the vast majority, with magnetic field strengths in excess of 100 T, are highly magnetic [Ferrario & Wickramasinghe 2005]. More than ~ 150 highly magnetic white dwarfs (HMWDs)[1] are known [Vanlandingham et al. 2005], with field strengths ranging between 10^2 and 10^5 T. The magnetic fields of HMWDs are generally dipoles offset from the rotation axis with detritus magnetic spots. The formation mechanisms of HMWDs are not completely characterised. Connections have been drawn between magnetic Ap stars on the main sequence and HMWDs in terms of magnetic flux conservation [Ferrario & Wickramasinghe 2005]. However, the high mean mass of the HMWD population with respect to the total white dwarf population has led some authors to suggest that HMWDs are formed in stellar mergers [Ferrario et al. 1997, Tout et al. 2008]. These mergers can either be double-degenerate (between two white dwarfs) or occur in magnetic cataclysmic variables (CVs) (between a white dwarf and a low mass main sequence companion). A significant fraction of HMWDs have rotation periods measurable from spectrophotometric periodic variations. Two distinct populations of rotating HMWDs can be identified: slow rotators with periods on the order of months (common with most white dwarfs), and extremely fast rotators with periods ranging from minutes to hours. The former

[1] I stress that in this thesis a HMWD is an *isolated* magnetic white dwarf. Isolation implies non-accretion of matter from any companion star.

population is tentatively identified with single massive stellar progenitors, and the latter population with binary mergers [Ferrario & Wickramasinghe 2005].

Both quiescent and flaring radio emission has been detected from magnetic CVs. To date, seven systems, three of which are highly magnetic (known as *polars*[2]), have exhibited flaring emission. The flares do not appear to be periodic, and are believed to be non-thermal in origin. However, only two polar systems (AM Herculis, AE Aquarii) appear to be persistent on timescales of decades, both in flaring and in quiescence [Mason & Gray 2007]. The quiescence in AM Herculis is explained by gyrosynchrotron emission in the white dwarf magnetosphere, and the flaring by coherent emission mechanisms in the atmosphere of the companion red dwarf [Dulk, Bastian & Chanmugam 1983]. The electron acceleration mechanism is as yet unclear, but has been modelled as being caused by the magnetic field of the companion interacting with the strong white dwarf magnetic field [Mason & Gray 2007]. AE Aquarii is a much more complex system than AM Herculis: the white dwarf in AE Aquarii is the fastest known rotating white dwarf with a period of 33 s [Venter & Meintjes 2006][3]. This extremely short period is believed to be caused by accretion from the companion star, which led to an addition of angular momentum to the white dwarf. This is analogous to the proposed mechanism for the formation of millisecond pulsars [Backer et al. 1982], where an old neutron star is similarly spun-up by a companion star.

No radio emission has been detected from an isolated HMWD. Searches at the positions of known HMWDs in large-area radio surveys have yielded no detections [Mason & Gray 2007]. Barrett et al. (1999) report the detection of a single highly circularly polarised flare from the HMWD EUVE J0317-853, but no further detection − quiescent or flaring − was observed in follow-up observations. The detection of the flare itself is in some doubt (see below). No targeted survey for radio emission from HMWDs has been published.

There are numerous similarities between radio pulsars [Hewish et al. 1968] and HMWDs. Pulsars are neutron stars formed from more massive progenitors than those that form white dwarfs. Pulsars are characterised by short duty-cycle highly periodic radio pulses, with rotation periods ranging from a few milliseconds to a few seconds. Pulsar magnetic fields are modelled as offset dipoles, and range from 10^4 to 10^8 T [Ferrario & Wickramasinghe 2007]. The radio pulses are thought to be caused by a coherent emission mechanism in localised regions near the magnetic poles. This mechanism is not constrained. The emission mechanism is fed by the pulsar wind: a relativistic outflow of electrons putatively driven by the strong electric potentials induced by the rotating magnetic field [Goldreich & Julian 1969].

[2] This is because of their highly polarised appearance at optical wavelengths. Less highly magnetic CV systems are known as *intermediate polars*.

[3] Recent results, however, have shown that a faster rotating system, RX J0648.0-4418, is in fact a white dwarf with a 13.2 second rotation period in a close binary system [Mereghetti et al. 2009]. However, this system is not a polar or even an intermediate polar.

No quiescent emission is observed from the pulsar wind. This is thought to be because the pulsar wind electrons are concentrated at small pitch angles, which preclude isotropically beamed synchrotron emission [Gaensler et al. 2000]. However, some pulsars that reside in regions of dense interstellar medium − such as remnants of the supernovae that created them − form pulsar wind nebulae (PWNe) [Gaensler & Slane 2006]. Synchrotron and inverse-Compton radiation is observed from PWNe when the ram pressure of the pulsar wind matches that of the interstellar medium, because the electron pitch angles are randomised at the resulting shock. PWNe are important probes of pulsar wind properties.

This chapter focuses on two HMWDs: EUVE J0317−853 (hereafter J0317) and PG 1031+234 (hereafter PG1031). J0317 was discovered and characterised by Barstow et al. (1995) as the hottest known HMWD, with an effective surface temperature $T_{eff} \sim 50000\,\mathrm{K}$ and a dipole magnetic field with a polar field strength of $\sim 3.4 \times 10^4\,\mathrm{T}$. It is also one of the fastest known HMWD rotators, with a period of $\sim 725\,\mathrm{s}$. Ferrario et al. (1997) suggested that J0317 is the result of a double-degenerate merger, based on its high mass close to the Chandrasekhar limit and its much younger age than its nearby visual binary (non-interacting) white dwarf companion. PG1031 has the highest magnetic field among known HMWDs [Schmidt et al. 1986]. The field has been modelled as a slightly offset dipole with a polar strength of $\sim 5 \times 10^4\,\mathrm{T}$, convolved with a number of magnetic spots with strengths of up to $\sim 2 \times 10^5\,\mathrm{T}$ [Latter, Schmidt & Green 1987]. PG1031 is also a fast rotator, with a period of ~ 3.4 hours. No interacting companion is known.

The aim of this study is twofold: to attempt to detect radio emission from HMWDs, quiescent or transient, and to present a framework to characterise the plasma environments of HMWDs through radio flux limits. I consider three key properties of the magnetospheres of HMWDs: the magnetospheric plasma densities, the energetics of possible stellar winds, and whether such winds consist of electrons with isotropic or anisotropic pitch angle distributions. These properties are observationally constrained and theoretically estimated for PG1031 and J0317. I also discuss the theoretical detectability of radio emission from HMWDs, using PG1031 and J0317 as extreme cases.

The fast-rotating population of HMWDs, of which PG1031 and J0317 are part, are close analogues to pulsars. Millisecond pulsars have magnetic fields on the order of $10^4 - 10^5\,\mathrm{T}$ [Ferrario & Wickramasinghe 2007], similar to HMWDs. The offset dipole magnetic field structures are also common. While the rotation periods of HMWDs are longer than those of pulsars, particularly millisecond pulsars, the greater size of white dwarfs leads to less disparate surface rotation velocities. Some evidence also exists for cyclotron line-driven winds around HMWDs [Zheleznyakov & Serber 1994], and such a scenario has been proposed for J0317 [Barstow et al. 1995]. The electrodynamic arguments that explain pulsar winds have also been applied to the fast-rotating white dwarf in AE Aquarii [Ikhsanov, Neustroev & Beskrovnaya 2004] to successfully model its spin-down.

This study is motivated by the close physical similarities between HMWDs and pulsars. Pulsars are the archetypal stellar radio transients. I discuss limits on the plasma environments in the magnetospheres of PG1031 and J0317 based on observational constraints. Understanding the pulsar emission mechanism has proved difficult because of the lack of observational constraints on neutron star magnetospheres. The pulsar wind mechanism, crucial to understanding how the pulsar emission mechanism is fed, is similarly ambiguous. However, in the case of HMWDs, magnetospheric properties can be probed using a number of independent techniques, enabling the stellar wind and emission physics to be constrained.

Upcoming large-area continuum imaging and transient surveys with next generation radio telescopes will target the transient radio sky. It is therefore important to characterise transient emitters. By characterising the magnetospheres of HMWDs, I attempt to understand whether HMWDs could form part of the stellar radio transient population as pulsar analogues.

The structure of this chapter is as follows. In §2, I outline the observing and analysis techniques used to constrain the emission from PG1031 and J0317 with the ATCA. In §3, I present the flux limits and report that the flare reported by Barrett et al. (1999) for J0317 was non-existent. In §4, I constrain the plasma density of PG1031 and J0317 by considering two emission models. In §5, I consider the electrodynamics of HMWD magnetospheres, and discuss the spin down properties and the consequences of anisotropic pitch angle distributions in the wind. Finally, in §6, I discuss the results and the implications for the detectability of radio emission from HMWD magnetospheres. The conclusions about HMWD magnetospheres are summarised in §7.

6.2 Observing and data analysis

PG1031 (10:33:49.18,+23:09:16.2) and J0317 (03:17:04.6,−85:32:35) were observed intermittently between 2008 October 30 and 2008 November 3 with the ATCA in its fully extended 6A configuration. A dual-band receiver providing two 128 MHz bandwidths was used. One bandwidth was centred either on 1344 MHz or 1384 MHz (20 cm), and the other bandwidth was centred on 2368 MHz (13 cm). Data were recorded in 32 channels across each of the bands, with integration times of 10 s. Flux, bandpass and polarisation calibrations were obtained from either of the ATCA primary calibrators PKS 1934−638 and PKS 0833−500, depending on which was above the horizon at the time of observation. Five minute observations of a secondary calibrator were also undertaken at 20 minute intervals for phase and gain calibrations. These calibrators, along with other relevant observing parameters, are listed in Table 6.1. Data in all polarisations were recorded.

Source	Start (UT)	T_{obs}	Cal 1	Cal 2	Centre frequency (MHz)	Beam size
PG1031	31/10/08 18:39	6.43	PKS0823-500	PKS1019+222	1344,2368	10"×27",6"×15"
J0317	30/10/08 12:23	5.17	PKS1934-638	PKS0606-795	1384,2368	10"×10",6"×6"
	1/11/08 16:22	1.38	PKS0823-500		1344,2368	
	2/11/08 7:56	12.13	PKS1934-638		1344,2368	
	3/11/08 12:02	4.03	PKS1934-638		1344,2368	

Tab. 6.1: ATCA observing log for PG1031 and J0317. T_{obs} is the on-source time in hours, and Cal 1 and 2 are the primary and secondary calibrators respectively. The beam size gives the synthesised beam dimensions.

The phase centres for all on-source observations were placed 10" South of the actual source positions (obtained from SIMBAD) in order to avoid the possibility of image artefacts at the ATCA pointing centre.

I carried out the data reduction using the MIRIAD software package. The analysis was aimed both at detecting the HMWDs as persistent quiescent emitters as well as at finding pulses or flares. Narrow-band and short-timescale interference was removed from the visibilities, along with any short-timescale amplitude excursions in the secondary calibrator data. The four shortest baselines were removed from the 20 cm data to reduce image confusion by extended sources. The polarisation calibrations were always obtained from the primary calibrator data because the secondary calibrator visibilities invariably had a limited parallactic angle coverage. The visibilities were imaged out to three primary beam FWHM in order to allow effective subtraction of all field sources. The strongest nearby sources were individually 'peeled' from the visibilities [Noordam 2004]: the phase centres were shifted to their positions, self-calibration was carried out using the MIRIAD task GPSCAL, and the final source models constructed using the MIRIAD CLEAN task were subtracted from the visibilities. The phase centres were shifted to the target positions and self calibration was applied using strong (> 5 mJy) sources within the central primary beam FWHM. All sources detected to greater than 6σ beyond three synthesised beams from the target positions, and within one primary beam FWHM, were then modelled using CLEAN and subtracted from the visibilities.

Source-subtracted lightcurves were constructed for each observing band in all Stokes polarisations by vector-averaging the visibilities. The averaging was conducted over time bins of different lengths to check for variability and flaring of different timescales. The timescales ranged from the length of the shortest observation of the source to the 10-second integration times. On all timescales, the detection threshold for variability or flares was taken to be a factor of six above the rms spread of the time series, as before in Chapter 5.

The source-subtracted visibilities were also imaged in all Stokes parameters in each band to one primary beam FWHM using multi-frequency synthesis to combine the frequency channels. The primary beam FWHM were 35' and 20' at 20 and 13 cm respectively for both sources. Regions with flux greater than 3σ were searched for within three synthesised beams of the source positions. The σ-values were measured by taking the standard deviations of the image values everywhere except within three synthesised beams of the source positions. In the analysis of the time-variability and quiescence of J0317, data taken using the different centre frequencies in the 20 cm band (1344 and 1384 MHz) were combined using the MIRIAD task UVAVER.

This procedure was repeated for archival observations of J0317 during 1996 March 26 from which Barrett et al. (1999) reported a "strong, highly circularly polarised" flare. No source subtraction was attempted given the short observing

Source	$S_{20\,cm}$	$S_{13\,cm}$	$S_{6\,cm}$ (1)
J0317	120	105	345
PG1031	204	165	–

Tab. 6.2: 3σ Stokes I quiescent flux constraints (in μJy) on emission from J0317 and PG1031. 1) This value of sigma was determined by taking the standard deviation of an image area with no 6σ sources, because of the poor image quality.

time and highly incomplete coverage of the u-v plane. These observations were made using the 6A configuration, and lasted for 64 minutes. The centre frequencies were 4800 and 5056 MHz, both within the 6 cm band. Data were recorded in 32 channels across two 128 MHz bandwidths with all polarisations. The primary calibrator was PKS 1934−638, and the secondary calibrator was PKS 0230−790. The synthesised beam had dimensions 3"×3". As with the J0317 data at 20 cm, the 6 cm image was constructed by combining data in the two bandwidths.

6.3 Results

None of the observations detected any flaring or quiescence in any polarisation at any frequency. No flares or variability greater than three times the time-series rms were found in any of the lightcurves on any timescale. Furthermore, no sources greater than 3σ were found within three synthesised beams of the source positions in the images. Table 6.2 lists the 3σ Stokes I constraints I place on the source fluxes at all frequencies.

This non-detection is particularly concerning for the 1996 observations of J0317, in the light of the claims of Barrett et al. (1999). Figure 6.1 shows the quiescent Stokes I lightcurves during this observation, prepared similarly to those in Figures 5.1 to 5.8 for DENIS 1048−3956 and LHS 3003. Averaging is on timescales of 10 seconds, 1 minute and 10 minutes. Figure 6.2 shows a "dirty" image made from this observation. The lack of even any 3σ contours in this image indicates the complete lack of any detections. The analysis technique has proven robust when applied to pulses from CU Vir, as well as the DENIS 1048−3956 quiescent detections. I therefore suggest that the result of Barrett et al. (1999) is incorrect, and that no radio flare was detected from J0317.

6.4 Observational constraints on the magnetosphere plasma

Indirect evidence exists for stellar winds around white dwarfs. Some authors [Zheleznyakov & Serber 1994, Barstow et al. 1995] posit the existence of cyclotron line radiation driven winds from hot HMWDs (including J0317), and interpret certain absorption features in the ultraviolet (UV) spectra of these stars as fundamental frequency cyclotron scattering. Others have derived the spin-down rate of the

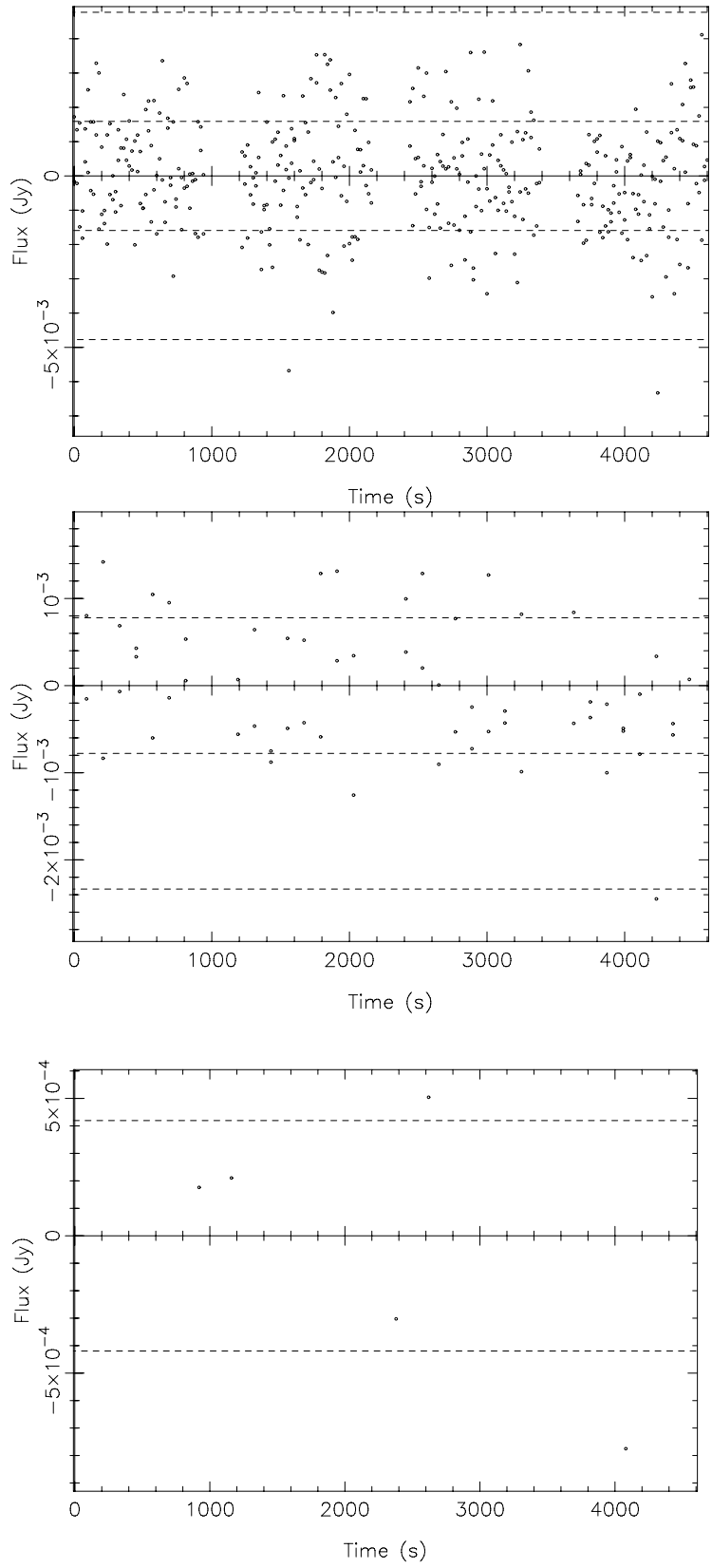

Fig. 6.1: Stokes I lightcurves of J0317 during 1996 March 26 at 6 cm. Time averaging is (from top) over 10 s, 1 min and 10 min. The horizontal dashed lines show the $\pm1\sigma$ and $\pm3\sigma$ cutoffs.

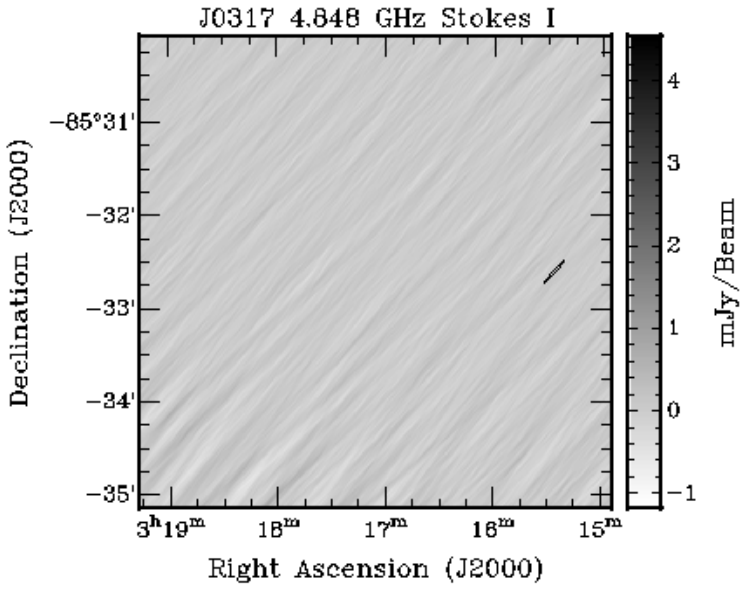

Fig. 6.2: Stokes I image of J0317 during 1996 March 26 at 6 cm. The image noise was $\sigma = 115\,\mu$Jy, and contours were placed at $\pm 3\sigma$, $\pm 4\sigma$ and $\pm 5\sigma$: none are visible in the image. This was the epoch during which Barrett et al. (1999) reported a "strong, circularly polarised flare." The synthesised beam shape is shown to the right of the image, and the colour bar shows the flux scale.

extremely fast-spinning white dwarf in AE Aquarii using a pulsar-like magnetic braking mechanism [Ikhsanov, Neustroev & Beskrovnaya 2004]. Such a mechanism is in fact essential for this white dwarf because its bolometric luminosity is not sufficient to explain the spin-down.

I derive a set of observational constraints on the magnetosphere plasma densities of J0317 and PG1031 by applying a series of assumptions about possible radio emission mechanisms. I first outline the theoretical framework, and then present the results of the calculations. Much of the theory in this section was adapted from Dulk (1985). The stellar parameters that I shall use in the calculations, including the distances D, masses M, polar magnetic field strengths B_p, rotation periods P and effective surface temperatures T_s are listed in Table 6.3. Given that neither PG1031 nor J0317 have accurately determined radii, I estimate the radii L as 0.01 solar radii [Liebert 1980].

In the Rayleigh-Jeans approximation to the low-frequency end of the blackbody spectrum, the brightness temperature T_b of a source with measured flux S_ν (Jy) at frequency ν is

$$T_B \Omega = \frac{c^2 S_\nu \times 10^{-26}}{k_B \nu^2} \tag{6.1}$$

where $\Omega = L^2/D^2$ is the apparent source solid angle.

I begin by making the following assumptions about the magnetospheres of HMWDs:

Parameter	PG1031	J0317
D (pc)	220 (3)	330 (6)
M (solar masses)	0.93 (1)	1.34 (4)
B_p (T)	5×10^4 (2)	4.5×10^4 (5)
P (s)	12240 (2)	726 (5)
T_s (K)	15000 (3)	50000 (6)

Tab. 6.3: Stellar properties for PG1031 and J0317. See text for an explanation of the symbols. *References: 1) Wickramasinghe & Ferrario (2005); 2) Latter, Schmidt & Green (1987); 3) Schmidt et al. (1986); 4) Ferrario et al. (1997); 5) Vennes et al. (2003); 6) Barstow et al. (1995).*

- The magnetospheres of HMWDs are optically thin at radio frequencies. I justify this, somewhat weakly, with the lack of evidence for radio emission from HMWDs. If HMWD magnetospheres were optically thick, with frequency-dependent optical depths $\tau_\nu \gg 1$, the brightness temperature T_b of the emission would be the same as the effective temperatures T_{eff} of the emitting electrons: $T_{eff} = T_b$. This is the highest possible value of T_b, and the lack of radio emission implies attenuation.

- I assume, for now, that the electron pitch angles in the plasma are randomised. Unlike pulsars, where the surface is a hard crust [Gaensler & Slane 2006], white dwarfs possess a thermal electron-proton plasma in the photosphere [Liebert 1980], which is here assumed to be subject to acceleration either by simple electrodynamic or by radiative forces. Like all thermal plasmas, the pitch angles are initially randomised, and I assume for now that the acceleration processes do not change this.

- I ignore bremsstrahlung emission and absorption, because of the high magnetic fields and low plasma densities involved. Instead, I consider mildly relativistic thermal and non-thermal power-law gyrosynchrotron mechanisms as the possible sources of radio emission. The brehmsstrahlung flux is proportional to the plasma number density n and plasma temperature T_p as $F \propto n^2 T_p^{1/2}$, whereas the thermal gyrosynchrotron flux behaves as $F \propto nT_p^a B^b,\ a, b > 1$, where B is the magnetic field strength.

In the optically thin regime, with $\tau_\nu \ll 1$, the effective temperature of the radiating electrons is related to the observed brightness temperature as $T_{eff} = T_b/\tau_\nu$. The optical depth is expressed in terms of a constant absorption coefficient κ_ν and the stellar diameter lengthscale L as $\tau_\nu = \kappa_\nu L$. The emission coefficient η_ν is defined as $\eta_\nu = \kappa_\nu k_B T_{eff} \nu^2/c^2$. Then, from the expression for T_{eff} in terms of T_b, the emission coefficient is given by

$$\eta_\nu = \frac{k_B T_b \nu^2}{Lc^2} \tag{6.2}$$

	J0317		PG1031	
Constraint	20 cm	13 cm	20 cm	13 cm
N_{TH}	2.94×10^{49}	4.49×10^{49}	3.40×10^{53}	1.55×10^{53}
N_{NTH}	4.35×10^{6}	6.62×10^{6}	3.30×10^{6}	1.50×10^{6}

Tab. 6.4: Upper limits for the electron number densities (in m^{-3}) in the magnetospheres of PG1031 and J0317.

I now consider numerical expressions for the emission coefficient from Dulk (1985) for thermal and non-thermal power-law gyrosynchrotron mechanisms, to derive upper limits for the electron densities in the magnetospheres of J0317 and PG1031. Both expressions are averaged over the viewing angle with respect to the magnetic field. In both cases, the maximum contribution to the emission is between harmonic numbers 10 and 100 [Dulk 1985]: the emission primarily occurs in regions of the magnetospheres where the cyclotron frequency $\nu_B = q_e B/2\pi m_e$ is between 1/10 and 1/100 of the observing frequency. I assume $\nu/\nu_B \sim 10$. This means that for ν =1.4 GHz (20 cm emission), $B = 5.00 \times 10^{-3}$ T, and that for ν =2.4 GHz (13 cm emission), $B = 8.57 \times 10^{-3}$ T.

Thermal gyrosynchrotron emission necessitates a thermal stellar wind with electrons in a Maxwellian distribution. I take the temperature of the radiating electrons to be isothermal with the surface effective temperature T_s. The thermal electron density N_{TH} (m^{-3}) is given by

$$N_{TH} = \eta_\nu (1.875 \times 10^{17} \times T_s^8 \nu^{-10} B^{11})^{-1} \tag{6.3}$$

I next consider a non-thermal stellar wind obeying a power law energy distribution such that the number of electrons n at an energy U is given by

$$n(U) = KU^{-\delta} \tag{6.4}$$

Here, K is a constant, and δ is the negative spectral index of the distribution. I derive the following expression for the wind electron density:

$$N_{NTH} = \eta_\nu (1.836 \times 10^{-14} \times B \times 10^{-0.52\delta} \times 10^{1.22-0.9\delta})^{-1} \tag{6.5}$$

and choose $\delta = 3$ after Dulk (1985). The viewing angle with respect to the magnetic field lines has been averaged using this index.

A third constraint on the magnetosphere plasma density can be applied by invoking Razin-Tsytovich suppression of gyrosynchrotron emission for frequencies where the refractive index deviates significantly from unity [Dulk 1985]. For the mildly relativistic regime under consideration here, suppression occurs at frequencies below ν_p^2/ν_B, where $\nu_p = 9\sqrt{N}$ is the fundamental plasma frequency. If we assume that no flux is visible from PG1031 and J0317 at 20 and 13 cm because of suppression of the emission, then a limit for N can be derived by assuming

suppression at wavelengths longer than 13 cm (frequencies less than 2.4 GHz):

$$N_{RT} \geq \frac{2.4 \times 10^9}{81} \nu_B \tag{6.6}$$

In the assumption of emission at the 10^{th} cyclotron harmonic, we simply have $\nu_B = 2.4 \times 10^8$ Hz, which places a constraint on the electron number density of $N_{RT} \geq 7.11 \times 10^{15}\,\mathrm{m}^{-3}$.

The thermal and non-thermal constraints on N_{TH} and N_{NTH} for PG1031 and J0317, using data from both the 20 and 13 cm observing bands, are presented in Table 6.4. Note that *these constraints are upper limits*, in the assumption of isotropic wind electron pitch angles. The calculations were made using the flux limits from Table 6.2 and the stellar parameters listed in Table 6.3.

6.5 A Goldreich-Julian magnetosphere for HMWDs

The analysis of Goldreich & Julian (1969) showed that a generalised dipole rotator must have a magnetospheric plasma to maintain dynamical equilibrium in the surface layers of the star. Here, I suggest that this argument applies to white dwarfs and neutron stars alike. Under such a model, assuming that only electrodynamic forces contribute to HMWD winds, I estimate the wind densities, spin-down rates and characteristic ages of J0317 and PG1031. In the case of the pitch angles of the electrons in the wind being preferentially small, I consider the interaction of this wind with the ambient interstellar medium (ISM), and derive estimates for the total radio flux and size of a possible resulting wind nebula.

Goldreich & Julian (1969) showed, by considering a star with a dipole magnetic field aligned with the rotation axis, that if no plasma existed beyond the stellar surface a magnetic field aligned electric field in the surface layer would cause this layer to be unstable. In the assumption of infinite conductivity within the star, Ohm's law for the current $\mathbf{J}$ in terms of the conductivity σ_c, electric field $\mathbf{E}$, particle velocity $\mathbf{v}$ and magnetic field $\mathbf{B}$ states

$$\mathbf{J} = \sigma_c(\mathbf{E} + \mathbf{v} \times \mathbf{B})$$

This implies that, as $\sigma_c \to \infty$,

$$\mathbf{E} = -\mathbf{v} \times \mathbf{B} = -(\mathbf{\Omega} \times \mathbf{r}) \times \mathbf{B} \tag{6.7}$$

where $\mathbf{\Omega}$ is the angular velocity, and $\mathbf{r}$ is the radial vector. If we assume that there is no plasma outside the star, then the external potential Φ is found by solving Laplace's equation $\nabla^2\Phi = 0$. The boundary condition is the electric field at the stellar surface ($r = R$). Taking $\mathbf{B}$ as a dipole field with polar field strength B_p aligned with the rotation axis,

$$\Phi = -\frac{B_p \Omega R^5}{6r^3}(3\cos^2(\theta) - 1) \tag{6.8}$$

where θ is the coordinate angle measured from the magnetic and rotation axes. Then, at $r = R$, we have

$$\mathbf{E} \cdot \mathbf{B} = \Omega R B_p^2 \cos^3(\theta)$$

and, at $\theta = 0$ (the North magnetic pole), the component of the electric field parallel to the magnetic field is

$$E_{\parallel} = \Omega R B_p \tag{6.9}$$

If we use the first Maxwell equation $\nabla \cdot \mathbf{E} = \rho_e/\epsilon_0$ to find the charge density ρ_e, the number density of unit charged particles just above the poles is

$$n_e = 2\Omega\epsilon_0 B_p \sim 6.9 \times 10^8 B_p/P \tag{6.10}$$

This is the Goldreich-Julian magnetosphere charge density. Note that the sign of the charged particles does not matter, because both positive and negative charges will be accelerated by the parallel electric field. I define the ratio f_{GE} between the gravitational forces binding charged particles to the star and the electric forces accelerating the charges as

$$f_{GE} = \frac{GMm_X}{\Omega R^3 B_p} \tag{6.11}$$

where G is the gravitational constant and m_X is the mass of the charged particle, be it an electron, proton, or something else. Therefore, a rotating magnetic star must have a magnetospheric plasma, with a minimum polar plasma particle number density of n_e.

Next, I consider the rate of energy loss of HMWDs. Adapting the expression of Ostriker & Gunn (1969): the rate of energy loss $\dot{U}$ of a rotating magnetic star with its magnetic axis offset from the rotation axis by an angle α is

$$\dot{U} = -\frac{2}{3}(m \sin\alpha)^2 \Omega^4 \tag{6.12}$$

where $m = B_p R/2$ is the dipole moment of the star. The energy loss is derived by considering the electromagnetic radiation emitted by a rotating dipole. However, a component of this 'braking radiation' can also be transformed into the acceleration of charged particles [Manchester & Taylor 1977]. This is the origin of the pulsar wind, and our postulated origin for winds from HMWDs.

Given the energy loss $\dot{U}$, the rate of change $\dot{P}$ of the rotation period P can be written as

$$\dot{P} = \frac{P^3 \dot{U}}{4\pi^2 I} \tag{6.13}$$

where $I = 2MR^2/5$ is the moment of inertia of the star. I also define a characteristic age τ_0 of the star in the same manner as for pulsars [Manchester & Taylor 1977]:

$$\tau_0 = \frac{1}{2}\frac{P}{\dot{P}} \tag{6.14}$$

This age is intended to represent the time that the system has been dominated by $\dot{P}$ braking.

When the ram pressure $P_{ram} = \rho_w v^2$ of the stellar wind is equivalent to the pressure $P_{med} \sim \rho_{ISM} k_B T_{ISM}$ of the ambient interstellar medium (ISM), a shock forms (ρ_w is the density of the wind, v is the wind velocity, ρ_{ISM} is the density of the ISM and T_{ISM} is the temperature of the ISM). In the shock, the energy of the wind is dissipated as heat. Arons (1983) estimated the radius R_s (in parsecs) of this shock (for pulsars, though I assume this to apply to white dwarfs as well) in terms of $\dot{U}$, τ_0 and the ISM number density $n_{ISM} \sim \rho_{ISM}/m_H$ (assuming a pure hydrogen ISM; m_H is the mass of a hydrogen atom) as

$$R_s \sim 4.4 \times 10^{-12} (\frac{\dot{U}\tau_0^3}{n_{ISM}})^{1/5} \tag{6.15}$$

I assume here that *all* of the energy loss of the star is converted into kinetic energy in the wind. The ISM is modelled in terms of a dominant (90% of the composition) warm hydrogen component with a number density $n_{ISM} = 3 \times 10^5\,\mathrm{m}^{-3}$ [Ferriere 1998]. This value is adopted in the calculations below.

In the ideal case of a white dwarf that is stationary with respect to the ISM, and where the ISM is not influenced by discrete components such as supernova remnants, the wind shock forms a spherical bubble about the star. The situation mirrors that of a pulsar wind nebula [Gaensler & Slane 2006], except that, as we shall see, the energetics of the winds are significantly lower for white dwarfs than for pulsars. I shall term these *white dwarf wind nebulae* (DWNe).

At the shock, electrons streaming as part of a HMWD wind are forced into a thermal distribution through Joule heating, and their pitch angles are randomised. Pulsar winds are thought to have highly anisotropic pitch angle distributions clustered close to zero [Gaensler et al. 2000]. This is intended to explain the lack of quiescent off-pulse emission from pulsars. The small pitch angles of the electrons in the wind, and their relativistic velocities, mean that any radiation is highly beamed and not isotropic. This beaming provides a crude perspective on the origin of pulses in pulsars. It can be argued that this scenario explains the lack of radio emission from HMWDs as well. *I now proceed having made the assumption that electrons in white dwarf winds have small pitch angles.*

I suggest that, as is the case for pulsar wind nebulae (eg. Gaensler et al. 2000), thermal synchrotron radio emission will be visible from electrons at the shock. The bolometric radio luminosity L_R of DWNe can be written as

$$L_R = \epsilon \dot{U} \tag{6.16}$$

where ϵ is the efficiency of conversion between the energy loss of the star and the radio flux. If this luminosity is modelled as being radiated between 10 MHz and 100 GHz (across the radio band), the 20 cm (1.4 GHz) radio flux $S_{20\,cm}$ in

HMWD	Ω (rad s^{-1})	α	n_e (m^{-3})	f_{GE}	$\dot{U}$ (J s^{-1})	$\dot{P}$ (s s^{-1})	τ_0 (s)
PG1031	5.1×10^{-4}	35°	2.8×10^{9}	2.4×10^{-29}	4.6×10^{8}	5.9×10^{-25}	1.0×10^{28}
J0317	8.7×10^{-3}	45°	4.3×10^{10}	2.2×10^{-30}	4.6×10^{13}	8.6×10^{-24}	4.2×10^{25}

Tab. 6.5: Estimated spin-down parameters for PG1031 and J0317.

HMWD	R_s (pc)	θ_{DWN} (deg)	S_{20cm} (mJy)	T_b (K)
PG1031	0.8	0.4	4.0×10^{-16}	6.7×10^{-24}
J0317	7.7	2.7	1.8×10^{-11}	3.0×10^{-19}

Tab. 6.6: Estimated DWN parameters for PG1031 and J0317.

millijansky at the Earth is given by

$$S_{20cm} = 2.1 \times 10^{-14} \frac{\epsilon \dot{U}}{D^2} mJy \tag{6.17}$$

where D is the distance to the star in parsecs. This flux is spread over the angular scale θ_{DWN} of the DWN, where $\theta_{DWN} = 2R_s/D$. The brightness temperature T_b of this radiation is given by

$$T_b = \frac{c^2 S_{20cm} \times 10^{-29} \theta_{DWN} \theta_{DWN}}{\nu^2 k_B} \tag{6.18}$$

As examples of our analysis above, I calculate properties of the spin-down and possible DWNe of J0317 and PG1031. Values for n_e, f_{GE}, $\dot{U}$, $\dot{P}$ and τ_0 are presented in Table 6.5, and values for R_s, θ_{DWN}, S_{20cm} and T_b are presented in Table 6.6. Values of α for PG1031 and J0317 are taken from Schmidt et al. (1986) and Barstow et al. (1997) respectively. The characteristic ages calculated using Equation 6.14, presented in Table 6.5, are greater than the age of the universe (which is $\sim 4.3 \times 10^{17}$ s) [Hinshaw et al. 2009]; I therefore use the age of the universe as the characteristic age τ_0 in the calculations for Table 6.6.

The choice of ϵ is made by considering typical values for pulsar wind nebulae radio fluxes. Gaensler et al. (2000) find from a survey of 27 pulsars for PWNe that, for the six youngest and most energetic pulsars, the non-detections of PWNe limit ϵ to the range $2 \times 10^{-7} - 2 \times 10^{-5}$. These measurements form the best known limits on ϵ for pulsars outside their original supernovae remnants; all these pulsars are beyond their supernovae remnants and exist in the ISM. I choose $\epsilon = 2 \times 10^{-6}$ for HMWDs.

6.6 Discussion

I have applied various models for the plasma conditions in the magnetospheres of HMWDs to derive observational constraints on the plasma densities, in the assumption of isotropic electron pitch angle distributions in the magnetospheres. I have also applied the theoretical framework for the spin-down of pulsars and pulsar

wind nebulae to HMWDs to estimate properties of the magnetosphere plasma, spin-down and possible wind nebulae. The DWNe analysis was conducted under the assumption of the wind electrons clustered at small pitch angles.

6.6.1 Comparison between the observational and theoretical results

I directly compare the observational plasma density constraints for PG1031 and J0317 derived using various emission models, given in Table 6.4, with the Goldreich-Julian densities given in Table 6.5. First, in the case of thermal gyrosynchrotron emission, the constraints are more than 50 orders of magnitude greater than the estimated values of n_e. This implies that the expected thermal emission is very weak, and requires fantastic plasma densities to produce detectable fluxes. If Razin-Tsytovich suppression applies for wavelengths longer than 13 cm, the lower limit of the plasma density is 6 orders of magnitude greater than the polar Goldreich-Julian density. I turn the argument around to state that if emission at 20 cm and 13 cm is *not* to be suppressed, the plasma number density must be less than a limiting value of

$$N_{RT} \leq 2.4 \times 10^{15}\, m^{-3}.$$

This is a much tighter constraint than the thermal limit. However, it is currently impossible to determine if Razin-Tsytovich suppression is in effect or not, given the higher thermal constraint and the lack of radio emission.

Amazingly, the non-thermal gyrosynchrotron constraints are in fact two orders of magnitude lower than the estimated Goldreich-Julian density values. Recall that all the emission calculations are conducted assuming completely isotropic pitch angle distributions. The non-thermal constraints are intriguing, because they imply that, for either J0317 or PG1031, if the entire Goldreich-Julian density of particles were non-thermal, with an isotropic pitch angle distribution, we would expect to see non-thermal gyrosynchrotron radio emission from the magnetosphere. This constraint is possibly loosened when one recalls that the emission was modelled as occuring at the 10^{th} cyclotron harmonic, in regions with magnetic fields that were six to seven orders of magnitude lower than the polar field strength. If the density decreases with the radius, as it does for every other free-streaming stellar wind known [Lamers & Cassinelli 1999], the plasma densities at the emission regions would be much lower than the polar density. While in both cases the non-thermal constraints are lower than the polar Goldreich-Julian densities, the densities at the emission regions given the calculated Goldreich-Julian densities could actually be much lower than the polar values. This argument also applies to the thermal and the Razin-Tsytovich suppression constraints.

While the comparison between the observational constraints and the Goldreich-Julian values is skewed by the plasma density distribution in a Goldreich- Julian magnetosphere, the observational constraints can still be compared among one another. Clearly, Razin-Tsytovich suppression precludes the possibility of thermal

gyrosynchrotron emission being visible in the observations. In fact, given that

$$S_\nu \propto T_b \propto \eta_\nu \propto N_{TH}$$

the maximum detectable thermal gyrosynchrotron fluxes at 13 cm are roughly 10^{-35} times less than the observational flux limits presented in Table 6.2. However, the somewhat tighter constraints on the non-thermal component of the wind assuming non-thermal gyrosynchrotron emission could imply that either the non-thermal components of the winds of PG1031 and J0317 are less than the constraining values, or that the pitch angle distributions of the winds are anisotropic. I posit the latter conclusion for two reasons:

- Particle acceleration by electric fields aligned with magnetic fields is an efficient mechanism for the production of non-thermal electrons [Melrose 1996]. This mechanism is variously applied to flows in solar, planetary, Ap star, brown dwarf and pulsar magnetospheres. I infer that the postulated HMWD wind is mainly non-thermal, if indeed driven by field-aligned electric fields. Whatever thermal component exists in this model is the result of collisions in the wind and between the wind and the ISM.

- Field aligned electric fields are also efficient mechanisms for producing particle distributions with small pitch angles [Melrose 1996]. If we assume that the collision component of the wind is low, then the pitch angles will not be randomised until the DWN shock and the wind will not radiate isotropically.

Therefore, I suggest that the pitch angles of the electrons in HMWD winds are small, and that the winds are more traceable by a study of DWNe properties, as opposed to emission emanating directly from the magnetosphere.

6.6.2 White dwarf wind nebulae

The integrated DWNe fluxes estimated above for PG1031 and J0317 (see Table 6.6) are well below current and envisaged detection thresholds at 20 cm. Upcoming surveys with next-generation radio telescopes such as ASKAP aim for maximum continuum sensitivities of $\sigma = 1\,\mu$Jy [Johnston et al. 2008]. The derived DWNe fluxes are 8 to 13 orders of magnitude lower than this value. Moreover, ASKAP will achieve such sensitivities over synthesised beams that are much smaller than the DWNe angular sizes. This means that the sensitivity to DWNe fluxes will be worse at least by factors of the ratios of the DWNe sizes to the synthesized beam diameters.

In fact, the DWNe signals will be dominated even by anisotropies in the Cosmic Microwave Background (CMB). The CMB is the blackbody radio background radiation in the universe, which was decoupled from matter upon the cooling and recombination of the primordial hot plasma $\sim 3.8 \times 10^5$ years after the Big Bang

[Hinshaw et al. 2009]. The redshifted radiation today has a brightness temperature of ∼2.73 K, with anisotropies on the order of 20 μK [Cayon & Smoot 1995]. These anisotropies are interpreted as density fluctuations in the early universe that evolved under gravity to form the current large-scale structure. The CMB power spectrum of angular fluctuations also peaks around 1°. The derived brightness temperatures for the DWNe of PG1031 and J0317 range between 10^{-13} and 10^{-18} of the typical CMB fluctuation temperatures, and are at angular scales where the CMB fluctuations are highest. Therefore, the DWNe of PG1031 and J0317 will not be detectable unless the CMB can be mapped to a sensitivity that is smaller than the DWNe fluxes. Note that the CMB can be identified and subtracted by its spectral properties: the spectrum is exactly that of a blackbody. However, current errors in the CMB measurements are of the order of one microkelvin [Cayon & Smoot 1995].

A comparison between the spin-down properties of HMWDs and pulsars reveals why DWNe are apparently impossible to detect. First, typical young pulsar magnetic fields are on the order of 10^8 T [Manchester & Taylor 1977], a factor of $\sim 10^4$ stronger than those of HMWDs. This, and the typical rotation periods of < 1 s lead to values of $\dot{U}$ for pulsars that are around 10^{27} J s^{-1} [Gaensler et al. 2000], 14 to 19 orders of magnitude greater than the values derived for PG1031 and J0317 (see Table 6.5). These are in fact roughly the factors by which the derived DWNe fluxes are less than the typical pulsar wind nebulae fluxes of a few mJy [Gaensler et al. 2000]. Furthermore, no 'static' PWN (a PWN caused purely by the shock between the ISM and the wind, with no component related to the pulsar proper motion that could result in a bow shock) has ever been observed for pulsars outside their original supernova remnants [Gaensler & Slane 2006].

There are three possibilities that could increase the detectability of a DWN. First, if a HMWD were to be found within a region of dense ISM, such as a supernova remnant, the resulting DWN would be confined to a much smaller region, reducing its angular size, increasing its surface brightness, and increasing the possibility of high angular resolution flux measurements. The second possibility is of high energy UV and X-ray emission from DWNe. Thermal X-ray emission is seen from a number of PWNe [Gaensler & Slane 2006], and there is a possibility that such emission will be visible from DWNe. I estimate the energy per particle E_p in the wind with velocity v at the stellar surface as

$$vE_p \sim \frac{\dot{U}}{4\pi R^2 n_e} \tag{6.19}$$

Also, we have

$$vE_p = v \times (m_e \gamma v c) = m_e c^2 \sqrt{\frac{v^4}{c^2 - v^2}}$$

for the electron component of the wind. Then, solving

$$(\frac{\dot{U}}{4\pi R_s^2 m_e n_e c^2})^2(c^2 - v^2) = v^4 \tag{6.20}$$

for the electron velocity v,

$$\begin{aligned} PG1031: \ v &\sim 9.9 \times 10^4 \, m \, s^{-1} \\ J0317: \ v &\sim 8.1 \times 10^6 \, m \, s^{-1} \end{aligned}$$

In a DWN shock, I estimate the temperature of the electrons T_e as

$$T_e \sim m_e v^2 / k_B \tag{6.21}$$

to get:

$$\begin{aligned} PG1031: \ T_e &\sim 6.5 \times 10^2 \, K \\ J0317: \ T_e &\sim 4.3 \times 10^6 \, K \end{aligned}$$

While the PG1031 wind does not appear to have enough energy to produce X-ray emission at the shock, the J0317 wind does. The temperature of 4.3×10^6 K corresponds to an energy of 370 eV, which is just within the conventional X-ray energy threshold of 160 eV. Further studies of DWN shock dynamics are required to accurately model this emission.

6.7 Conclusions

I have shown the following:

- Upper limits are placed for the quiescent 20 cm and 13 cm fluxes from the HMWDs PG1031 and J0317, and no variable or transient emission is found over the observing timespan.
- Razin-Tsytovich suppression implies that thermal gyrosynchrotron emission from PG1031 and J0317 is essentially non-detectable.
- The non-thermal constraining plasma densities for PG1031 and J0317 are lower than the polar Goldreich-Julian densities. The non-detection of radio emission therefore implies that the electron pitch angles in the wind are concentrated at small values.
- DWNe in the ISM are non-detectable with current and envisaged radio telescopes.

Unified physical properties of the low-field transient population

7.1 Introduction

There is a strong case to attempt a unified physical model for the periodic transient emission from magnetic rotating stars. As we have seen, systems ranging from brown dwarfs to CU Vir, as well as pulsars, all produce radio pulses through mechanisms linked to the rotation rates and the magnetic fields. However, if we consider the individual cases more closely, it is only in the case of pulsars that the pulse mechanisms can possibly be directly parametrised, in terms of the magnetic field and rotation rates in the Goldreich-Julian model of the pulsar magnetosphere [Goldreich & Julian 1969]. In all other cases of known pulse emitters, the magnetosphere plasma densities far exceed the Goldreich-Julian densities for the systems, necessitating other means by which the non-thermal electrons feeding the pulse emission mechanisms can populate the magnetosphere and be accelerated. These means, in the form of a radiatively driven wind and equatorial current sheet acceleration, are understood for CU Vir, but not in the case of brown dwarfs.

In this chapter, I briefly discuss commonalities and differences in and some methods of at least partly unifying the pulse emission models for brown dwarfs and CU Vir-type transients. This is carried out in the hope of developing pulsar-like parametrised models for the emission. I term these sources the Low Field Transient Population (LFTP). Also, some radio transients not identified with known objects, such as the periodic Galactic Centre radio transient GCRT 1745−3009 [Hyman et al. 2005], could originate in a magnetic rotator system. A model for transient emission from a magnetic rotator must have three components:

- A model for the magnetosphere, including the magnetic field geometry, the structures of various regions (such as zones of confined plasma), the plasma conditions (such as density, temperature and flow velocity profiles), and the way by which plasma is evacuated from the star.
- A model for the mechanism by which electrons are accelerated and obtain the appropriate non-thermal energy and possibly anisotropic pitch-angle distributions for the coherent emission mechanism.
- A model for the coherent emission mechanism itself, including the beaming geometry, polarisation and propagation effects.

The modelling work in Chapters 3 and 4 for the magnetosphere, nonthermal emission and pulses from CU Vir has all these components: I define the dead and wind zones by numerically solving for the plasma conditions, I fit the electron acceleration rate and model the spectral decay, and I model the beaming geometry of the

pulses. I now discuss models for brown dwarf pulses in comparison to the CU Vir models, and outline the possibility of basic parametrisations in terms only of the magnetic field strengths and the rotation.

7.2 Unified properties of the LFTP pulse models

Unlike the well-defined magnetosphere of CU Vir, we have seen that brown dwarf magnetospheres are not constrained. While it is known that a number of brown dwarfs do have large (kilo-Gauss, $\sim 0.1\,\mathrm{T}$) magnetic fields [Reiners & Basri 2007], the field structures are not defined. Reiners & Basri (2007) did not observe any modulation in the magnetic field lightcurves of any brown dwarf. However, an interesting feature of the Reiners & Basri (2007) study was that the magnetic field strengths were not correlated with the surface temperatures, but only with the $v \sin i$ rotation rates. The faster the rotation, the stronger was the observed magnetic field. This adds evidence for dynamo-type magnetic fields in brown dwarfs. Dynamo fields in low mass fully-convective stars, with masses < 0.35 solar masses (spectral types later than M3), are essentially dipolar and aligned with the stellar rotation axes [Phan-Bao et al. 2009]. The field strengths B_D are related to the rotation angular velocities ω as $B_D \propto \omega$ [Güdel 2002]. However, planetary dynamos in gas giants such as Jupiter are modelled as $B_D \propto \sqrt{\omega}$; some authors suggest that the latter mechanism is the one applicable to brown dwarfs [Burgasser & Putman 2005]. I prefer the former model given that it accounts for the presence of a stellar core where nuclear fusion is still occuring, whereas the planery dynamo model does not. However, in either case, I infer that the global magnetic fields of brown dwarfs are dipolar and aligned with the rotation axes.

These ideas have mixed implications for unified LFTP pulse emission models. The clear magnetosphere links are that the global fields are dipolar, and that in both cases the rotation has an impact on the magnetosphere structures. However, the lack of evidence for stellar winds in brown dwarfs implies that the means by which the magnetospheres are filled with plasma are unclear. Güdel (2002) suggests that low-mass stellar magnetospheres are filled in numerous microflaring events, and that such events make up the quiescent radio emission from such stars as well. However, microflares do not constitute a stellar wind: while I expect confined dead zones close to the surfaces of rapidly rotating magnetic brown dwarfs, with confinement at the Alfvén radius, I do not expect wind zones similar to that seen in CU Vir. Moreover, the aligned rotator model could also explain the lack of radio modulation of the quiescence from brown dwarfs. In CU Vir, the quiescent modulation is caused by the varying amount of confined dead zone matter in the line of sight. This would not be the case for brown dwarfs because the confined zone would be symmetric about both the rotation and magnetic axes. Careful measurements of the timing of pulses from brown dwarfs could provide a measure of the spin-down rate, and hence an estimate of the mass loss due to the continuous

replenishment of the magnetospheric plasma.

The lack of wind zones in brown dwarfs immediately means that the acceleration and non-thermal electron propagation models are different in brown dwarfs as compared to CU Vir-type transients. However, while these models may be different in their geometries and the populations of electrons that are accelerated, it is believed that the actual acceleration mechanisms both involve magnetic reconnection events. Strong Hα flares (recall that a correlation exists between Hα activity and magnetic field strength in M stars) have been observed from a number of brown dwarfs [Schmidt et al. 2007], all tied to magnetic reconnection events in the stellar coronae. Therefore, while the acceleration might occur in different places and in different geometries in the two models, the basic statistics of the acceleration rate and the same electron distributions apply to both brown dwarfs and CU Vir-type transients. The spectrum I have measured for DENIS 1048−3956 directly confirms the presence of a power law distribution of non-thermal electrons in the magnetosphere; this is directly analogous to the non-thermal electron population of CU Vir. However, it appears that the non-thermal electron population in the DENIS 1048−3956 magnetosphere is more evenly spread than that of the CU Vir magnetosphere, given the lack of modulation. I note that the lack of modulation is also explained by the alignment of the rotation and magnetic axes. The non-thermal component of the DENIS 1048−3956 magnetosphere also appears to be highly stable, given that the quiescence was detected at similar levels both in 2004 and 2009. Either the system was stable over this time, or it has somehow varied and returned to the same state. A final comment is that, under this model of microflares filling the magnetosphere and possible magnetic reconnection acceleration in these flares, the DENIS 1048−3956 flares observed by Burgasser & Putman (2005) could simply have corresponded to a particularly large surface flare. However, the $\sim 100\%$ circular polarisation of the flares combined with the high brightness temperatures ($T_b > 10^{13}$ K), imply a coherent emission mechanism, possibly an ECM, that would have to be accounted for in a 'giant flare' model.

Finally, I consider the emission mechanisms of the pulses from brown dwarfs and from CU Vir. This is possibly the easiest component of the pulse models, given that it is accepted that ECM mechanisms apply in both cases. The particular flavour of the ECM mechanism − whether the loss-cone mechanism, suggested Chapter 3 for CU Vir, applies to brown dwarfs or not − in both cases still needs to be constrained. However, simple facts such as fundamental cyclotron frequency emission and perpendicular beaming could tentatively be treated as common between the models. Also, the geometries of the non-thermal electron flows feeding the coherent emission mechanisms could be similar. Some non-thermal electrons accelerated in brown dwarf flare plumes could be captured by the magnetic fields and flow, gyrating, towards the poles in a direct analogy with the CU Vir magnetosphere geometry.

In summary, I identify the following commonalities in models for LFTP pulses.

First, all models involve dipole magnetic fields, of roughly the same kilo-Gauss ($\sim 0.1\,\mathrm{T}$) strengths, and regions of confined plasma close to the stars. The models predict an azimuthally symmetric spread of negative power law non-thermal electrons that are isotropic in the pitch angle distributions. These electrons, flowing towards the poles, radiate through a gyrosynchrotron mechanism, and the spectra decay via this emission, inverse Compton and magnetic mirroring processes. At regions where the fundamental cyclotron frequency is the same as the frequency of interest, an ECM mechanism at the observing frequency operates. The variability of the quiescence and the shapes of the pulses is possibly caused by fluctuations in the stream of non-thermal electrons feeding the emission mechanisms.

A significant motivation for a unified model for LFTP pulses is to make an attempt to constrain the population of such objects. Such constraints are possible by parametrising the model in terms of common independent observables, such as the rotation period, or maximum surface rotation velocity, and the magnetic field. In the simple (!) case of pulsars, a lower limit on the rotation periods exists when the rates of energy dissipation through braking radiation (see Equation 6.12) are not enough to produce detectable bolometric luminosities. However, unless the model described above can be parametrised in terms of such observables, no theoretically based population syntheses are possible at present.

Conclusions: Ideas for Future Work

8.1 Concluding remarks

This thesis has been a somewhat sprawling description of studies characterising prototypical examples of three potential classes of stellar radio transient. I have approached this field from a different perspective than is the norm. Rather than attempting blind surveys for transient radio emission that would subsequently be identified with sources, I targeted known examples of rotating magnetic star transient emitters in attempts to isolate transient source populations. The goals of this thesis, outlined in Chapter 1, fell into two groups. First, I intended to model the transient radio emission from various types of magnetic rotating star, based on previous and new targeted observations, with the ultimate goal of finding unified physical characteristics. I thought that these characteristics could be a possible means of understanding the population of magnetic star radio transients, both in terms of how many such stars could produce transient emission, and how persistent the transient emission would be. Also, much was made of the similarities between pulsar emission and the pulsed emission from lower magnetic field stars, such as CU Vir, and the simmilarities between pulsars themselves and HMWDs. It was hoped that some insight could be gained into the pulsar emission mechanism by studying lower field, but larger, more easily probed systems. The second set of goals revolved around rationalising possible populations of stellar transients by applying both the modelling work and new observational data for the known transient emitters.

In this final chapter, I discuss the overall conclusions of this work in the context of the initial goals, and describe necessary future studies. I split the discussion into two parts: the discussion of the negative result for the radio emission from HMWDs and the observational and modelling results for the low-field transient population.

The non-detection of radio emission, transient or quiescent, from the observed HMWDs can be interpreted in two fairly elementary ways. Either the observed HMWDs cannot support a persistent pulsar-like emission mechanism, or such a mechanism exists but is beamed away from the line of sight. Given that a Goldreich-Julian magnetosphere must exist for these stars, I have shown that if HMWD winds are like pulsar winds in their anisotropic electron pitch angle distributions, there is little chance of observational proof for their existence in the form of quiescent radio emission. Also, the non-detection of quiescent emission, in the assumption of a non-thermal electron energy distribution in the wind, implies that the electron pitch angles are not isotropically distributed. Therefore, it seems clear that the only way to prove that HMWDs can be sources of transient emission, analogous in their appearances and mechanisms to pulsars, is by actually detecting periodic radio pulses.

The work on the LFTP stars, including the MCP star CU Vir and the brown dwarfs LHS 3003 and DENIS 1048−3956 proved to be more fruitful. While no radio pulses were detected from either of the brown dwarfs observed, I demonstrated for the first time the existence of a negative power law spectrum for the quiescent emission from DENIS 1048−3956. This implies a negative power law non-thermal magnetospheric electron population that is very similar to that of CU Vir. Indeed, both electron populations were possibly accelerated in magnetic reconnection events, with those of the brown dwarf occuring near the stellar surface, and those of CU Vir occuring in the current sheet. Extrapolating the DENIS 1048−3956 result to other radio-loud brown dwarfs, we have a possibly unified model for the pulses from the LFTP, with ECM emission emitted in a loss-cone mechanism fed by streams of non-thermal electrons flowing towards the magnetic poles. This mechanism was modelled in detail for CU Vir, and could be applied to known brown dwarf pulse emitters given estimates of the rotation and magnetic field orientations and geometries. It is important to note that this mechanism is clearly distinct from current ideas for the pulsar emission mechanism, in the following ways:

- The LFTP model contends that the emission mechanism is an ECM, beamed perpendicularly to the field lines, whereas pulsar emission is beamed along the field lines [Manchester & Taylor 1977], and is probably not caused by ECM mechanisms [Melrose 1992].

- Pulsar winds are completely different from the mechanisms suggested for the filling of the magnetospheres of the LFTP.

The methods used to estimate the detection rates of CU Vir-type transients in future radio surveys cannot be applied to brown dwarfs, because there is no single template for a brown dwarf radio transient source. First, of the six brown dwarfs observed to flare, the only commonalities among the flares are the almost certain origins in a coherent, possibly ECM, emission mechanism. The flares vary in flux, structure, sign of the polarisation, duty cycle and variability from period to period. More concerning is the variability of the states of the stars: some pulse emitters were previously not radio sources at all, and others appear to have stopped emitting pulses after having been detected to do so. This variability has been observed on timescales of years. I interpret this, along with the non-detection of quiescence from LHS 3003 after it had previously been detected, as evidence for two activity states in magnetic brown dwarfs. In this model, brown dwarfs oscillate between states of relative coronal inactivity where their radio luminosities are small and proportional to their X-ray luminosity[1], and radio loud states where there is a large population of non-thermal power law electrons in the magnetosphere being accelerated in reconnection events near the surface. Therefore, this behaviour,

[1] This is described by the Güdel-Benz relation for cool stars [Benz & Güdel 1994].

including the mechanism that causes the stars to 'turn on', will have to be characterised before population estimates for brown dwarf transients can be made. That said, it is certainly possible that similar effects, not yet observed, apply to the population of CU Vir-type transients, and that CU Vir is unique in its stability.

8.2 Ideas for future work

It is evident, both from the discussion above and the conclusions reached at the ends of each chapter that there is immense scope for future research into this field. I shall begin by outlining the various projects required to answer questions left outstanding by this work, and then move on to ideas to further the goals of the thesis.

The individual questions that require self-contained bodies of work are listed here:

- The anomaly between the radio and optical lightcurve periods of CU Vir needs to be resolved. The simplest method to achieve a satisfactory solution would be to perform simultaneous radio observations targeted at the pulses along with optical observations targeted at measuring both the magnetic field and the total lightcurve in the V photometric band. This would establish whether the radio pulse period is directly linked to the rotation of the star.

- The measurement of a wide-band dynamic spectrum of the CU Vir pulses would provide a highly accurate map of the magnetic field geometry, given our ECM emission model. Emission at different frequencies arrives at different times, and a continuous map of the pulse delay would provide an accurate measure of the magnetic field geometry. This would enable the existence of higher multipole moments in the magnetic field structure to be tested. I note here that an offset dipole can be modelled as a centered dipole with the addition of multipole moments, and a measurement of the pulse dynamic spectrum would enable the field offset to be modelled directly. Such measurements would need to be conducted over both the 20 and 13 cm bands, and would possibly require measurements in different parts of the band to be undertaken over different full rotations of the star and added in phase.

- The CU Vir magnetosphere quiescent emission model needs to be tested against the 20 and 13 cm quiescent lightcurves, once a careful search for modulation has been conducted. The various ideas outlined at the end of Chapter 4 also need to be implemented in the model. This refined model could be used to directly model the non-thermal electron population at the ECM emission zones, and to model the growth rate of emission modes there. This would form a direct prediction of the nature of the ECM mechanism.

- The wide-band spectra of known periodic pulsing brown dwarfs, such as TVLM 513−46546, LSR J1835+3259 and 2MASS J00361617+1821104 [Hallinan et al. 2008], and 2MASSW J0746425+200032 [Berger et al. 2009], including the pulses and quiescence, need to be measured. Assuming ECM emission, this would enable a characterisation of the magnetic field geometry, as suggested above for CU Vir, using the dynamic spectra of the pulses. The quiescent spectra, along with measures of the circular polarisation fractions, would enable the magnetosphere plasma non-thermal electron densities and the magnetic field strengths to be estimated, as was achieved in Chapter 5 with DENIS 1048−3956.

- The pulses from some, or all of the known brown dwarf pulsators listed above need to be carefully timed over long timescales so as to measure the spin-down of the stars. This would allow some insight into the degree of mass loss and the mechanism by which the magnetospheres are filled with plasma. Similar long-term timing studies are necessary for CU Vir in order to understand its spin-down, both persistent and abrupt.

- Brown dwarfs with known two-state radio activity behaviours that include pulses in the radio loud states, such as TVLM 513−46546 [Hallinan et al. 2007], need to be consistently monitored, in the hope that the nature of the state change can be identified. This would include time series and full Stokes continuum measurements across single rotation periods on a regular basis, every few weeks for example. This would help understand the triggering mechanism of the radio emission. In the radio quiet state, more sensitive observations would be required to test the adherence of the (possible) radio emission to the Güdel-Benz relation.

- In a somewhat similar study, brown dwarfs with known X-ray luminosities that are in radio-quiet states need to be observed at radio frequencies with the sensitivities required to measure the predicted Güdel-Benz radio fluxes. This would solidify this relation for brown dwarfs in radio quiet states.

- The possibility of X-ray emission from the wind shocks of HMWDs needs to be more thoroughly analysed by modelling the shock dynamics. If the possibility exists, it must then be tested.

- Finally, while there is not sufficient motivation to perform further searches for radio emission from HMWDs, a recently identified ultramassive, fast spinning white dwarf, RX J0648.0-4418, in an accreting binary with a period of only 13.2 s [Mereghetti et al. 2009] bears further radio study. This system is reminiscent of AE Aquarii [Venter & Meintjes 2006], a known radio flare emitter. A possible factor against there being radio emission are suggestions

by Mereghetti et al. (2009) that the magnetic field of this system is at the low end for white dwarfs.

The host of individual, targeted projects listed above, while important in their own rights, are not nearly sufficient to complete the goals of this thesis. To do so, large-scale surveys for transient emission from systems similar to CU Vir and the known brown dwarf pulse emitters are necessary. The population of magnetic star radio transients needs to be increased, in order to better characterise component populations and the LFTP as a whole. Therefore, a selection of objects with properties similar to the known pulse emitters, such as high magnetic field strengths (as compared to the rest of the respective stellar classes), fast rotation periods and relative nearness need to be surveyed for radio emission across individual periods of rotation. Measures of the magnetic lightcurves and optical periods close to or simultaneous with the radio observations are also necessary. While upcoming telescopes and surveys will probably do similar science, pre-empting the flood of information with model predictions and ideas for target sources based on emperical knowledge of the population of transient emitters would be highly useful. The study of stellar radio transients, throughout this work, has provided amazing opportunities to further stellar astrophysics and our understanding of the radio sky, and has opened up exciting new avenues for further research. Most importantly, however, it has been a whole lot of fun.

BIBLIOGRAPHY

[Arons 1983] Arons J., 1983, Nat, 302, 301

[Babel & Montmerle 1997] Babel J., Montmerle T., 1997, AA, 323, 121

[Backer et al. 1982] Backer D. C., Kulkarni S. R., Heiles C., Davis M. M., Goss W. M., 1982, Nat, 300, 615

[Barrett et al. 1999] Barrett P., McConnell M., Drake S., Lim J., Ferrario L., Vennes S., 1999, in Bulletin of the American Astronomical Society. p. 736

[Barstow et al. 1995] Barstow M. A., Jordan S., O'Donoghue D., Burleigh M. R., Napiwotzki R., Harrop-Allin M. K., 1995, MNRAS, 277, 971

[Begelman, Ergun & Rees 2005] Begelman M. C., Ergun R. E., Rees M. J., 2005, ApJ, 625, 51

[Benz & Güdel 1994] Benz A. O., Güdel M., 1994, AA, 285, 621

[Benz, Alef & Güdel 1995] Benz A. O., Alef W., Güdel M., 1995, AA, 298, 187

[Berger 2002] Berger E., 2002, ApJ, 572, 503

[Berger 2006] Berger E., 2006, ApJ, 648, 629

[Berger et al. 2001] Berger E. et al., 2001, Nat, 410, 338

[Berger et al. 2009] Berger E. et al., 2009, ApJ, 695, 310

[Bingham, Cairns & Kellett 2001] Bingham R., Cairns R. A., Kellett B. J., 2001, AA, 370, 1000

[Borra & Landstreet 1980] Borra E. F., Landstreet J. D., 1980, Astrophysical Journal Supplement Series, 42, 421

[Bower et al. 2007] Bower G. C., Saul D., Bloom J. S., Bolatto A., Filippenko A. V., Foley R. J., Perley D., 2007, ApJ, 666, 346

[Burgasser & Putman 2005] Burgasser A. J., Putman M. E., 2005, ApJ, 626, 486

[Burrows et al. 2001] Burrows A., Hubbard W. B., Lunine J. I., Liebert J., 2001, Reviews of Modern Physics, 73, 719

[Catalano, Magazzu & Strazzulla 1979] Catalano F. A., Magazzu A., Strazzulla G., 1979, Information Bulletin on Variable Stars, 1695, 1

[Cayon & Smoot 1995] Cayon L., Smoot G., 1995, ApJ, 452, 487

[Cordes, Lazio & McLaughlin 2004] Cordes J. M., Lazio T. J. W., McLaughlin M. A., 2004, New Astronomy Review, 48, 1459

[Deutsch 1952] Deutsch A. J., 1952, ApJ, 116, 536

[Drake et al. 1987] Drake S. A., Abbott D. C., Bastian T. S., Bieging J. H., Churchwell E., Dulk G., Linsky J. L., 1987, ApJ, 322, 902

[Dulk & Marsh 1982] Dulk G. A., Marsh K. A., 1982, ApJ, 259, 350

[Dulk 1967] Dulk G. A., 1967, Icarus, 7, 173

[Dulk 1985] Dulk G. A., 1985, ARA&A, 23, 169

[Dulk, Bastian & Chanmugam 1983] Dulk G. A., Bastian T. S., Chanmugam G., 1983, ApJ, 273, 249

[Fender 2003] Fender R., 2003, 288, 79

[Ferrario & Wickramasinghe 2005] Ferrario L., Wickramasinghe D. T., 2005, MNRAS, 356, 615

[Ferrario & Wickramasinghe 2007] Ferrario L., Wickramasinghe D., 2007, MNRAS, 375, 1009

[Ferrario et al. 1997] Ferrario L., Vennes S., Wickramasinghe D. T., Bailey J. A., Christian D. J., 1997, MNRAS, 292, 205

[Ferriere 1998] Ferriere K., 1998, ApJ, 497, 759

[Fleming, Giampapa & Schmitt 2000] Fleming T. A., Giampapa M. S., Schmitt J. H. M. M., 2000, ApJ, 533, 372

[Frater, Brooks & Whiteoak 1992] Frater R. H., Brooks J. W., Whiteoak J. B., 1992, Journal of Electrical and Electronics Engineering Australia, 12, 103

[Gaensler & Slane 2006] Gaensler B. M., Slane P. O., 2006, ARA&A, 44, 17

[Gaensler et al. 2000] Gaensler B. M., Stappers B. W., Frail D. A., Moffett D. A., Johnston S., Chatterjee S., 2000, MNRAS, 318, 58

[Gizis et al. 2000] Gizis J. E., Monet D. G., Reid I. N., Kirkpatrick J. D., Liebert J., Williams R. J., 2000, AJ, 120, 1085

[Glagolevskij & Gerth 2002] Glagolevskij Y. V., Gerth E., 2002, AA, 382, 935

[Goldreich & Julian 1969] Goldreich P., Julian W. H., 1969, ApJ, 157, 869

[Groote & Hunger 1997] Groote D., Hunger K., 1997, AA, 319, 250

[Güdel 2002] Güdel M., 2002, ARA&A, 40, 217

[Güdel et al. 1993] Güdel M., Schmitt J. H. M. M., Bookbinder J. A., Fleming T. A., 1993, ApJ, 415, 236

[Hallinan et al. 2007] Hallinan G. et al., 2007, ApJ, 663, L25

[Hallinan et al. 2008] Hallinan G., Antonova A., Doyle J. G., Bourke S., Lane C., Golden A., 2008, ApJ, 684, 644

[Hasegawa & Sato 1989] Hasegawa A., Sato T., 1989, Space plasma physics: I - Stationary processes

[Hatzes 1997] Hatzes A. P., 1997, MNRAS, 288, 153

[Hewish et al. 1968] Hewish A., Bell S. J., Pilkington J. D. H., Scott P. F., Collins R. A., 1968, Nat, 217, 709

[Hewitt, Melrose & Ronnmark 1982] Hewitt R. G., Melrose D. B., Ronnmark K. G., 1982, Australian Journal of Physics, 35, 447

[Hewitt, Melrose & Ruennmark 1981] Hewitt R. G., Melrose D. B., Ruennmark K. G., 1981, Proceedings of the Astronomical Society of Australia, 4, 221

[Hinshaw et al. 2009] Hinshaw G. et al., 2009, ApJS, 180, 225

[Hobbs, Edwards & Manchester 2006] Hobbs G. B., Edwards R. T., Manchester R. N., 2006, MNRAS, 369, 655

[Högbom 1974] Högbom J. A., 1974, 15, 417

[Hyman et al. 2005] Hyman S. D., Lazio T. J. W., Kassim N. E., Ray P. S., Markwardt C. B., Yusef-Zadeh F., 2005, Nat, 434, 50

[Ikhsanov, Neustroev & Beskrovnaya 2004] Ikhsanov N. R., Neustroev V. V., Beskrovnaya N. G., 2004, AA, 421, 1131

[Johnston et al. 2008] Johnston S. et al., 2008, Experimental Astronomy, 22, 151

[Kawka et al. 2003] Kawka A., Vennes S., Wickramasinghe D. T., Schmidt G. D., Koch R., 2003, in D. de Martino, R. Silvotti, J.-E. Solheim, & R. Kalytis,

ed, NATO ASIB Proc. 105: White Dwarfs. p. 179

[Kellett et al. 2007] Kellett B. J., Graffagnino V., Bingham R., Muxlow T. W. B., Gunn A. G., 2007, ArXiv Astrophysics e-prints

[Khokhlova & Ryabchikova 1970] Khokhlova V. L., Ryabchikova T. A., 1970, Astrophysics, 6, 112

[Kirkpatrick et al. 1999] Kirkpatrick J. D. et al., 1999, ApJ, 519, 802

[Klebesadel, Strong & Olson 1973] Klebesadel R. W., Strong I. B., Olson R. A., 1973, ApJ, 182, L85+

[Klein 1987] Klein K., 1987, AA, 183, 341

[Kramer 2005] Kramer M., 2005, in L. I. Gurvits, S. Frey, & S. Rawlings, ed, EAS Publications Series. p. 219

[Kraus 1986] Kraus J. D., 1986, Radio astronomy

[Kundu 1983] Kundu M. R., 1983, Solar Physics, 86, 205

[Kurth, Baumback & Gurnett 1975] Kurth W. S., Baumback M. M., Gurnett D. A., 1975, Journal of Geophysical Research, 80, 2764

[Lamers & Cassinelli 1999] Lamers H. J. G. L. M., Cassinelli J. P., 1999, Introduction to Stellar Winds

[Latter, Schmidt & Green 1987] Latter W. B., Schmidt G. D., Green R. F., 1987, ApJ, 320, 308

[Leone & Manfre 1996] Leone F., Manfre M., 1996, AA, 315, 526

[Leone & Umana 1993] Leone F., Umana G., 1993, AA, 268, 667

[Leone 1991] Leone F., 1991, AA, 252, 198

[Leone, Catalano & Manfre 1993] Leone F., Catalano F. A., Manfre M., 1993, AA, 279, 167

[Leone et al. 2004] Leone F., Trigilio C., Neri R., Umana G., 2004, AA, 423, 1095

[Leone, Trigilio & Umana 1994] Leone F., Trigilio C., Umana G., 1994, AA, 283, 908

[Leone, Umana & Trigilio 1996] Leone F., Umana G., Trigilio C., 1996, AA, 310, 271

[Leto et al. 2006] Leto P., Trigilio C., Buemi C. S., Umana G., Leone F., 2006, AA, 458, 831

[Liebert 1980] Liebert J., 1980, ARA&A, 18, 363

[Liebert et al. 2003] Liebert J., Kirkpatrick J. D., Cruz K. L., Reid I. N., Burgasser A., Tinney C. G., Gizis J. E., 2003, AJ, 125, 343

[Lim, Drake & Linsky 1996] Lim J., Drake S. A., Linsky J. L., 1996, in A. R. Taylor & J. M. Paredes, ed, Radio Emission from the Stars and the Sun. p. 324

[Linsky, Drake & Bastian 1992] Linsky J. L., Drake S. A., Bastian T. S., 1992, ApJ, 393, 341

[Longair 1994] Longair M. S., 1994, High energy astrophysics. Volume 2. Stars, the Galaxy and the interstellar medium.

[Lorimer et al. 2007] Lorimer D. R., Bailes M., McLaughlin M. A., Narkevic D. J., Crawford F., 2007, Science, 318, 777

[Manchester & Taylor 1977] Manchester R. N., Taylor J. H., 1977, Pulsars.

[Manchester et al. 2001] Manchester R. N. et al., 2001, MNRAS, 328, 17

[Mason & Gray 2007] Mason P. A., Gray C. L., 2007, ApJ, 660, 662

[Matsumura et al. 2007] Matsumura N. et al., 2007, AJ, 133, 1441

[McLaughlin et al. 2006] McLaughlin M. A. et al., 2006, Nat, 439, 817

[Melrose & Dulk 1982] Melrose D. B., Dulk G. A., 1982, ApJ, 259, 844

[Melrose & Dulk 1993] Melrose D. B., Dulk G. A., 1993, Planetary and Space Science, 41, 333

[Melrose 1976] Melrose D. B., 1976, ApJ, 207, 651

[Melrose 1992] Melrose D. B., 1992, Royal Society of London Philosophical Transactions Series A, 341, 105

[Melrose 1994] Melrose D. B., 1994, Space Science Reviews, 68, 159

[Melrose 1996] Melrose D. B., 1996, 242, 209

[Melrose, Dulk & Hewitt 1984] Melrose D. B., Dulk G. A., Hewitt R. G., 1984, Journal of Geophysical Research, 89, 897

[Mereghetti et al. 2009] Mereghetti S., Tiengo A., Esposito P., La Palombara N., Israel G. L., Stella L., 2009, Science, 325, 1222

[Michel & Sturrock 1974] Michel F. C., Sturrock P. A., 1974, Planetary and Space Science, 22, 1501

[Neuhäuser et al. 1999] Neuhäuser R. et al., 1999, AA, 343, 883

[Niinuma et al. 2009] Niinuma K. et al., 2009, ApJ, 704, 652

[Noordam 2004] Noordam J. E., 2004, in J. M. Oschmann Jr., ed, Society of Photo-Optical Instrumentation Engineers (SPIE) Conference Series. p. 817

[Norris & the EMU team 2009] Norris R. P., the EMU team, 2009, ArXiv e-prints

[Okoye & Hewish 1967] Okoye S. E., Hewish A., 1967, MNRAS, 137, 287

[Oppenheimer, Kulkarni & Stauffer 1998] Oppenheimer B. R., Kulkarni S. R., Stauffer J. R., 1998, ArXiv Astrophysics e-prints

[Osten et al. 2009] Osten R. A., Phan-Bao N., Hawley S. L., Reid I. N., Ojha R., 2009, ApJ, 700, 1750

[Ostriker & Gunn 1969] Ostriker J. P., Gunn J. E., 1969, ApJ, 157, 1395

[Parker 1967] Parker E. N., 1967, ApJ, 149, 517

[Petschek 1964] Petschek H. E., 1964, NASA Special Publication, 50, 425

[Phan-Bao et al. 2009] Phan-Bao N., Lim J., Donati J., Johns-Krull C. M., Martín E. L., 2009, ApJ, 704, 1721

[Power et al. 2008] Power J., Wade G. A., Aurière M., Silvester J., Hanes D., 2008, Contributions of the Astronomical Observatory Skalnate Pleso, 38, 443

[Pyper et al. 1998] Pyper D. M., Ryabchikova T., Malanushenko V., Kuschnig R., Plachinda S., Savanov I., 1998, AA, 339, 822

[Reiners & Basri 2007] Reiners A., Basri G., 2007, ApJ, 656, 1121

[Richards et al. 1998] Richards E. A., Kellermann K. I., Fomalont E. B., Windhorst R. A., Partridge R. B., 1998, AJ, 116, 1039

[Ryle & Hewish 1960] Ryle M., Hewish A., 1960, MNRAS, 120, 220

[Salter, Hogerheijde & Blake 2008] Salter D. M., Hogerheijde M. R., Blake G. A., 2008, AA, 492, L21

[Schmidt et al. 1986] Schmidt G. D., West S. C., Liebert J., Green R. F., Stockman H. S., 1986, ApJ, 309, 218

[Schmidt et al. 2007] Schmidt S. J., Cruz K. L., Bongiorno B. J., Liebert J., Reid I. N., 2007, AJ, 133, 2258

[Shore & Brown 1990] Shore S. N., Brown D. N., 1990, ApJ, 365, 665

[Shore 1987] Shore S. N., 1987, AJ, 94, 731

[Slottje 1978] Slottje C., 1978, Nat, 275, 520

[Stępień 1998] Stępień K., 1998, AA, 337, 754

[Tout et al. 2008] Tout C. A., Wickramasinghe D. T., Liebert J., Ferrario L., Pringle J. E., 2008, MNRAS, 387, 897

[Treumann 2006] Treumann R. A., 2006, Astronomy and Astrophysics Review, 13, 229

[Trigilio et al. 2000] Trigilio C., Leto P., Leone F., Umana G., Buemi C., 2000, AA, 362, 281

[Trigilio et al. 2004] Trigilio C., Leto P., Umana G., Leone F., Buemi C. S., 2004, AA, 418, 593

[Trigilio et al. 2008] Trigilio C., Leto P., Umana G., Buemi C. S., Leone F., 2008, MNRAS, 384, 1437

[Twiss 1958] Twiss R. Q., 1958, Australian Journal of Physics, 11, 564

[Usov & Melrose 1992] Usov V. V., Melrose D. B., 1992, ApJ, 395, 575

[Vanlandingham et al. 2005] Vanlandingham K. M. et al., 2005, AJ, 130, 734

[Vennes et al. 2003] Vennes S., Schmidt G. D., Ferrario L., Christian D. J., Wickramasinghe D. T., Kawka A., 2003, ApJ, 593, 1040

[Venter & Meintjes 2006] Venter L. A., Meintjes P. J., 2006, MNRAS, 366, 557

[Warwick 1967] Warwick J. W., 1967, Space Science Reviews, 6, 841

[Weber & Davis 1967] Weber E. J., Davis L. J., 1967, ApJ, 148, 217

[Wickramasinghe & Ferrario 2005] Wickramasinghe D. T., Ferrario L., 2005, MNRAS, 356, 1576

[Willson, Lang & Foster 1988] Willson R. F., Lang K. R., Foster P., 1988, AA, 199, 255

[Zhao et al. 1992] Zhao J. et al., 1992, Science, 255, 1538

[Zheleznyakov & Serber 1994] Zheleznyakov V. V., Serber A. V., 1994, ApJS, 90, 783